

UCLA

UCLA Electronic Theses and Dissertations

Title

Simulation on dislocation's contribution to metal strength and grain boundary's role as irradiation defect sink

Permalink

<https://escholarship.org/uc/item/1272643w>

Author

He, Sicong

Publication Date

2023

Peer reviewed|Thesis/dissertation

UNIVERSITY OF CALIFORNIA

Los Angeles

SIMULATION ON DISLOCATION'S CONTRIBUTION TO METAL
STRENGTH AND GRAIN BOUNDARY'S ROLE AS DEFECT SINK

A dissertation submitted in partial satisfaction
of the requirements for the degree
Doctor of Philosophy in Materials Science and Engineering

by

Sicong He

2023

© Copyright by

Sicong He

2023

ABSTRACT OF THE DISSERTATION

SIMULATION ON DISLOCATION'S CONTRIBUTION TO METAL
STRENGTH AND GRAIN BOUNDARY'S ROLE AS DEFECT SINK

by

Sicong He

Doctor of Philosophy in Materials Science and Engineering

University of California, Los Angeles, 2023

Professor Jaime Marian, Chair

This series of works have been focused on materials response to various harsh environments, i.e. high stresses, high temperature and irradiation. The work is mainly achieved by using different computer simulation techniques across multiple time and space regimes. Multiphysics and multiscale simulations were carried out to try to reveal the true physics behind some phenomena never seen before, discovering new sciences and mechanisms that are promising to guide future generation materials design.

The dissertation of Sicong He is approved.

Gaurav Sant

Yinmin Wang

Amartya Banerjee

Jaime Marian, Committee Chair

University of California, Los Angeles

2023

*To my parents . . .
who have been giving me care and strength through hard times,
fighting alongside me against all the challenges*

TABLE OF CONTENTS

1	Introduction	1
2	Modeling screw dislocations in Tungsten	2
2.1	Introduction	2
2.2	Raw atomistic inputs	5
2.3	General theory of the line-on-substrate model	8
2.3.1	Elastic interaction model	9
2.3.2	The line tension model as a simplified LOS approach	15
2.4	Implementation and parameterization of LOS models	17
2.4.1	The Peierls potential	17
2.4.2	Core energies	18
2.4.3	Implementation details	19
2.5	Results	22
2.5.1	System length scales: line shapes, kink separation, and kink widths	22
2.5.2	System energies: kink energies and activation enthalpies	25
2.6	Discussion	29
2.6.1	Comparisons between LOS models	29
2.6.2	Defining the core size by matching LOS models to atomistic data	30

2.6.3	Building 3D kink-pair models from 2D atomistic data	31
2.6.4	Discussion of other works	33
2.7	Conclusions	34
2.8	Fitting procedure of the stress dependence of the Peierls potential . . .	35
2.9	Fitting of core energy data	37
3	Edge dislocation model with superjogs in Nb-Mo-Ta-W HEA . . .	41
3.1	Introduction	42
3.2	Theory and models	46
3.2.1	Monte Carlo model of non-conservative edge dislocation motion	46
3.2.2	Dislocation dynamics model	50
3.2.3	Model parameterization	52
3.3	Results	57
3.3.1	Thermal super-jog concentration	57
3.3.2	Dislocation dynamics under stress	58
3.3.3	Time evolution of the plastic strain	59
3.3.4	Strain rate-temperature relations	61
3.4	Discussion	62
3.4.1	Physical model	62
3.4.2	An analytical model of edge dislocation strength based on the present numerical results	65
3.4.3	Discussion on model predictions	67

3.5	Conclusions	68
3.6	Computational flow diagram	70
3.7	Analytical model of edge dislocation strength due to super-jog evolution	71
4	Geometrically Necessary Dislocations signal analysis	75
4.1	Introduction	75
4.2	Introduction	76
4.3	Experimental Observations	78
4.3.1	Results	81
4.4	Theoretical Background	82
4.5	Computational Methods	84
4.5.1	Atomistic	84
4.5.2	Discrete GND analysis	85
4.6	Results	86
4.6.1	Molecular dynamics simulations	86
4.6.2	GND density calculations	88
4.7	General Discussion	91
4.8	Conclusions	93
4.9	Kinematic and physical definitions of the Nye tensor	93
4.9.1	Derivation of the dislocation density tensor	93
4.9.2	Dislocation density tensor: small deformation limit	96
4.9.3	Dislocation density and lattice curvature	97

4.10 CPU cost of Nye tensor extraction software	99
5 Simulation of the evolution of Grain boundary’s ability to absorb irradiation defects	107
5.1 Introduction	108
5.2 Mechanism of network formation near saturated grain boundaries under irradiation	111
5.3 Methods	116
5.3.1 Experimental	116
5.3.2 Computational models	117
5.3.3 Calculation and processing of GND fingerprints	119
5.4 Results	120
5.4.1 Experimental GND maps as a function of irradiation dose	120
5.4.2 Simulation results	121
5.5 Discussion	124
5.5.1 Phenomenology of denuded zone evolution near grain boundaries in irradiated crystals	124
5.5.2 Discussion on simulation methods and comparison with experimental results	126
5.5.3 Consistency of the present results with radiation damage theories	127
5.6 Conclusions	129
References	136

LIST OF FIGURES

2.1	Variation of the Peierls potential with stress for the EAM and MEAM potentials.	7
2.2	Core energies obtained from atomistic simulations. (Left) Total atomistic energy (per unit length) for a computational cell containing a screw dislocation segment modeled with the EAM potential. The total energy is partitioned between an elastic energy and a core energy assuming a value of $a = 2b$. c_1 represents the size of the box along a $\langle 110 \rangle$ crystallographic direction (separation of the dislocation dipole). (Right) Dislocation core energies as a function of the character angle θ all for $a = 2b$. Results for both interatomic potentials, as well as and DFT data, are shown.	9
2.3	Schematic representation of a kink-pair configuration on a straight screw dislocation. The points labeled \mathbf{L} and \mathbf{R} represent arbitrarily distant locations to the left and right of \mathbf{A} and \mathbf{D} , respectively. We use a cartesian coordinate system such that the x direction is along the glide direction, the y direction is normal to the glide plane, and z is oriented along the line. h_0 is the periodicity of the Peierls potential, w is the length of the \mathbf{BC} segment, and l_1 and l_2 are the widths of the kinks (projections of the \mathbf{AB} and \mathbf{CD} segments on x). The shaded region corresponds to the slipped area defined in eq. (2.4).	10
2.4	Representation of a discrete segment used to calculate the enthalpy of the kink-pair configuration using the line tension LOS model. x_0 is calculated as in eq. (2.12). The length of the black segment is L	16

2.5	Dislocation core energies for (a) EAM and (b) MEAM interatomic potentials as a function of the dislocation character angle θ and the core size a . The curves generated using eq.(2.20) for nine different values of a are also plotted.	19
2.6	Elastic interaction and self energies as a function of the length of LA and DR segments.	20
2.7	Optimized kink pair configurations as a function of stress for the EAM potential. (a) Elastic interaction model. (b) Line tension model.	22
2.8	Kink separation in the kink-pair under stress (normalized to the corresponding Peierls stress). The EI results indicate divergence at zero stress, in accordance with elasticity theory, while the LT values are finite at all stresses. Atomistic results for the EAM potential are shown for comparison, showing very good agreement with predictions by the LT model. . .	24
2.9	Amplitude of the saddle-point configuration for the LT model as a function of stress. The results for EAM (red squares) and MEAM (black circles) agree well with theoretical predictions [1] in each case (solid and dashed lines)	25
2.10	Kink widths, l_1 and l_2 (refer to Fig. 2.3), as a function of stress.	26
2.11	Kink-pair activation enthalpy for the EI and LT models, each for the EAM and MEAM potentials. The results are normalized to the unstressed activation enthalpy obtained in atomistic calculations and the Peierls stress in each case (refer to Table 2.1).	27

2.12	Energies of individual kinks for EI and LT modes and EAM and MEM potentials. The differences are due to the asymmetry of the core energy functions about the edge orientation.	29
2.13	Comparison of the Kocks-Ashby-Argon expressions corresponding to the EI, LT, and atomistic models using EAM parameters for W. The gray dashed line corresponds to LT results assuming no asymmetry in the core energies and no stress-dependence of the Peierls potential ($p = 0.88$, $q = 1.37$), while the gray solid line is the equivalent EI curve ($p = 0.50$, $q = 1.29$).	32
2.14	Fitting of U_0 and α for the EAM potential	35
2.15	Fitting of U_0 and α for the MEAM potential	36
2.16	Dependence of the dislocation core energy terms f and g on dislocation character for (a) EAM and (b) MEAM interatomic potentials.	38
3.1	Modes of super-jog evolution. (a) super-jog generation on a straight dislocation line. This mode of motion requires vacancy nucleation. (b) Direct translation along the slip direction \mathbf{s} . This mode of motion requires a vacancy jump.	47
3.2	Dislocation critical stresses and friction coefficients from ref. [3]. The two data points for screw and edge at 0 K were obtained using a SNAP potential [4].	51

3.3	Relaxed edge dislocation dipole utilized for vacancy formation energy calculations. (a) Atomistic representation according to common neighbor analysis and equivalent line representation, both extracted using <code>Ovito</code> [5]. (b) Side view showing the edge pole dislocation locations (\perp symbols) and atoms from three consecutive $[11\bar{2}]$ planes. Atoms are colored by chemical species (green for Nb, red for Mo, blue for Ta, and yellow for W). The atomic positions ‘0’ and ‘1’ (of significance in the text) are indicated in both images. The distance between positions 0 and 1 is equal to the first nearest neighbor distance (i.e., one Burgers vector) with both positions located on the same $[11\bar{2}]$ plane.	54
3.4	(a) Vacancy formation energy distribution in the Nb-Mo-Ta-W alloy at position ‘0’ near the edge dislocation core in Fig. 3.3b. (b) Migration energy distribution for the $1 \rightarrow 0$ jump at the edge dislocation core positions shown in Fig. 3.4a. Negative energies (shaded area in the graphs) signal the spontaneous formation of vacancies and transitions, respectively. . . .	55
3.5	Arrhenius plot of the thermal concentration of super-jogs, n_0 , as a function of temperature on edge dislocations. The figure includes both the lower-bound n_0 , characterized by the mean energy of the formation energy distribution in Fig. 3.4a, $\bar{E}_f^\perp = 0.93$ eV, and also the simulated n_0 , obtained by sampling from the distribution in Fig. 3.4a according to eq. (3.1) (obtained from 10 independent samplings at each temperature). . .	58

3.6	Plastic strain rate as a function of time at several temperatures under an applied stress of 1500 MPa for a dislocation source with a total length of $150b$ containing two super-jogs evenly spread at $+L/3$ and $+2L/3$. The inset shows an overlapping sequence of time frames of the dislocation configuration at 1700 K covering 30 ns of DD/kMC simulation.	60
3.7	Plastic strain as a function of: (a) stress for a fixed line length of $L = 150b$ and fixed number of super-jogs (two), (b) line length for a fixed applied stress of 1000 MPa and fixed number of super-jogs (two), and (c) number of super-jogs for fixed stress (1000 MPa) and line length ($210b$). The error bars represent the numerical variability obtained from five independent simulations for each case.	62
3.8	Variation of τ with temperature together with different terms contributing to it in eq. (3.11) for a strain rate of $\dot{\epsilon} = 10^{-4} \text{ s}^{-1}$. Experimental data from refs. [6, 7].	66
3.9	Flow diagram of the numerical procedure employed here. Processes pertaining to the kMC module are colored in shaded gray, while those pertaining to the DD module are colored in shaded blue. Each box is numbered according to the sequence of steps.	70
4.1	Schematic illustration of the computational workflow of the methods developed in this paper.	79
4.2	Bright field micrographs of a grain with $(a_0/2)\langle 111 \rangle$ Burgers vector dislocation loop being absorbed onto a $\langle 110 \rangle$ GB plane. Nye dislocation tensor map generated from PED ACOM orientation data highlighted increased signal at the $25^\circ [1 \ -3 \ -6]$ GB [2].	81

4.3	(a) Atomistic and (b) discrete line representation of an 80-Å $(a_0/2)[111]$ loop before absorption. (c) Atomistic and (d) discrete line representation of the partial absorption stage.	101
4.4	Two oblique views of the fully absorbed loop and the grain boundary using a DXA representation.	102
4.5	Absorbed dislocation loops in bcc Fe with original Burgers vector $(a_0/2)[111]$ and initial radii of (a) 20 Å and (b) 80 Å. The resulting disconnection loops and their corresponding Burgers vectors are shown and labeled. . .	102
4.6	(a) Cells containing net dislocation loop segment length for an 8.0-nm Voronoi discretization of the full 80-Å loop. (b) Heat map of the full loop according to the GND intensity of the loop.	103
4.7	Normalized GND density for the (a) 80-Å and (b) 20-Å loops before, during and after absorption by the GB as a function of average Voronoi cell size. The error bars reflect the variability in tessellation morphology for a constant average mesh size. The shaded region represents the GND signal detection limit, while the translucent lines show the GND signal calculated based on regular hexahedral meshes for reference.	104
4.8	Highlighted Voronoi cells with net dislocation content for the (a) partially- and (b) fully-absorbed loops. The corresponding regular hexahedral mesh representations are given in (c) and (d), respectively. Cells are colored according to their GND density (shown in the color bars in units of m^{-2}).	105
4.9	Dislocation lines crossing surface S bounded by closed circuit C.	106
4.10	CPU cost per (dislocation segment length) of the GND analysis software for the three cases considered in the main text of this paper.	106

5.1	Schematic sequence of two square $\frac{1}{2}\langle 111 \rangle$ prismatic dislocation loops (orange and blue) (a) gliding along their glide prisms (delineated by the thin orange and blue lines) on a collision trajectory; (b) coming into contact within the reaction volume (shaded cube); and (c) reacting to form a $[100]$ junction along their common intersection. The process is driven by elasticity and unidimensional random diffusion (1D Brownian motion). The junction (black segment) is unbalanced and satisfies the Burgers vector reaction $\frac{1}{2}[111] + \frac{1}{2}[1\bar{1}\bar{1}] \rightarrow [100]$	112
5.2	(a) Simulated GND footprints of two hexagonal $\frac{1}{2}\langle 111 \rangle$ prismatic loops when (top) they are separated beyond their reaction distance, and (bottom) after reaction along one of their edges (color map in arbitrary units). Color coding: ■ $\frac{1}{2}[\bar{1}11]$; ■ $\frac{1}{2}[\bar{1}\bar{1}\bar{1}]$; ■ $[\bar{1}00]$. (b) Schematic representation of an idealized prismatic loop network composed of $\langle 111 \rangle$ and $\langle 100 \rangle$ segments forming from a saturated grain boundary (located on the right edge of the image).	114
5.3	Nye dislocation tensor maps generated from PED ACOM orientation data, highlighting the increase of GND density at the GBs, as well as the evolution of Nye tensor signals, proposed to be dislocation networks, throughout differing nanocrystalline grain matrices (A-D) with the increase in He ion damage from 0.0 to 18.3 dpa. Fig. 5.3A is reproduced with permission from El-Atwani et al. [8].	131

- 5.4 (a) Initial formation of partial loop substructures on a saturated GB. The loops are colored according to their Burgers vectors. (b) The GB is fully ‘blanketed’ by partial loops. (c) Snapshot showing the arrival of the first loop that does not reach the GB (interacting instead with the half-loops). (d) Final loop network after 1.0 dpa of irradiation. Color coding: ■ $1/2[11\bar{1}]$; ■ $1/2[\bar{1}11]$; ■ $1/2[1\bar{1}1]$; ■ $1/2[\bar{1}\bar{1}\bar{1}]$; white $\langle 100 \rangle$ 132
- 5.5 Rendition of the configuration shown in Fig. 5.3b processed as explained in Section 5.3.3. The left image is a side view (edge-on to the GB), while the one on the right is the same configuration tilted at an angle. The inset corresponds to the box highlighted in Fig. 5.3 (pane A). The color bar for the GND density is quantitatively equivalent in both cases. 133
- 5.6 Calculated GND fingerprint of a twin plate bounded by two $\Sigma 3$ boundaries ($\approx 109^\circ$ -misorientation GB), showing the underlying atomistic structure seen along a $\langle 110 \rangle$ crystal direction. Superimposed on the image are the profiles for the lattice orientation ω and the lattice curvature κ profiles. The inset corresponds to the box highlighted in Fig. 5.3 (pane C). 134

LIST OF TABLES

2.1	Interatomic potential-specific parameters. The top half of the table includes atomistic parameters used in the LOS models: a_0 is the lattice constant, τ_P is the Peierls stress, U_{lk} and U_{rk} are the energies of left and right kinks, respectively, and $\Delta H_0 = U_{lk} + U_{rk}$ is the zero-stress kink-pair activation enthalpy. The bottom half of the table lists outputs of the LOS model calculations, separated between EI and LT calculations: a is the core width, p and q are the exponents of the phenomenological kink-pair enthalpy expressions, ΔH_0^* is the intercept of the kink-pair activation enthalpy with the vertical axis, and τ_a is the stress at which the activation enthalpy vanishes, equivalent to the athermal stress in experimental tests.	39
2.2	Values of the Fourier coefficients in eq. (2.21) for the EAM and MEAM potentials.	40
3.1	Summary of super-jog transitions.	49
3.2	Numerical expressions use for the temperature dependence of the coefficients plotted in Fig. 3.2. T is the absolute temperature in K.	52
3.3	Mean energies for the vacancy formation and migration energy distributions at dislocations cores (' \perp ', highlighted in red) and in the bulk ('V'), for both the random Nb-Mo-Ta-W system and the <i>gray</i> alloy. The relevant energies are highlighted in red.	56
3.4	Parameters and material constants used to evaluate eq. (3.22).	73
4.1	Fitting parameters for CPU cost vs mesh size	100

ACKNOWLEDGMENTS

I am thankful to my supervisor Professor Jaime Marian. Without his guidance and support, I would not have achieved all these works. I also want to express gratitude to the other Committee Members: Professor Gaurav Sant, Professor Yinmin Wang and Professor Amartya Banerjee. They helped me realize the improvements I still need to make. Finally, I would like to thank the colleagues I have worked with: Professor Mitra Taheri, Professor David Srolovitz, Xinran Zhou, Emily Hopkins and Larrisa Woryk, for all the support and considerations you have given me.

VITA

- 2012–2016 B.S. (Physics), Central China Normal University
- 2017–2019 M.S. (Materials Science and Engineering), University of California, Los Angeles
- 2019–2023 Graduate Student Researcher, Materials Science and Engineering Department, UCLA.
- 2023 Teaching Assistant, Materials Science and Engineering Department, UCLA. Taught "Computer Simulations of Materials" under direction of Professor Jaime Marian.

PUBLICATIONS

He, S., Overly, E., Bulatov, V., Marian, J., & Cereceda, D. (2019). Coupling 2D atomistic information to 3D kink-pair enthalpy models of screw dislocations in bcc metals. *Phys. Rev. Mater.*, 3, 103603. doi:10.1103/PhysRevMaterials.3.103603

Zhou, X., He, S., & Marian, J. (2021). Cross-kinks control screw dislocation strength in equiatomic bcc refractory alloys. *Acta Materialia*, 211, 116875. doi:10.1016/j.actamat.2021.116875

McElfresh, C., Roberts, C., He, S., Prikhodko, S., & Marian, J. (2022). Using machine-learning to understand complex microstructural effects on the mechanical behavior of Ti-6Al-4V alloys. *Computational Materials Science*, 208, 111267. doi:10.1016/j.commatsci.2022.111267

He, S., Zhou, X., Mordehai, D., & Marian, J. (2023). Thermal super-jogs control the high-temperature strength plateau in Nb-Mo-Ta-W alloys. *Acta Materialia*, 244, 118539. doi:10.1016/j.actamat.2022.118539

Woryk, L. M., He, S., Hopkins, E. M., Hung, C.-Y., Han, J., Srolovitz, D. J., ... Taheri, M. L. (2022). Geometrically necessary dislocation fingerprints of dislocation loop absorption at grain boundaries. *Phys. Rev. Mater.*, 6, 083804. doi:10.1103/PhysRevMaterials.6.083804

Zhou, X., Wang, X., Fey, L., He, S., Beyerlein, I., Cao, P., & Marian, J. (2023). Models of dislocation glide and strengthening mechanisms in bcc complex concentrated alloys. *MRS Bulletin*. doi:10.1557/s43577-023-00571-y

He, S., Hopkins, E. M., Leff, A. C., Zhou, X., Taheri, M. L., Marian, J. (submitted) Complex dislocation loop networks as natural extensions of the sink efficiency of saturated grain boundaries in irradiated metals.

CHAPTER 1

Introduction

The discoveries of novel materials have enabled the fast development of society nowadays. These newly synthesized materials have exhibited great properties in mechanical, electrical, thermal, magnetic and irradiation resistant aspects. The thesis will be organized as follows: Chapter 2 and 3 are simulations on a single dislocation's behavior. In Chapter 2, with inputs from atomistic calculations, our mesoscale simulations can predict screw dislocation's kink pair formation enthalpy in Tungsten with accuracy while saving computational cost. In Chapter 3, I simulate the dynamics of edge dislocations, which are strengthened by superjogs, explaining the high temperature strength retention of Refractory High Entropy Alloy NbMoTaW. In Chapter 4, I show a toolbox that I developed, which can analyse the geometrically necessary dislocations signals in Fe through pure computational approach. The results obtained through this way are then presented in Chapter 5. The irradiation defects's interaction with grain boundaries in Fe is both examined by experiments and simulations. And the quantitative agreement that we get enables us to recognize and propose a paradigm shift in grain boundaries's role as defect sinks.

CHAPTER 2

Modeling screw dislocations in Tungsten

2.1 Introduction

In the field of dislocation physics, body-centered cubic (bcc) metals are peculiar due to the existence of non-planar dislocations with screw character and thermally-activated mobility that control plastic flow at low-to-intermediate temperatures. These dislocations have a Burgers vector \mathbf{b} equal to $\frac{1}{2}\langle 111 \rangle$ and move on close-packed planes (primarily $\{110\}$ and $\{112\}$) [9, 10, 11, 12, 13]. Generally, this motion is understood to occur over a periodic energy landscape known as the *Peierls* potential via the thermally activated nucleation of steps on the dislocation line, known as *kink pairs*, and their subsequent sideward relaxation [14, 15, 16, 17, 18, 19, 20]. Screw dislocations in bcc materials often behave in non-crystallographic ways, giving rise to phenomena such as pencil glide, asymmetry of the critical stress in the twinning and anti-twinning glide directions, asymmetry of the critical stress under tension/compression loading, or anomalous slip [21, 22, 23, 24, 25, 26, 27, 28, 29, 30, 31]. Most of these peculiarities are typically attributed to the highly compact (non-planar) structure of the $\frac{1}{2}\langle 111 \rangle$ screw dislocation core, which has naturally attracted much attention over the last several decades mostly in the form of atomistic models [32, 33, 34]. Based on recent work using electronic structure calculations, a picture has emerged

whereby the preferred dislocation core structure in bcc crystals has been established to be a compact, non-dissociated core resting on an underlying sinusoidal Peierls potential, U_P [35, 36, 37, 38, 39].

The strong temperature dependence of the yield and flow stresses displayed by most bcc metals is generally rationalized in terms of the thermally-activated nature of kink-pair nucleation. As such, a principal objective of the materials community in bcc alloys has been to develop models to characterize the activation energy of kink pairs. These are typically based on energy minimization of curved string configurations lying on a static energy substrate in either one [40, 41] or two dimensions [42]. The energy of the string is obtained by solving an integro-differential equation in a two-dimensional space defined by the glide x and screw z directions that accounts for the elastic energy of the line, its position on the substrate potential, and the mechanical work done by the stress τ [43, 44]. These so-called line-on-substrate (LOS) approaches have been traditionally approximated by models that reduce the double line integral (along x and z) to discrete sums along one or both integration dimensions. In the so-called line-tension (LT) model the integral along the screw direction is replaced by a dislocation self-energy which depends on the curvature of the line. The other integral is solved along the glide coordinate, yielding the equilibrium shape of the kink-pair configuration on the substrate potential. These activated configurations are usually referred to as 'bulge' structures as they resemble a protuberance on the dislocation line projected along the glide direction. The LT approach works well when this protuberance is small, i.e. at high and intermediate stresses, but not at low stresses [40, 41]. For low values of τ , the elastic interaction (EI) between kinks governs the line energy, in which case one can approximate the bulge configuration by a polygon (typically a trapezoid) with mutually-interacting

elastic segments, reducing the double integral to a set of discrete convergent sums [45, 46].

While insights gained from these models have improved our understanding of the activated states of kink-pair configurations, knowledge obtained from a decade or so of atomistic calculations supports the need to augment LOS models with inelastic contributions brought about by non-linear effects of atomistic nature. The most important of these are (i) the alteration of the Peierls potential energy function in the presence of resolved shear stress, and (ii) the consideration of core energies into the energy description of kink-pair configurations. At low stresses, one can safely assume that U_P remains unchanged and the effect of stress on the dislocation can be linearly decoupled from the underlying substrate in the form of a mechanical work. However, at stresses approaching the critical stress, referred to as the Peierls stress τ_P at 0 K, it is insufficient to consider only the zero stress internal energy to represent the Peierls trajectory. This trajectory is defined as the rectilinear path, denoted by the reaction coordinate x , between two equivalent equilibrium states (known as ‘easy core’) on the Peierls potential, which has periodicity $h_0 = a_0 \frac{\sqrt{6}}{3}$, where a_0 is the lattice constant. As recent calculations have shown, U_P can couple to the applied stress in non-negligible ways [47]. For its part, the inelastic contribution to the total dislocation energy, referred to as the core energy, is known to be potentially an important driving force in the minimization of dislocation line configurations (e.g. the so-called self-force in dislocation dynamics models). In particular, as will be shown below, in bcc metals the dependence of the core energy with dislocation character is periodic in the entire $[-\frac{\pi}{2}, \frac{\pi}{2}]$ angular range of θ (taken to be equal to zero for the screw orientation), contrary to other crystal structures, which display a $[0, \frac{\pi}{2}]$ periodicity. While this is a consequence of a well-known asymmetry of the

bcc crystal lattice [12, 24, 23], it has not been included into continuum models of kink-pair configurations to date.

In this work, we explore the effect of these features on numerical LT and EI models of kink-pair configurations modified to account for variations in $U_P(x)$ brought about by the applied stress and character-dependent dislocation core energies. Ultimately, we are after checking whether the notion that atomic information based on (quasi) 2D simulations can be effectively integrated into dislocation energy models of 3D line configurations is correct to interpret bcc plastic behavior. As well, we check whether fine details obtained in atomistic models, such as, e.g., the energy asymmetry between left and right-handed kinks that has been observed in several bcc metals [48, 49, 50], can be accurately captured by this coupled approach. Our paper is organized as follows. First we introduce the unprocessed physical inputs as obtained from atomistic simulations. Next, we review the theoretical formulation of the EI and LT models employed here. This is followed by details about the coupling between atomistic information and the discretized continuum models. We then show results for two different atomistic force fields for tungsten. We conclude the paper with a discussion of the results and some general conclusions.

2.2 Raw atomistic inputs

Based on a prior analysis of several W interatomic potentials for screw dislocation property calculations [51], we have selected an embedded-atom method (EAM) [52] and a *modified*-EAM (MEAM) potential [53] as the most suitable in terms of physical accuracy and computational efficiency. Using these two potentials, we have studied the dependence of $U_P(x)$ on the resolved shear stress, and of the dislocation core

energies on dislocation character. This furnishes what we refer to as ‘raw’ atomistic inputs, i.e. before they are processed to be in usable form for the LOS models. Below we report on the numerical values in each case and provide a brief description of how they are arrived at.

2.2.0.1 Peierls potential

The Peierls potential $U_P(x)$ is obtained as the minimum energy path along the reaction coordinate x joining two adjacent equilibrium dislocation core configurations (known as *easy* core configurations). This is done using the nudged elastic band (NEB) method [54] in small atomistic supercells reflecting the structure of balanced dipole configurations oriented along the $[111]$, $[\bar{1}2\bar{1}]$ and $[\bar{1}01]$ directions. These configurations permit the use of periodic boundary conditions along all three supercell directions. The dimensions of the simulation cell along the three coordinate axes were $L_x = 13.6 \text{ \AA}(5b)$, $L_y = 108 \text{ \AA}$, and $L_z = 107 \text{ \AA}$, containing a total of $N = 10000$ atoms. The NEB trajectory is partitioned into 30 images constrained to relax in configurational hyperplanes defined by the normal axis along x ($3N - 1$ degrees of freedom).

Prior to the NEB calculations, unconstrained energy minimizations using LAMMPS [55] were carried out for the initial and final configurations. NEB trajectories are generated as a function of stress τ (resolved shear stress on the glide plane) and the results are shown in Fig. 2.1. The paths shown in the figure are generated by subtracting from the resulting NEB trajectory the mechanical work, $-\tau bx$, for each image and matching the equilibrium position, $x_0(\tau)$, and the associated energy in each case to the origin of each curve.

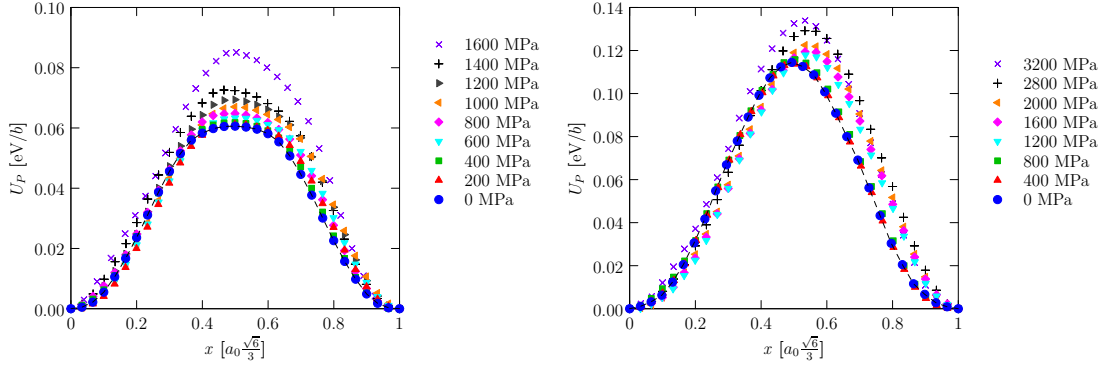


Figure 2.1: Variation of the Peierls potential with stress for the EAM and MEAM potentials.

2.2.0.2 Dislocation core energies

The dislocation core energy is a mathematical construct designed to remove the singularity in the stress and strain fields of elasticity theory. As such, the core region is eminently inelastic in nature and can arbitrarily be defined by a parameter a referred to as the *core radius*. This effectively partitions the total energy of a dislocation dipole into elastic and inelastic parts, with the latter confined to the core region within a [56, 57, 58] (cf. Section 2.3.1.2). This partition results in the following definition of the core energy:

$$e_c(\theta, a) = \frac{e_{\text{atm}}(\theta) - e_{\text{el}}(\theta, a)}{2} \quad (2.1)$$

where the angle $\theta = \cos^{-1} \left(\frac{\mathbf{b} \cdot \mathbf{t}}{b} \right)$ formed by the Burgers vector \mathbf{b} and the line direction \mathbf{t} defines the dislocation character, while the $1/2$ factor reflects the existence of a dislocation dipole.

The total energy e_{atm} is obtained from conjugate gradient minimizations of periodic atomistic supercells containing a dislocation dipole much in the manner described in the above section. The only difference resides in the orientation of the

supercell, whose axes z , y and x are now oriented along the \mathbf{n} , \mathbf{t} and $(\mathbf{n} \times \mathbf{t})$ directions, respectively. For its part, the elastic energy e_{el} is calculated by subtracting the interaction energy due to the periodic dipole network (appearing by virtue of using periodic boundary conditions) from the elastic energy of a dislocation dipole. An example of the partition of energy described by eq. (2.1) is shown in Figure 2.2. The core energies assuming a value of $a = 2b$ for the EAM and MEAM potentials, as well as for DFT calculations of pure screw (0°) and edge (90°) configurations [59] are also given in Fig. 2.2. As the graph shows, the angular periodicity of the core energy function is $(0, \pi)$, as there is an asymmetry in the energies about the pure edge orientation. This is not surprising, given the natural crystallographic asymmetry of the bcc lattice, which is most notoriously manifested in the existence of the so-called M111 dislocation orientation [60]. As will be discussed later, this asymmetry in the core energies leads to different energies for ‘left’ and ‘right’-handed kinks, a phenomenon commonly observed in atomistic calculations using a number of interatomic potentials [48, 49, 50].

2.3 General theory of the line-on-substrate model

Line-on-substrate model regards the dislocation as a line resting on a periodic energy landscape (substrate) that reflects the coupling between the dislocation line and the crystal lattice. As mentioned in Sec. 4.1, the two most widely used versions of the LOS model are the elastic interaction (EI) model and the line tension (LT) model. Here we provide a description of the theoretical formulations employed here for each of the two cases.

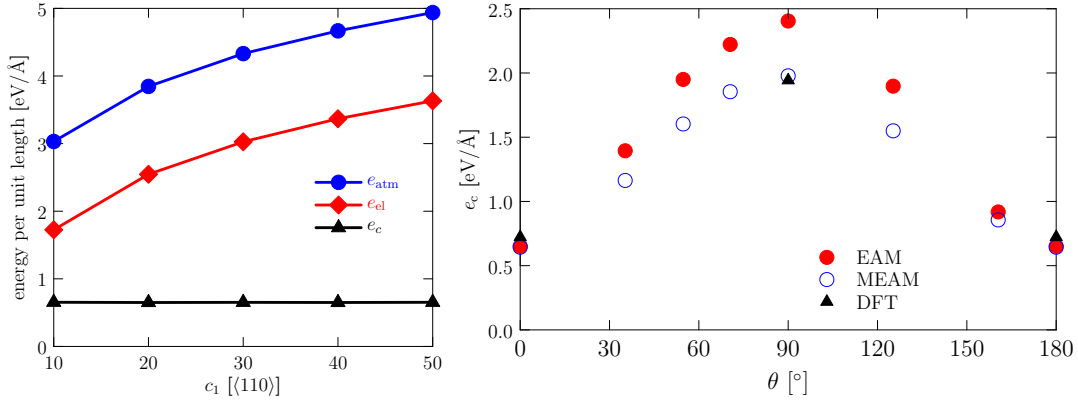


Figure 2.2: Core energies obtained from atomistic simulations. (Left) Total atomistic energy (per unit length) for a computational cell containing a screw dislocation segment modeled with the EAM potential. The total energy is partitioned between an elastic energy and a core energy assuming a value of $a = 2b$. c_1 represents the size of the box along a $\langle 110 \rangle$ crystallographic direction (separation of the dislocation dipole). (Right) Dislocation core energies as a function of the character angle θ all for $a = 2b$. Results for both interatomic potentials, as well as and DFT data, are shown.

2.3.1 Elastic interaction model

In the EI model, a kink-pair on a screw dislocation line can be approximated by an open trapezoid connected to two semi-infinite segments in the manner shown in Fig. 2.3: The segments LA and DR are located on the first Peierls valley, the segment BC is on the second Peierls valley, and AB and CD are the kink segments that straddle both minima. One can use the structure shown in Fig. 2.3 to obtain stable configurations for the activated state by optimizing the activation enthalpy of the system for a given stress. The activated state can be characterized by the sum of self-energies ΔE_{self} and interaction energies ΔE_{int} for all segments shown in the figure. In addition, the contribution to the energy of the underlying substrate ΔU_P

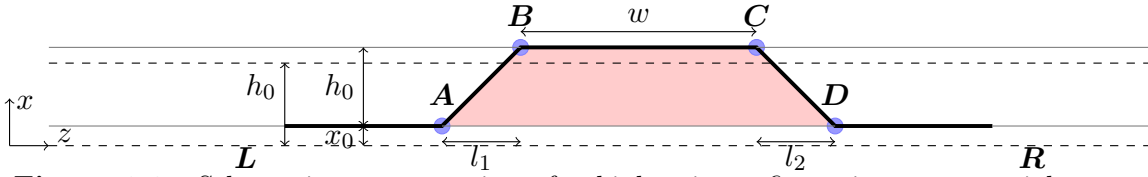


Figure 2.3: Schematic representation of a kink-pair configuration on a straight screw dislocation. The points labeled L and R represent arbitrarily distant locations to the left and right of A and D , respectively. We use a cartesian coordinate system such that the x direction is along the glide direction, the y direction is normal to the glide plane, and z is oriented along the line. h_0 is the periodicity of the Peierls potential, w is the length of the BC segment, and l_1 and l_2 are the widths of the kinks (projections of the AB and CD segments on x). The shaded region corresponds to the slipped area defined in eq. (2.4).

must be separately considered for the case of screw dislocations in bcc metals. The enthalpy is then obtained by subtracting the mechanical work W_m performed by the stress τ :

$$\Delta H(\{\mathbf{r}_i\}, \tau) = \Delta E_{\text{self}}(\{\mathbf{r}_i\}, \theta_i) + \Delta E_{\text{int}}(\{\mathbf{r}_i\}) + \Delta U_{\text{P}}(\{\mathbf{r}_i\}) - W_m(\tau, \{\mathbf{r}_i\}) \quad (2.2)$$

The stable configurations for the kink-pair structure shown in the figure are obtained by optimizing the above expression with respect to the coordinates \mathbf{r}_A , \mathbf{r}_B , \mathbf{r}_C , \mathbf{r}_D . Note that, due to the asymmetry in the e_c function described in the previous Section, in Fig. 2.3 the kink widths l_1 and l_2 do not necessarily have to be equal. This sets our work apart from other studies where it is commonly assumed that they are the same. The energies of the kink-pair configurations shown in the figure need to be computed piecewise, adding the contributions from all the dislocation segments. In the next sections we provide expressions for each of the energy terms introduced in eq. (2.2).

2.3.1.1 The mechanical work

The mechanical work W_m in eq. (2.2) is simply defined as:

$$W_m(\tau, \{\mathbf{r}_i\}) = \tau b A \quad (2.3)$$

where τ , b , and A are, respectively, the resolved stress on the glide plane, the magnitude of the Burgers vector, and the area swept by the kink pair. This area can be calculated as:

$$A = \frac{1}{2} (|\mathbf{AB} \times \mathbf{AC}| + |\mathbf{DC} \times \mathbf{DA}|) \quad (2.4)$$

where

$$\mathbf{AB} \equiv \mathbf{r}_B - \mathbf{r}_A$$

$$\mathbf{AC} \equiv \mathbf{r}_C - \mathbf{r}_A$$

$$\mathbf{DC} \equiv \mathbf{r}_C - \mathbf{r}_D$$

$$\mathbf{DA} \equiv \mathbf{r}_A - \mathbf{r}_D$$

2.3.1.2 Self-energies of dislocation segments

In accordance with [44] and [46], the total elastic self-energy of the configuration in Fig. 2.3 can be written as:

$$\Delta E_{\text{self}}^{\text{el}}(\{\mathbf{r}_i\}) = E_{\text{self}}^{\text{el}}(\mathbf{AB}) + E_{\text{self}}^{\text{el}}(\mathbf{BC}) + E_{\text{self}}^{\text{el}}(\mathbf{CD}) - E_{\text{self}}^{\text{el}}(\mathbf{AD}) \quad (2.5)$$

Here we use the non-singular expressions for the self-energy of a straight dislocation segment \mathbf{m} defined by endpoints \mathbf{r}_1 and \mathbf{r}_2 , and Burgers vector \mathbf{b} provided by [61], which give these energies as a function of θ and a . In this work, we add the core energy contribution to the above elastic energies as:

$$E_{\text{self}}(\mathbf{m}) = E_{\text{self}}^{\text{el}}(\mathbf{m}) + e_c(\theta, a) \|\mathbf{m}\| \quad (2.6)$$

2.3.1.3 Interaction energies

For the interaction energies, Hirth and Lothe [44] give the following expression for a symmetric kink-pair:

$$\begin{aligned} \Delta E_{\text{int}}(\{\mathbf{r}_i\}) = & \\ 2 [E_{\text{int}}(\mathbf{LA}/\mathbf{AB}) + E_{\text{int}}(\mathbf{LA}/\mathbf{BC}) + E_{\text{int}}(\mathbf{LA}/\mathbf{CD}) + E_{\text{int}}(\mathbf{AB}/\mathbf{BC}) - E_{\text{int}}(\mathbf{LA}/\mathbf{AD})] + & \\ + E_{\text{int}}(\mathbf{AB}/\mathbf{CD}) & \end{aligned} \quad (2.7)$$

This is because, for a symmetric configuration, the following equivalencies hold:

$$E_{\text{int}}(\mathbf{LA}/\mathbf{AB}) \equiv E_{\text{int}}(\mathbf{DR}/\mathbf{CD})$$

$$E_{\text{int}}(\mathbf{LA}/\mathbf{BC}) \equiv E_{\text{int}}(\mathbf{DR}/\mathbf{BC})$$

$$E_{\text{int}}(\mathbf{LA}/\mathbf{CD}) \equiv E_{\text{int}}(\mathbf{DR}/\mathbf{AB})$$

$$E_{\text{int}}(\mathbf{AB}/\mathbf{BC}) \equiv E_{\text{int}}(\mathbf{CD}/\mathbf{BC})$$

$$E_{\text{int}}(\mathbf{LA}/\mathbf{AD}) \equiv E_{\text{int}}(\mathbf{DR}/\mathbf{AD})$$

However, for an asymmetric configuration, only the last one is true and, thus, the sum of interaction energies reads:

$$\begin{aligned} \Delta E_{\text{int}}(\{\mathbf{r}_i\}) = & E_{\text{int}}(\mathbf{LA}/\mathbf{AB}) + E_{\text{int}}(\mathbf{DR}/\mathbf{CD}) \\ & + E_{\text{int}}(\mathbf{LA}/\mathbf{BC}) + E_{\text{int}}(\mathbf{DR}/\mathbf{BC}) + E_{\text{int}}(\mathbf{LA}/\mathbf{CD}) + \\ & + E_{\text{int}}(\mathbf{DR}/\mathbf{AB}) + E_{\text{int}}(\mathbf{AB}/\mathbf{BC}) + E_{\text{int}}(\mathbf{CD}/\mathbf{BC}) \\ & - 2E_{\text{int}}(\mathbf{LA}/\mathbf{AD}) + E_{\text{int}}(\mathbf{AB}/\mathbf{CD}) \end{aligned} \quad (2.8)$$

The general expression within non-singular isotropic elasticity theory for the interaction energy of two segments \mathbf{m} and \mathbf{n} with, respectively, endpoints \mathbf{r}_1 and \mathbf{r}_2 , and

\mathbf{r}_3 and \mathbf{r}_4 is:

$$E_{\text{int}}(\mathbf{m}, \mathbf{n}) = E^*(\mathbf{r}_4 - \mathbf{r}_2) + E^*(\mathbf{r}_3 - \mathbf{r}_1) - E^*(\mathbf{r}_4 - \mathbf{r}_1) - E^*(\mathbf{r}_3 - \mathbf{r}_2) \quad (2.9)$$

where the functional E^* takes different forms depending on the nature of the interaction. The non-singular elastic expressions used here to obtain E^* are all given by [61], which we omit for simplicity.

2.3.1.4 The Peierls potential

The kink pair structure shown in Fig. 2.3 rests on a periodic energy landscape known as the Peierls potential, U_{P} . Multiple atomistic studies using DFT and semi-empirical potentials [62, 63, 64] have shown that U_{P} is well represented by a (co)sinusoidal function of the type:

$$U_{\text{P}}(x) = \frac{U_0}{2(1-\alpha)} \left[1 - \cos \frac{2\pi x}{h_0} - \frac{\alpha}{2} \left(1 - \cos \frac{2\pi x}{h_0} \right)^2 \right] \quad (2.10)$$

where x represents the reaction coordinate (along the glide direction), U_0 is known as the Peierls energy, and h_0 is the period of U_{P} ($h_0 = a_0\sqrt{6}/3$ in bcc lattices). α is a parameter that captures the deviation of U_{P} from a pure cosine function. The contribution to the total energy of a kink segment lying across two Peierls valleys is:

$$\Delta U_{\text{P}}(\{\mathbf{r}_i\}) = \int_{\text{LABCDR}} U_{\text{P}}(x) d\ell - \int_{\text{LADR}} U_{\text{P}}(x) d\ell \quad (2.11)$$

Both of the above integrals are evaluated from an equilibrium position x_0 to $x_0 + h_0$. x_0 is obtained from the following relation:

$$\left. \frac{dU_{\text{P}}(x)}{dx} \right|_{x=x_0} = \tau b \quad (2.12)$$

The infinitesimal differential $d\ell$ follows along the kink segment and in general can be linearized as:

$$d\ell = \sqrt{dx^2 + dz^2}$$

We now make the approximation that the straight segments **LA**, **BC**, **DR** cancel with their respective counterparts in the **LADR** configuration. Then the above integrals reduce to:

$$\Delta U_{\text{P}}(\{\mathbf{r}_i\}) = \int_{x_0}^{x_0+h_0} U_{\text{P}}(x) (d\ell_1 + d\ell_2) - U_{\text{P}}(x_0) (l_1 + l_2) \quad (2.13)$$

To capture the effect of the resolved shear stress on the shape of $U_{\text{P}}(x)$ revealed in Sec. 2.2.0.1, we consider a stress dependence of both $U_0(\tau)$ and $\alpha(\tau)$, as will be shown in Appendix 2.8.

Equations (2.3), (2.5), (2.8), and (2.13) are combined to fully define the activation enthalpy in eq. (2.2), which is subsequently optimized for the set of parameters w , l_1 , and l_2 as a function of stress. Each saddle point corresponds to the activated state of the kink-pair at each stress, from which the dependence of $\Delta H(w, l_1, l_2)$ with τ can be calculated. The dimensions of the trapezoid corresponding to each optimized configuration are obtained as:

$$\begin{aligned} \mathbf{r}_A &\equiv (x_0, 0) \\ \mathbf{r}_B &\equiv (x_0 + h_0, l_1) \\ \mathbf{r}_C &\equiv (x_0 + h_0, l_1 + w) \\ \mathbf{r}_D &\equiv (x_0, l_1 + w + l_2) \end{aligned}$$

2.3.2 The line tension model as a simplified LOS approach

At low stresses the stability of the kink-pair configuration is controlled by the elastic interaction between the kink segments. However, as the stress increases and the shape of the line resembles more a ‘bulged’ structure with low curvature. In such cases, the elastic energy of the system is well approximated by a so-called *line tension* representation [65, 66], where the energy of the kink-pair structure is controlled by the curvature of non-straight segments. Within elasticity, the line tension is defined as:

$$T(\theta, a) = \frac{\partial E_{\text{self}}(\theta, a)}{\partial \ell} \quad (2.14)$$

which is the dislocation energy per unit length, depending only on dislocation character θ and the core radius a . For small dislocation segment lengths, ℓ , the above expression can be approximated by $T(\theta, a) \approx \frac{E_{\text{self}}(\theta, a)}{\ell}$. This form of $T(\theta, a)$ replaces the self and interaction elastic energies in the enthalpy expression for the kink-pair configuration. $\Delta H(\{\mathbf{r}_i\})$ now reads:

$$\Delta H(z, \tau) = \int dz [\Delta T(\theta(z), a) + \Delta e_c(\theta(z), a) + \Delta U_{\text{P}}(x(z), \tau) - W_m(\tau)] = \quad (2.15)$$

$$= \int dz [(T(\theta(z), a) - T(\theta = 0, a)) + (e_c(\theta(z), a) - e_c(\theta = 0, a)) + \Delta U_{\text{P}}(x(z), \tau) - W_m(\tau)] \quad (2.16)$$

where e_c , W_m and ΔU_{P} are defined as in Secs. 2.2.0.2, 2.3.1.1 and 2.3.1.4. Eq. (2.15) can be represented as a piecewise sum along the z direction of the contributions of individual segments of length b [67]:

$$\begin{aligned} \Delta H(\{x_i\}, \tau) = & b \sum_i [T(\theta_i, a) - T(\theta = 0, a) + (e_c(\theta_i, a) - e_c(\theta = 0, a)) + \\ & + \Delta U_{\text{P}}(x_i, \tau) - \frac{\tau b}{2}(x_{i+1} + x_i - 2x_0)] \end{aligned} \quad (2.17)$$

where $U_P(x, \tau)$ is given by equation (2.10), and $\theta_i = \tan^{-1} \left(\frac{x_{i+1} - x_i}{b} \right)$. The geometry of one discretization segment is shown in Fig. 2.4 for the calculation of the mechanical work.

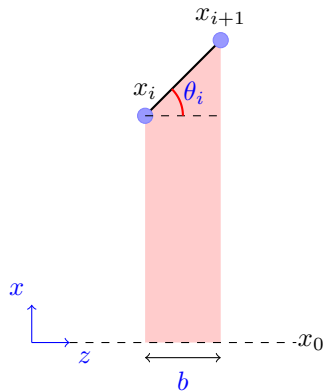


Figure 2.4: Representation of a discrete segment used to calculate the enthalpy of the kink-pair configuration using the line tension LOS model. x_0 is calculated as in eq. (2.12). The length of the black segment is L .

The expression utilized in eq. (2.14) is derived from those provided by [61], which expressed in piecewise form for use in eq. (2.17) is:

$$T(\theta, a) = \frac{\mu b^2}{4\pi(1-\nu)} \left\{ (1 - \nu \cos^2 \theta) \ln \frac{b + \sqrt{b^2 + a^2}}{a} - \frac{3 - \nu}{2} \left(\frac{\sqrt{b^2 + a^2} - a}{b} \right) \cos^2 \theta \right\} \quad (2.18)$$

The equilibrium configurations are obtained by minimizing the value of ΔH in eq. (2.17) as a function of the set of coordinates $\{x_i\}$ at each stress point τ .

2.4 Implementation and parameterization of LOS models

In this section we explain how to process the atomistic results described in Sec. 2.2 for use in the EI and LT models just presented. First, we discuss the expressions for the stress-dependence of the Peierls potential, followed by those pertaining to the core energies.

2.4.1 The Peierls potential

For the EI model, the integral in eq. (2.13) can be solved analytically and used directly in expression (2.2):

$$\begin{aligned}
\Delta U_{\text{P}}(\{\mathbf{r}_i\}) &= \left(\sqrt{1 + \frac{l_1^2}{h_0^2}} + \sqrt{1 + \frac{l_2^2}{h_0^2}} \right) \int_{x_0}^{x_0+h_0} U_{\text{P}}(x) dx - U_{\text{P}}(x_0) (l_1 + l_2) = \\
&= \frac{U_0}{2(1-\alpha)} \left\{ \left(\sqrt{1 + \frac{l_1^2}{h_0^2}} + \sqrt{1 + \frac{l_2^2}{h_0^2}} \right) \left[h_0 \left(1 - \frac{3\alpha}{4} \right) + \right. \right. \\
&\quad - \frac{h_0(1-\alpha)}{2\pi} \left(\sin \frac{2\pi(x_0+h_0)}{h_0} - \sin \frac{2\pi x_0}{h_0} \right) + \\
&\quad - \frac{h_0\alpha}{16\pi} \left(\sin \frac{4\pi(x_0+h_0)}{h_0} - \sin \frac{4\pi x_0}{h_0} \right) \left. \right] + \\
&\quad \left. - (l_1 + l_2) \left[1 - \cos \frac{2\pi x}{h_0} - \frac{\alpha}{2} \left(1 - \cos \frac{2\pi x}{h_0} \right)^2 \right] \right\} \quad (2.19)
\end{aligned}$$

where we have used $dz_\beta = \frac{l_\beta}{h_0} dx$, with $\beta = 1, 2$. The atomistic information provided in Sec. 2.2.0.1 has been introduced into this expression in the form of stress-dependent correlations for U_0 and α . We have seen that U_0 scales as τ^n whereas α is a linear function of τ . The specific expressions and the fitting procedure followed to obtain these correlations is described in Appendix 2.8.

For the LT model, $U_{\text{P}}(x_i)$ is evaluated directly using (2.10) for each discretized

segment x_i . Summation over all segments then gives us the total potential energy of the line, in accordance with eq. (2.17). The expressions for $U_0(\tau)$ and $\alpha(\tau)$ are identical to those used in the EI model.

2.4.2 Core energies

The core energy results from atomistic calculations shown in Sec. 2.2.0.2 are introduced in the same manner in the EI and LT models. In principle, the main features of e_c that a fitting procedure must capture are its dependence of both dislocation character (i.e. angle θ) and core width a . However, what is novel in this work is the slight asymmetry about the edge character orientation displayed in Fig. 2.2. For this, we additively separate the total core energy into an a -independent term, and an a -dependent one:

$$e_c(\theta, a) = f(\theta) + g(\theta) \log\left(\frac{a}{b}\right) \quad (2.20)$$

where $f(\theta)$ and $g(\theta)$ are obtained by fitting the data in Fig. 2.2 to Fourier series expansions of the type:

$$y(\theta) = c_0 + \sum_{k=1}^3 c_k \sin(2k\theta) + d_k \cos(2k\theta) \quad (2.21)$$

These functions can yield the asymmetry about $\theta = \pi/2$ and naturally satisfy the condition that their first derivative is equal to zero for $\theta = 0$ and $\theta = \pi$ (zero self-force for screw orientation). It is important to clarify that this partition of the core energy is mathematically arbitrary, and other works have opted for different approaches [68]. The dependence of the dislocation core energy with both the character angle and the core size is shown in Fig. 2.5. The details about the fitting procedure and the numerical values of the coefficients c_i and d_i are given in Appendix 2.9.

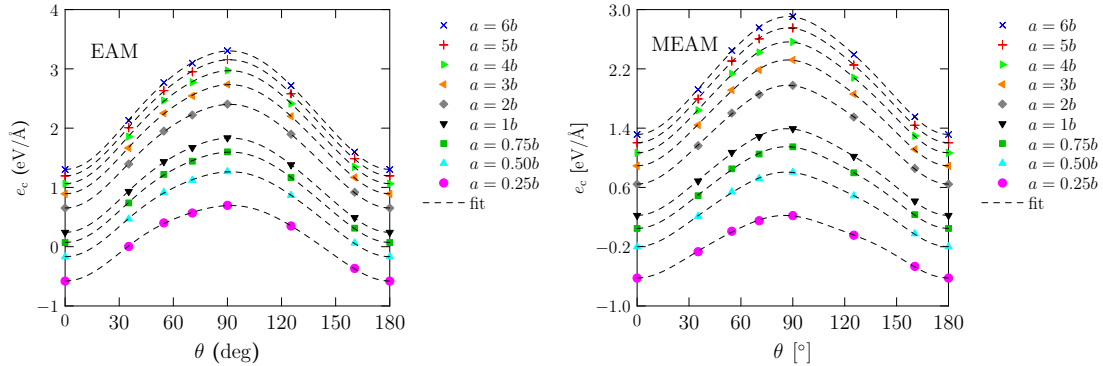


Figure 2.5: Dislocation core energies for (a) EAM and (b) MEAM interatomic potentials as a function of the dislocation character angle θ and the core size a . The curves generated using eq.(2.20) for nine different values of a are also plotted.

2.4.3 Implementation details

2.4.3.1 Elastic interaction model

In the EI model, the kink-pair configuration itself represents the activated state between the two minima in the Peierls potential representing the initial and final screw dislocation configurations. As such, the enthalpy in eq. (2.2) must be maximized along the reaction path. This is done by obtaining the saddle point of the entire structure as a function of the position of points A , B , C , and D in Fig. 2.3. However, standard (unconstrained) optimization algorithms are difficult to stabilize in an energy landscape that is only conditionally convergent [69]. The geometry of the configuration, however, can be used to identify conditions that favor convergence.

This can be done, for example, by noting that the trapezoid depicted in Fig. 2.3 represents a dislocation loop (with three ‘real’ segments and one ‘anti’ segment) whose elastic energy is known to be finite. This imposes limits on the minimum and maximum size of the trapezoidal structure that are discussed below.

(i) The condition of finite energy means that the total activation enthalpy in eq. (2.2) is independent of the size of segments \mathbf{LA} and \mathbf{DR} . Using isotropic singular linear elasticity, the terms depending on the lengths of these segments are seen to cancel in the analytical expressions for the total elastic energy of the trapezoidal configuration. With the non-singular theory, things are not quite as simple, as analytical expressions are not straightforward to obtain. However, the same premise must still hold. Here, we have performed a numerical study to confirm this, and have established the minimum length of segments \mathbf{LA} and \mathbf{DR} to have converged, length-independent energies. Fig. 2.6 shows the combined value of $(\Delta E_{\text{int}} + \Delta E_{\text{self}})$ in eq. (2.2) as a function of the value of $\|\mathbf{LA}\| \equiv \|\mathbf{RD}\|$. Our results show that values of approximately $200b$ or larger must be used to achieve length independence. In most simulations, we have typically used a value of $1000b$.

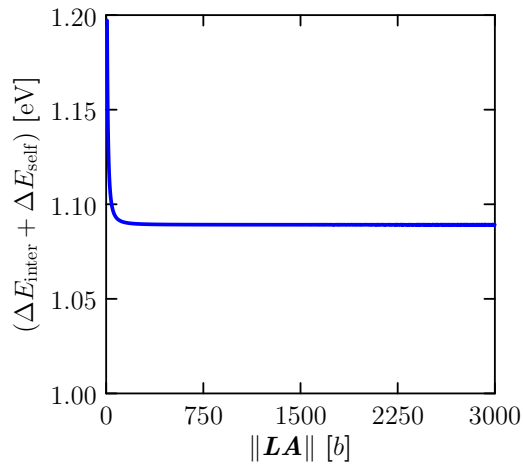


Figure 2.6: Elastic interaction and self energies as a function of the length of \mathbf{LA} and \mathbf{DR} segments.

(ii) At the same time, the separation of segments \mathbf{AB} and \mathbf{CD} (i.e. the value of

w in Fig. 2.3) must be sufficiently small for the elastic interaction energy to be finite within the numerical tolerance of our minimization procedure. w changes with stress, but we have found that, as a rule of thumb, at zero stress values of no less than $40b$ should be considered.

2.4.3.2 Line tension model

The case of the LT model differs from that of the EI model just explained. In this case, the saddle point configuration corresponds to a bulged structure that lies somewhere along the x coordinate. This configuration does not generally correspond to one where the line lies on either of the minima of U_P . Therefore, one must vary the size of the bulge, defined by a variable h along the x path between x_0 and h_0 until the system's enthalpy goes through a maximum. At each stress, this path is discretized and the saddle point structure found. This is expected to yield minimum energy paths that are substantially equivalent to dynamic trajectories [70]. To improve the rate of convergence, here we invert the potential energy landscape by altering the sign of the mechanical work along the path as to balance the the rest of the terms in the enthalpy and have net zero effect on the total energy. This approach has proven robust for the calculations undertaken in this work.

Once the saddle-point configuration is found for each stress, we approximate the left and right sides of the bulged structure with an arc tangent function. All the corresponding outputs (i.e. w , l_1 , l_2 , etc) are calculated upon mathematical analysis of the best approximants obtained for each case.

2.5 Results

The first-principles method used here for parameterizing and benchmarking the LOS model calculations are atomistic calculation results using two different interatomic potentials. Table 2.1 (top half) gives several parameters of importance obtained for each potential. Below, we discuss the most important results for the EI and LT models. Most results are shown in normalized form to facilitate inter-comparison: (i) the stress is expressed as the fraction of the Peierls stress, $s = \tau/\tau_P$, (ii) energies are plotted relative to the zero-stress activation enthalpy ΔH_0 , and (iii) lengths are expressed in Burgers vector units, b , or Peierls potential wavelength h_0 .

2.5.1 System length scales: line shapes, kink separation, and kink widths

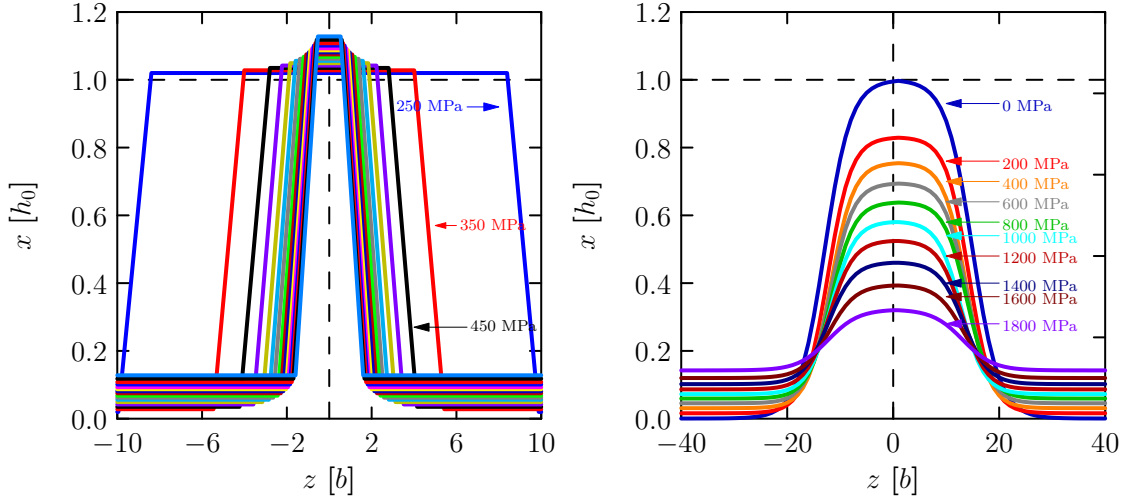


Figure 2.7: Optimized kink pair configurations as a function of stress for the EAM potential. (a) Elastic interaction model. (b) Line tension model.

Fig. 2.7 shows the optimized saddle point configurations for kink pairs as a function of stress under the EI and LT models for the EAM potential. The configurations

for the MEAM potential are qualitatively similar in both cases. The graphs for the EI model results do not show segments **LA** and **DR** in their entirety but a diminishing kink separation, w , can generally be observed as the stress increases. This variation of w with τ is plotted in Fig. 2.8. In accordance with elasticity theory, the kink-pair length diverges at zero stress, decreasing gradually with stress to a final value of $\approx 2b$. For its part, lacking an interaction energy, the results for w in the LT model are less significant, but they are weakly dependent on stress. Interestingly, LT predictions for the EAM and MEAM potentials result in differences of about a factor of two between both atomic models (higher for MEAM). As well, EAM values are in very good agreement with the corresponding atomistic results (around $10b$, from ref. [49]).

As shown in Fig. 2.7 for the LT model, the activated state for the dislocation is a bulged configuration straddling the Peierls potential. The amplitude of this bulge is plotted in Fig. 2.9 as a function of stress for the EAM and MEAM potentials. As the figure indicates, this amplitude coincides with the wavelength of $U_P(x)$, h_0 at zero stress, and is zero at the Peierls stress, consistent with the definition of the activated state at both ends of the stress range. Our results show excellent agreement with the expected analytical form for h in line tension models [70, 1] (shown as lines in Fig. 2.9).

While these results are interesting, one of the most important aspects in this work is the asymmetry in the dislocation core energies introduced in Sec. 2.2.0.2. This asymmetry manifests itself as differing kink ‘widths’, i.e. the spreading length along the dislocation line (z -coordinate) of the segments connecting two consecutive Peierls valleys. These are labeled l_1 and l_2 in Fig. 2.3. The results for these two lengths are shown in Fig. 2.10. With the EI model, there are slight differences between the left

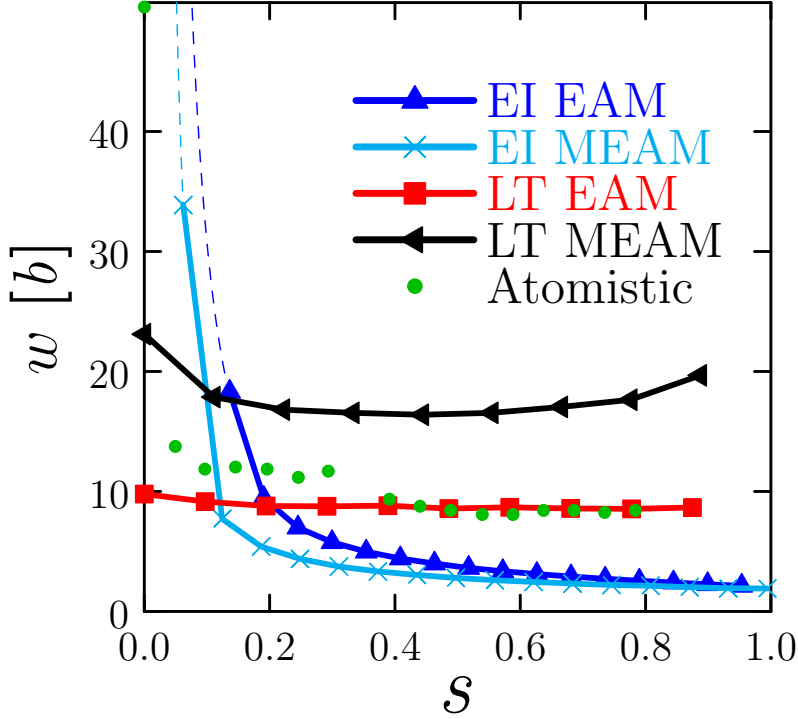


Figure 2.8: Kink separation in the kink-pair under stress (normalized to the corresponding Peierls stress). The EI results indicate divergence at zero stress, in accordance with elasticity theory, while the LT values are finite at all stresses. Atomistic results for the EAM potential are shown for comparison, showing very good agreement with predictions by the LT model.

and right kinks, with the left one, l_1 , being larger than the right one, l_2 . Contrary to the situation of the kink-pair separation w , here the EAM kinks spread over approximately twice the distance of the MEAM ones. These results also show a slow decrease of l_1 and l_2 with stress (kinks approaching the edge orientation), although interestingly these widths are around $1.5b$ for the MEAM potential and between 3 and $4b$ for EAM. This stands in contrast to atomistic results, which predict kink widths of approximately $25b$ for EAM calculations [49]. For their part, LT results

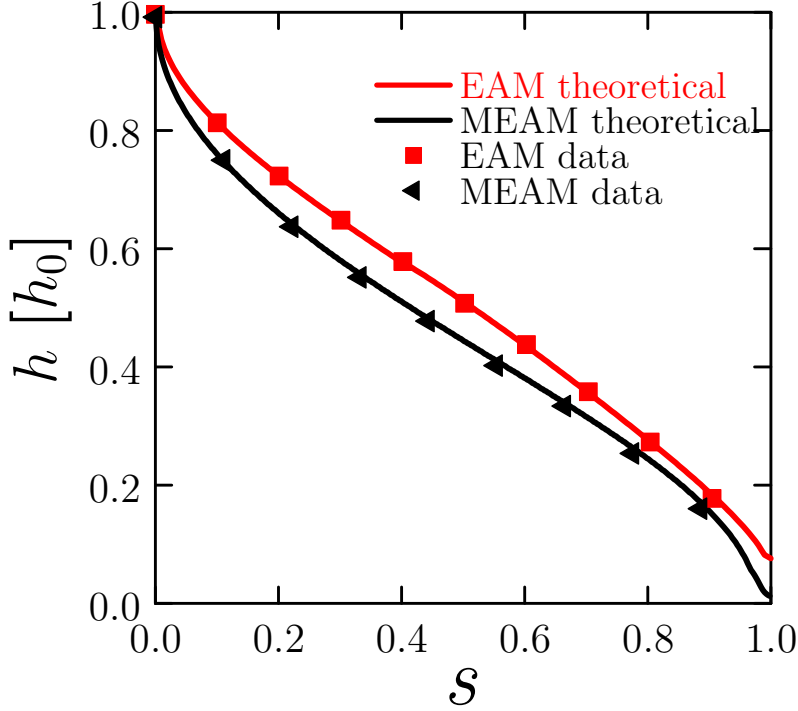


Figure 2.9: Amplitude of the saddle-point configuration for the LT model as a function of stress. The results for EAM (red squares) and MEAM (black circles) agree well with theoretical predictions [1] in each case (solid and dashed lines)

show no appreciable difference between l_1 and l_2 . Here too calculations for the EAM potential result in larger kink widths than for the MEAM potential, between 4.5 and $6b$ vs. 3 and $4b$, respectively. However, l_1 and l_2 display a different dependence with stress in this case, reaching a minimum at low stresses but growing with stress subsequently.

2.5.2 System energies: kink energies and activation enthalpies

The most important physical quantity to extract from our models is the kink-pair activation enthalpy as a function of stress. This is used in a number of approaches

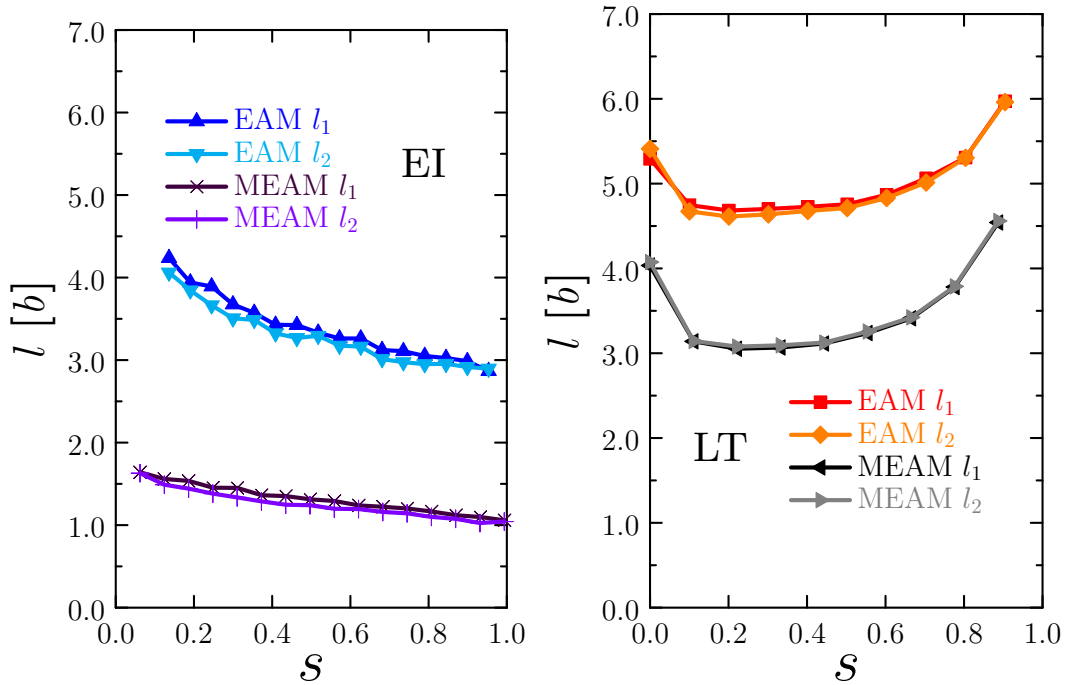


Figure 2.10: Kink widths, l_1 and l_2 (refer to Fig. 2.3), as a function of stress.

to describe thermally-activated screw dislocation motion in bcc metals (as it has been done in our works in the past, e.g. [49, 71]). In Fig. 2.11 we show the results for the EI and LT models, each in turn for the EAM and MEAM potentials. To facilitate comparison across different models and different interatomic potentials, we normalize the enthalpies by the unstressed activation enthalpy obtained in atomistic calculations in each case, ΔH_0 , and the stresses by the Peierls stress τ_P . These parameters are all given in Table 2.1. Note that (i) the enthalpy at zero stress for the EI model is undefined and therefore the data point shown in Fig. 2.11 is the atomistic value, and (ii) that the actual intercept of the activation enthalpy curves for the LT model with the vertical axis does not necessarily correspond to the atomistic

value¹. This is what is labeled as ΔH_0^* in Table 2.1. Similarly, intercepts with the stress axis in all cases do not necessarily match the value of τ_P , with the actual values labeled as τ_a in Table 2.1. We interpret these stresses as being the ‘athermal’ limits for the kink-pair mechanism in each case.

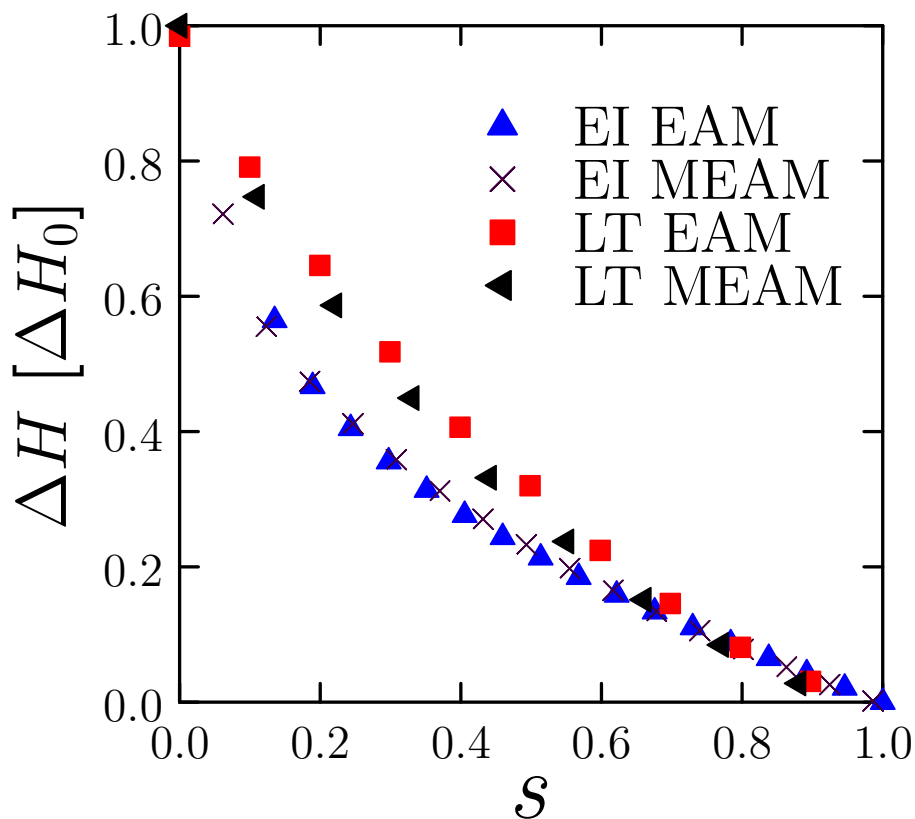


Figure 2.11: Kink-pair activation enthalpy for the EI and LT models, each for the EAM and MEAM potentials. The results are normalized to the unstressed activation enthalpy obtained in atomistic calculations and the Peierls stress in each case (refer to Table 2.1).

Most importantly, the values of a used in eqs. (2.6), (2.8), and (2.18) to obtain

¹It is also important to note that ΔH_0 is obtained atomistically via procedures that are insensitive to periodic image interactions [48].

these energies have been chosen as to provide the best fit of the activation enthalpy curves to the known atomistic values of ΔH_0 and τ_P . In other words, we arbitrarily set the core width value to match known ‘first-principles’ calculations of the potential in question. These values of a are provided also in Table 2.1 and, as can be seen, are always less than one Burgers vector distance. We will return to this issue in Sec. 2.6.

Finally, it is common practice to fit the curves in Fig. 2.11 to the Kocks-Ashby-Argon phenomenological expression [72]:

$$\Delta H(\tau) = \Delta H_0 \left(1 - \left(\frac{\tau}{\tau_P} \right)^p \right)^q$$

where p and q are exponents that describe the asymptotic behavior of $\Delta H(\tau)$ in the limits of zero stress ($q = 1.25$) and the Peierls stress ($p = 0.5$) for isotropic linear elasticity [66]. Since tungsten is elastic isotropic, our model provides an excellent testbed for these values, which have indeed been reproduced for stress-independent U_P and symmetric $e_c(\theta, a)$. These exponents are also provided in Table 2.1.

To evaluate again the effect of the core energy asymmetries on the energetics of the activated states, we calculate in Fig. 2.12 the individual kink energies as a function of τ . As no appreciable difference was found for the LT model predictions, we omit them from the figure for clarity. The energies shown include the interaction and self-energies in the EI model of the kink segments only. Only a noticeable difference can be found for the EAM results, approximately 10%, whereas kinks energies are practically identical for the MEAM potential. The individual atomistic kink energies are given in the table above as well (for zero stress), differing about 20% between themselves. We also discuss this more in depth in the next section.

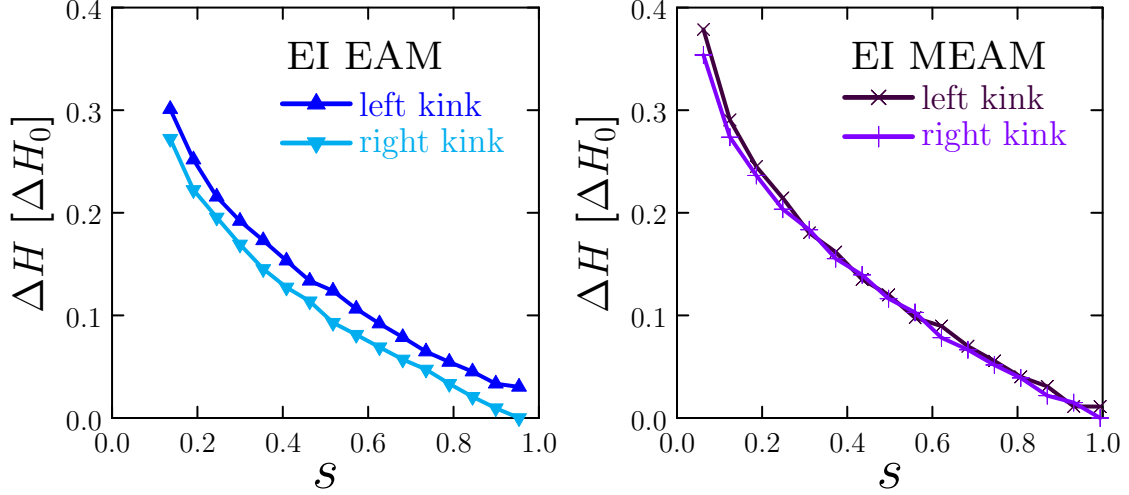


Figure 2.12: Energies of individual kinks for EI and LT modes and EAM and MEM potentials. The differences are due to the asymmetry of the core energy functions about the edge orientation.

2.6 Discussion

2.6.1 Comparisons between LOS models

As indicated in Sec. 4.1, different approximations to the line integral along the x (glide) direction to calculate the energy of the activated kink-pair state result in different LOS model formulations, each with its own advantages and disadvantages. The EI model approximates the bulge configuration better at low stresses, when the activated state extends across the entire Peierls potential period and the kink-pair energy is dominated by elastic interactions between kink segments. This allows the use of a simple trapezoidal structure to represent the system, which has the benefit of consisting of only four degrees of freedom. This considerably speeds up convergence of the energy minimizations, which allows us to study the parametric space of the model efficiently. The novel aspect of the EI model used here is the asymmetry of

the left and right kinks, by virtue of the character dependence of the core energy function. Regarding this, the EI model results predict differences of less than 1% in the kink widths for both EAM and MEAM parameters (Fig. 2.10), while the difference in enthalpy is slightly larger (Fig. 2.12).

For its part, the LT model is best suited for lines with small curvature, when the bulge configuration is small, a situation typically encountered at high stresses. The implementation of the LT approach involves, however, up to hundreds of discrete segments, which increases the computational severalfold compared to the EI model. LT results show no discernible difference in the values of both the energies and the kink widths. Thus, it appears that the LT model is less sensitive to the core energy asymmetry than the EI model.

In terms of EAM-vs-MEAM differences, as shown in Fig. 2.11, when normalized to the corresponding values of ΔH_0 and τ_P , EI and LT model results appear to be independent of the interatomic potential used. This is an encouraging result as it could potentially indicate that normalized LOS model predictions can be transferred across different potentials, which would eliminate a common source of variability in dislocation property calculations.

2.6.2 Defining the core size by matching LOS models to atomistic data

The size of the dislocation core (a in this work) is a mathematical construct introduced to remove the singularity inherent to the theory of elasticity. As such, it does not possess any intrinsic physical meaning, serving instead as an arbitrary limit between the elastic and inelastic regions. However, one can remove some of this arbitrariness by matching the LOS model calculations to atomistic results of the total

energy of kink pair configurations. By adjusting the value of a to partition the elastic and core energies in eqs. (2.1) and (2.20) in such a way as to match the atomistic kink-pair energies at zero stress (obtained independently for the EAM and MEAM potentials), one can relate the value of the core width to the size of a region that contains the inelastic contribution to the total energy. Following these approach, we obtain values of $0.7b$ (EI) and $0.8b$ (LT) for the EAM case ($\Delta H_0 = 1.63$ eV) and $0.2b$ and $0.5b$ for MEAM ($\Delta H_0 = 1.78$ eV). The fact that these are between half and a full Burgers vector may be indicative of the order of magnitude to be expected for this parameter. However, we emphasize that this is one attempt to establish the value of a using a physical criterion, but it is difficult to ascertain how accurate or valid it is relative to other approaches [73, 74, 75]. In any case, we believe this to be an interesting aspect of our calculations and worth reporting as an original application of LOS models.

2.6.3 Building 3D kink-pair models from 2D atomistic data

One of the advantages of studying straight dislocations is the existence of translational symmetry along the line direction, which generally reduces the study of its properties to quasi 2D structures that need only capture the minimum repeatable translational unit along the dislocation line. For screw dislocations, this length is of course the Burger’s vector, which is typically the shortest lattice vector of the crystal. For this reason, general dislocation properties can be efficiently and accurately calculated using thin atomistic supercells, which makes them amenable to electronic structure calculations. The existence of kink pairs breaks the translational symmetry of screw dislocations in bcc (and other) crystals. Being the fundamental

structure governing screw dislocation dynamics, this necessitates using 3D configurations which precludes the use of computationally demanding approaches such as DFT. Consequently, it has been a goal of the bcc plasticity community to assess whether 2D information such as what has been presented here (Secs. 2.5.1 and 2.5.2) suffices to capture 3D behavior when incorporated into efficient continuum models of dislocation line configurations.

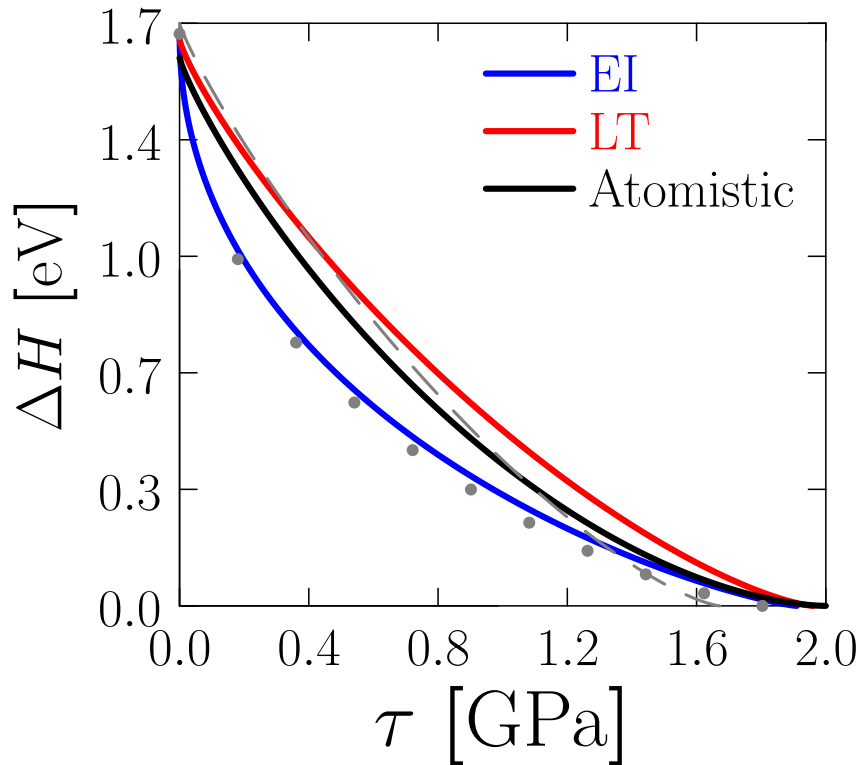


Figure 2.13: Comparison of the Kocks-Ashby-Argon expressions corresponding to the EI, LT, and atomistic models using EAM parameters for W. The gray dashed line corresponds to LT results assuming no asymmetry in the core energies and no stress-dependence of the Peierls potential ($p = 0.88$, $q = 1.37$), while the gray solid line is the equivalent EI curve ($p = 0.50$, $q = 1.29$).

Our calculations provide a testbed for this idea, in line with prior efforts [64], as they allow a direct comparison to strictly atomistic results of kink-pair configurations using EAM [49, 71]. This is illustrated in Fig. 2.13, where a good agreement between the LOS results and the atomistic calculations can be appreciated. As the figure shows, the LT model agrees with the atomistic result at low stresses, while the EI model produces a better match at high stresses. In the intermediate stress range, the EAM calculations lie in between both LOS approaches. Albeit restricted to very specific conditions, this verification result suggests that continuum models parameterized with atomistic 2D results can indeed be good approximants of full atomistic behavior in tungsten. While it is not clear how much of this agreement can be attributed to specific features of W, such as elastic isotropy or the choice of interatomic potential, we can cautiously conclude that LOS models that employ 2D information can be trusted to provide acceptable estimates of ΔH in other bcc metals.

2.6.4 Discussion of other works

Researchers have been calculating kink-pair activation enthalpies using continuum elastic models since the 1950s. As atomistic information involving fundamental dislocation properties has become available [62, 68], we have been able to enrich continuum formulations and increase their physical accuracy. There are several examples of this in the literature [67, 64, 60, 75], each highlighting one specific aspect of the physics of kink pairs in screw dislocations in bcc metals. However, to the best of our knowledge, this work constitutes the first LOS formulation to simultaneously integrate (i) the stress dependence of the Peierls potential, (ii) the asymmetry of the

dislocation core energies with respect to dislocation character, and (iii) the extraction of the core width by matching LOS results with atomistic results.

2.7 Conclusions

Our first conclusion is that one can successfully incorporate atomistic data obtained in quasi-2D conditions into continuum elastic models of 3D kink-pair configurations. We have demonstrated that the stress dependence of the Peierls potential and results for core energies as a function of dislocation character can be integrated into elastic interaction and line tension models in a straightforward manner. Moreover, we report a slight asymmetry in the core energies about the edge orientation in W , in accordance with a periodicity of $(0, \pi)$ for the dislocation character space in bcc metals.

The asymmetry in the dislocation core energies accounts for no more than 10% difference in left and right kink energies (compared to no less than 20% in atomistic results) and results in very slight variations in their spreading lengths. Thus, we conclude that, while they are likely one of several contributions to this energy asymmetry, core energies alone cannot capture it in its entirety. However, a representation of core energies in terms of the core width parameter is helpful to extract the value of this parameter by matching to atomistic data. In our particular case, we find that this core width is always less than one Burgers vector distance.

Including the stress dependence of the Peierls potential in the models appears to shift the athermal stresses to higher values compared to when just the zero stress potential is used, more in line with the atomistic values of the Peierls stress. However, this effects is small as well.

Finally, our results suggest that atomistic calculations of kink-pair configurations result in activation enthalpies that are in between elastic interaction and line tension predictions. In particular, at low stresses atomistic data agree better with line tension calculations, while at high stresses the agreement is better with full elastic models.

2.8 Fitting procedure of the stress dependence of the Peierls potential

Here we explain how to introduce the resolved shear-stress dependence in eq. (2.10). The τ -dependence enters through the parameters U_0 and α and our goal here then is to obtain compact expressions for $U_0(\tau)$ and $\alpha(\tau)$. To this end, we first plot the values of U_0 and α with stress in Fig. 2.14 and 2.15 for the EAM and MEAM potentials, respectively.

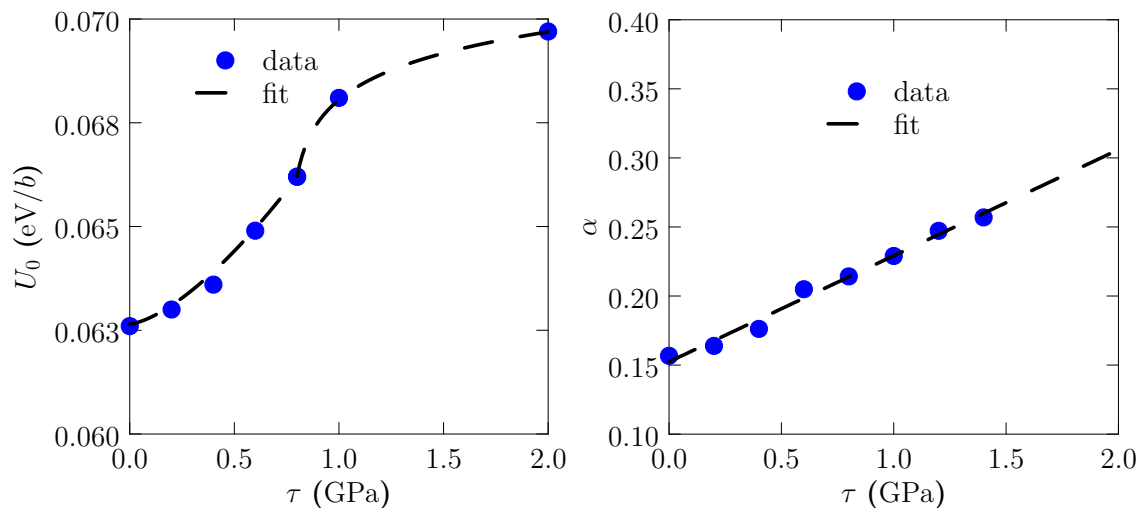


Figure 2.14: Fitting of U_0 and α for the EAM potential

As the figures show, generally there is a nonlinear dependence of U_0 with stress

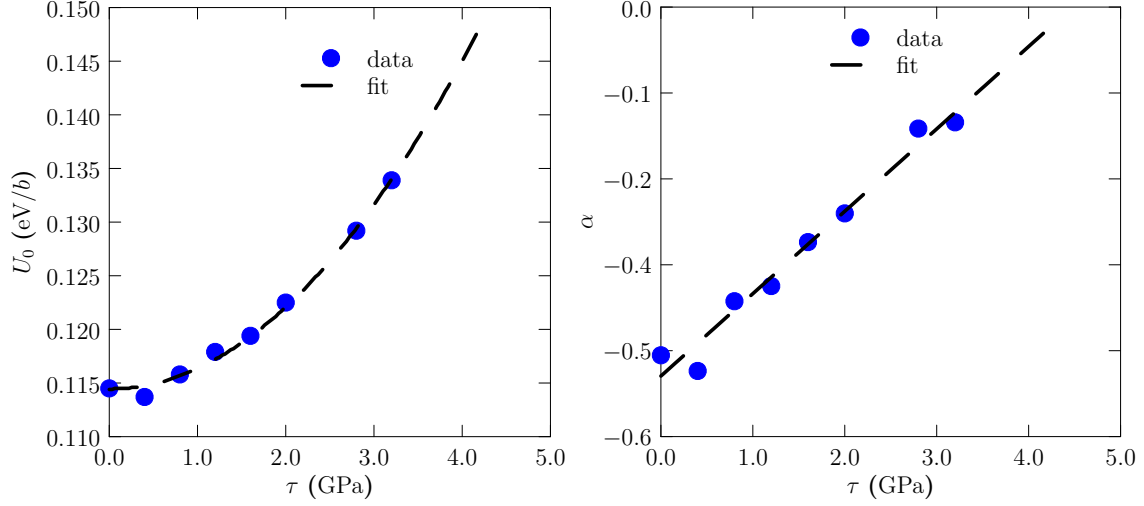


Figure 2.15: Fitting of U_0 and α for the MEAM potential

and a linear one for α . Consequently, we use power laws for $U_0(\tau)$ and linear relationships for $\alpha(\tau)$.

- Fitting of U_0 :

- EAM: Due to the change of convexity of the EAM U_0 data, we split the fitting into two regions.

1. In the low stress region, $\tau \leq 0.8$ GPa,

$$U_0(\tau) = 0.005\tau^{1.49} + 0.06 \quad (2.22)$$

2. In the high stress region, $\tau > 0.8$ GPa,

$$U_0(\tau) = 0.21(\tau - 0.7643)^{0.005} - 0.14 \quad (2.23)$$

- MEAM:

$$U_0(\tau) = 0.003(\tau - 0.13)^{1.6742} + 0.11 \quad (2.24)$$

with U_0 expressed in [eV/b] when τ is expressed in GPa.

- Fitting of α :

1. EAM:

$$\alpha = 0.077\tau + 0.152 \quad (2.25)$$

2. MEAM:

$$\alpha = 0.115\tau - 0.515 \quad (2.26)$$

with α non-dimensional when τ is in GPa.

We emphasize that these expressions have no implied physical meaning and are simply used for convenience in the range of stresses considered here.

2.9 Fitting of core energy data

As it was shown in Section 2.2.0.2, dislocation core energies expressed as:

$$e_c(\theta, a) = f(\theta) + g(\theta) \log\left(\frac{a}{b}\right)$$

where both $f(\theta)$ and $g(\theta)$ are Fourier series of the type:

$$y(\theta) = c_0 + \sum_{k=1}^3 c_k \sin(2i\theta) + d_k \cos(2i\theta)$$

Note that this form for $f(\theta)$ and $g(\theta)$ depends only on θ , with the a -dependence contained exclusively in the logarithmic term. This mimics the partition represented by eq. (2.1). The coefficients in these expressions are obtained by least-squares fitting to the atomistic data points obtained from Fig. 2.2) by varying a and θ , and are listed in Table 2.2. $f(\theta)$ and $g(\theta)$ are plotted as a function of θ in Fig. 2.16 along with the corresponding Fourier series curves for the EAM and MEAM potentials.

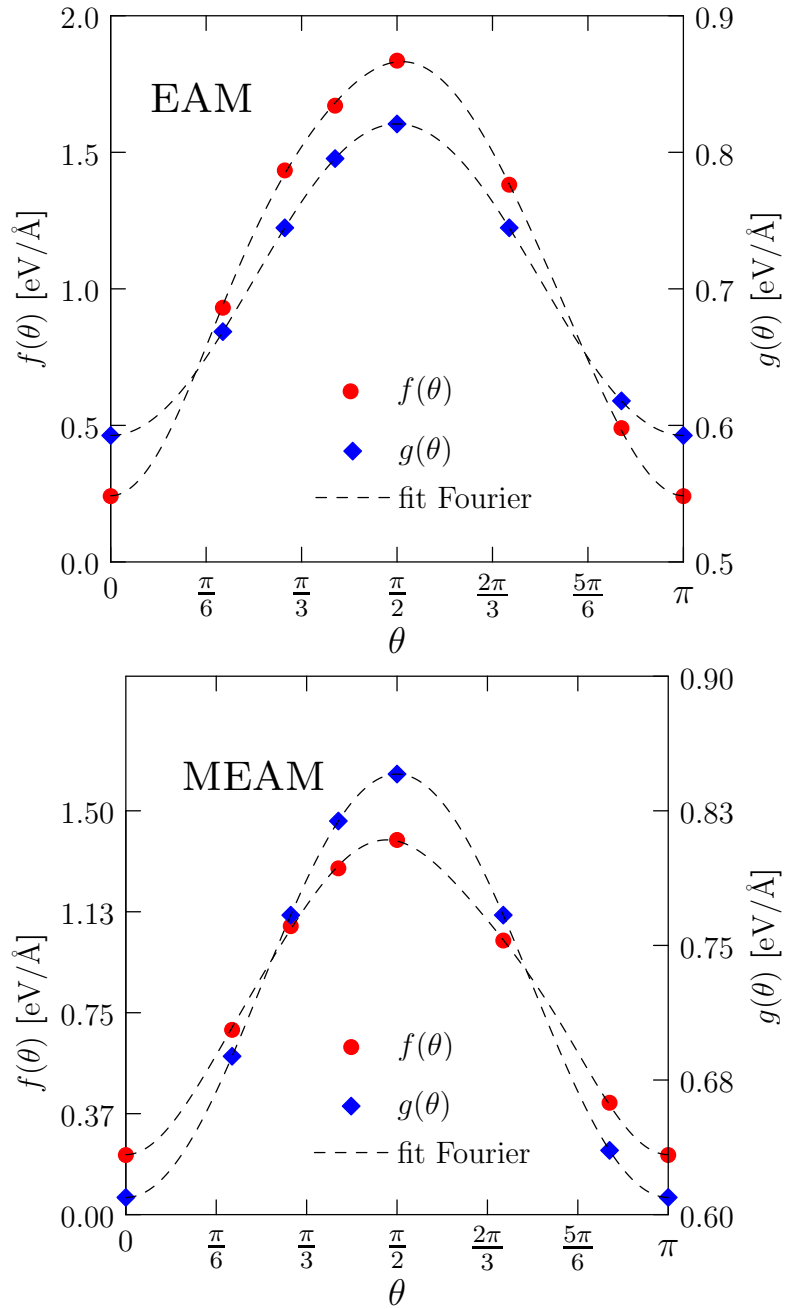


Figure 2.16: Dependence of the dislocation core energy terms f and g on dislocation character for (a) EAM and (b) MEAM interatomic potentials.

Table 2.1: Interatomic potential-specific parameters. The top half of the table includes atomistic parameters used in the LOS models: a_0 is the lattice constant, τ_P is the Peierls stress, U_{lk} and U_{rk} are the energies of left and right kinks, respectively, and $\Delta H_0 = U_{\text{lk}} + U_{\text{rk}}$ is the zero-stress kink-pair activation enthalpy. The bottom half of the table lists outputs of the LOS model calculations, separated between EI and LT calculations: a is the core width, p and q are the exponents of the phenomenological kink-pair enthalpy expressions, ΔH_0^* is the intercept of the kink-pair activation enthalpy with the vertical axis, and τ_a is the stress at which the activation enthalpy vanishes, equivalent to the athermal stress in experimental tests.

	EAM		MEAM	
a_0 [Å]	3.19		3.14	
τ_P [GPa]	2.0		3.4	
U_{lk} [eV]	0.71		0.81	
U_{rk} [eV]	0.92		0.99	
ΔH_0 [eV]	1.63		1.80	
	EI	LT	EI	LT
a [b]	0.70	0.80	0.15	0.50
p	0.41	0.83	0.45	0.80
q	1.05	1.38	1.09	1.46
ΔH_0^* [eV]	—	1.68	—	1.84
τ_a [GPa]	1.84	1.99	3.22	3.61

Table 2.2: Values of the Fourier coefficients in eq. (2.21) for the EAM and MEAM potentials.

Potential	function	c_0	c_1	d_1	c_2	d_2	c_3	d_3
EAM	f	1.1017	0.0149	-0.7895	0.0082	-0.0634	-0.0331	-0.0078
	g	0.7067	-	-0.1141	-	-	-	-
MEAM	f	0.8390	0.0092	-0.5730	-0.0191	-0.0325	-0.0118	-0.0122
	g	0.7275	-	-0.1179	-	-	-	-

CHAPTER 3

Edge dislocation model with superjogs in Nb-Mo-Ta-W HEA

Refractory multi-element alloys (RMEA) with body-centered cubic (bcc) structure have been the object of much research over the last decade due to their high potential as candidate materials for high-temperature applications. Most of these alloys display a remarkable strength at temperatures above 1000°C, which cannot be explained by the standard model of bcc plasticity dominated by thermally-activated screw dislocation motion. Recent research on Nb-Mo-Ta-W alloys points to a heightened role of edge dislocations during mechanical deformation, which is generally attributed to atomic-level chemical fluctuations in the material and their interactions with dislocation cores during slip. However, while this effect accounts for levels of strength that are much larger than what might be found in a pure metal, it is not sufficient to explain the high yield stress found at high temperature in Nb-Mo-Ta-W. In this work, we propose a new strengthening mechanism based on the existence of thermal super-jogs in edge dislocation lines that act as strong obstacles to dislocation motion, conferring an extra strength to the alloy that turns out to be in very good agreement with experimental measurements. The basis for the formation of these super-jogs is found in the unique properties of RMEA, which display vacancy formation energy distributions with tails that extend into negative values. This leads to spontaneous,

i.e., athermal, vacancy formation at edge dislocation cores, which subsequently relax into atomic-sized super-jogs on the dislocation line. At the same time, these super-jogs can displace diffusively along the glide direction, relieving with their motion some of the extra stress, thus countering the hardening effect due to jog-pinning. We implement these mechanisms into a specially-designed hybrid kinetic Monte Carlo/Discrete Dislocation Dynamics approach (kMC/DD) parameterized with vacancy formation and migration energy distributions obtained with machine-learning potentials designed specifically for the Nb-Mo-Ta-W system. The kMC module sets the timescale dictated by thermally-activated events, while the DD module relaxes the dislocation line configuration in between events in accordance with the applied stress. We find that the balance between super-jog pinning and super-jog diffusion confers an extra strength to edge dislocations at intermediate-to-high temperatures that is in remarkable agreement with experimental measurements in equiatomic Nb-Mo-Ta-W and several other RMEA. We derive an analytical model based on the computational results that captures this improved understanding of plastic processes in these alloys and explains the experimental data.

3.1 Introduction

Since their inception in the 1990s [137, 138], high entropy alloys (HEA) have attracted a great deal of attention due to a unique combination of properties seldom found in other material types [139, 140, 141, 142, 143, 144, 7, 145, 146]. This makes them potentially very attractive as candidate materials for a number of technological applications in harsh environments such as elevated temperatures, irradiation, or corrosion [147, 148, 149, 150]. The basic idea behind creating alloys of this type

is to combine a number of elements (typically four or more) in similar proportions to achieve solid solution phase stability through the large configurational entropy of the system. Due to the large chemical and configurational space available to create these materials, several hundred different HEA combinations now exist, each with their own distinct compositions, structure, and properties [151, 152, 153]. The large volume of research on the topic over the last decade has resulted in a fast-evolving field full of new findings, unexplained results, and unresolved controversies. The reader is referred to the numerous reviews and monographs published over the last several years for more details [139, 140, 141, 142, 143, 144, 7, 145, 154, 155]. Note that, while the term ‘multicomponent’ or ‘multielement’ alloys is sometimes preferred in the literature over ‘high-entropy’ alloys (particularly when the number of elemental constituents is less than five), here we use all interchangeably.

Among the different materials proposed, refractory multi-element alloys (RMEA) are a special class of alloys composed of typically four or more refractory metal elements (Nb, Mo, Ta, V, W, Cr, Hf, Zr). These systems generally crystallize into a single body-centered cubic (bcc) phase, found to be stable up to very high temperatures [7, 6, 156, 157, 158, 159, 160, 161]. RMEA display sluggish self-diffusion rates [162, 163, 164, 165] and, similar to their pure bcc metal counterparts, suffer from a lack of ductility at low temperatures [6, 166]. However, they retain a high strength and ductility at high temperature, making them attractive candidates for structural applications in the power, aerospace, or nuclear sector [147, 148, 149, 167, 154].

While the deformation mechanisms of bcc metals and their alloys are relatively well understood, the mechanical response of chemically complex alloys at high temperature is still under vigorous investigation. Perhaps one of the most crucial aspects separating standard bcc behavior with that of RMEA is the role played by screw and

edge dislocations during plastic deformation. Although the experimental evidence is still inconclusive [168, 169, 170], recent research points to the increased importance of edge dislocation slip relative their role in pure metal bcc systems and dilute alloys [171, 172, 173, 3]. Because chemical fluctuations in HEA take place at the atomistic scale, molecular dynamics (MD) has become the preferred tool to simulate dislocation processes in these systems. Indeed, MD simulations have been used to characterize the intrinsic roughness of dislocation lines [174, 171, 175], the effect of short-range order (SRO) [171, 3, 176] on alloy properties, and dislocation mobilities [3, 177]. For example, MD simulations have convincingly shown that the lattice resistance aided by SRO (intrinsic strengthening) in bcc RMEA can reach up to 1 GPa at low temperatures. However, their contribution is much diminished as the temperature increases, and it alone cannot account for the observed high-temperature dependence of alloy strength.

In contrast, an often overlooked feature of multi-element systems is the statistical nature of defect properties due to their compositional heterogeneity [178, 179, 180, 181, 182]. Properties such as point defect formation energies, planar defect energies, or dislocation core energies are defined by distributions whose variance generally correlates with the number of elements in the alloy [180, 181]. In particular, the thermal concentration of point defects in pure refractory metals is typically negligible on account of their relatively high formation energies. However, in HEA the low energy tails of defect energy distributions can lead to non-insignificant defect concentrations, even in conditions where these would be several orders of magnitude lower if one considered only the individual alloy elements. Moreover, defect formation energies can be substantially reduced at material inhomogeneities such as dislocation cores, material interfaces, precipitates, etc. [183, 184]. For vacancies, which display formation

energies 2~3 times lower than self-interstitial atoms in metals, a side effect of above two effects combined (broad energy distributions together with heterogeneous defect nucleation), is the possibility for non-thermal formation, i.e., the spontaneous existence of vacancies at any temperature at pre-existing microstructural defects.

Of particular interest is the formation of vacancies at or near edge dislocation cores, which is thermodynamically more favorable within the compressive region of the stress field [184]. Topologically, vacancies on dislocation lines can be regarded as elementary (super)jogs that can only move by nonconservative means (e.g., *jog dragging*) [185, 186, 187]. As such, the existence of super-jogs on a dislocation line can lead to extra strengthening, as has been seen in a number of systems at high temperature [188]. Moreover, owing to the low energy tails of the vacancy formation energy distributions, it is reasonable to expect a nonzero concentration of super-jogs on edge dislocation lines in even at low temperatures. The main objective of this work is to quantify this specific effect in a model RMEA and establish its viability as a high-temperature strengthening mechanism. More generally, we aim to study the behavior of edge dislocations, and their impact on alloy strength, when single-valued point defect energies are replaced by energy distributions.

Due to MD's intrinsic limitations when it comes to simulating thermally-activated mechanisms and their role in dislocation motion, here, following our line of work in previous publications [189, 190], we conduct stress-driven simulations of edge dislocation motion as a function of temperature using a combined approach consisting of discrete dislocation dynamics (DD) and kinetic Monte Carlo (kMC). Our DD/kMC model captures the thermal formation and evolution of vacancies/super-jogs on edge dislocations and quantifies their effect on dislocation motion as a first attempt to embed some of the complexities of the highly-random alloy into a mesoscale framework

with the aim of capturing time and length scales more suitable for experiments, as compared to MD. We focus on equiatomic Nb-Mo-Ta-W alloys, for which robust interatomic potentials exist [191, 4, 192], as well as a wealth of experimental data [193, 194, 158, 195, 196, 197], and carry out calculations of vacancy energetics to parameterize the model without fitting to any experimental measurements.

The paper is organized as follows. First, we provide the theoretical framework for DD/kMC model. This is followed by a description of the numerical implementation and the atomistic calculations performed to parameterize the model to the alloy of choice. Next we present results of the strength of the alloy as a function of temperature and strain rate. We finalize the paper with a discussion of the results and the conclusions.

3.2 Theory and models

3.2.1 Monte Carlo model of non-conservative edge dislocation motion

The key element of the modeling approach is a stochastic model based on the residence-time algorithm to simulate dislocation evolution under stress. The time scale is governed by a set of thermally-activated events that punctuate periods of standard dislocation glide. As such, dislocation evolution proceeds by way of a series of super-jog processes intercalated by stress-assisted glide. Here we consider two distinct thermal processes, which are schematically illustrated in Fig. 3.1:

1. At any point during a simulation, a super-jog may appear on the dislocation line by thermal nucleation of a vacancy (process shown in Fig. 3.1a). Such nucleation is subjected to equilibrium constraints so that the linear concen-

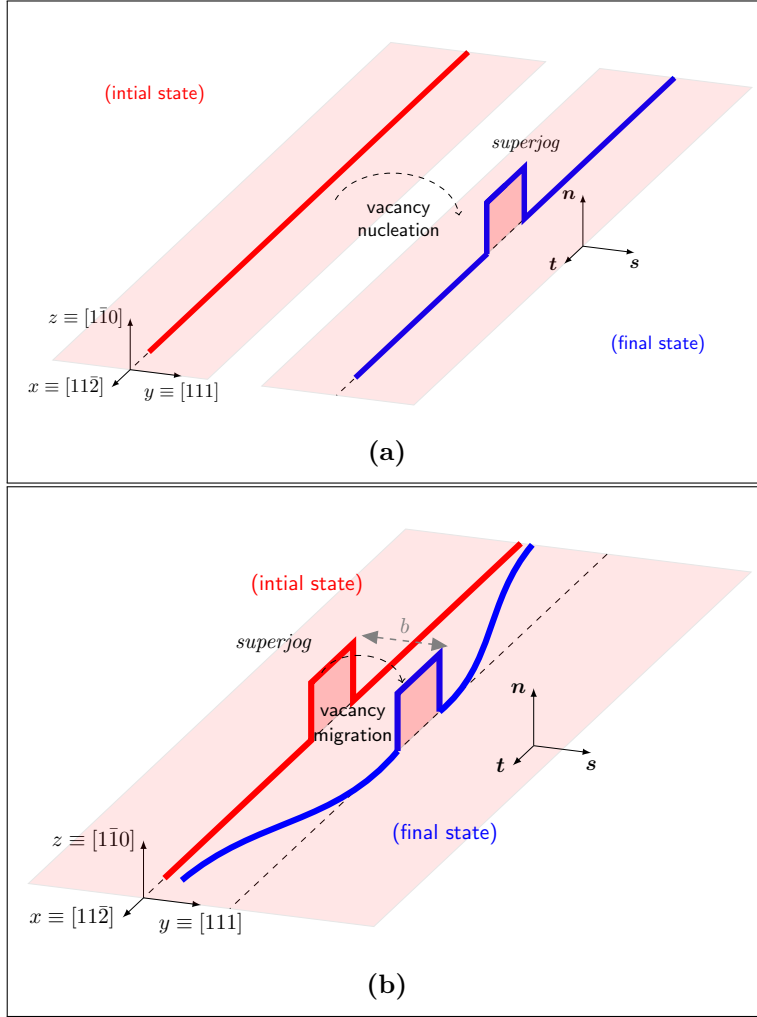


Figure 3.1: Modes of super-jog evolution. (a) super-jog generation on a straight dislocation line. This mode of motion requires vacancy nucleation. (b) Direct translation along the slip direction \mathbf{s} . This mode of motion requires a vacancy jump.

translation of super-jogs remains within thermal limits. For this, the dislocation line is subdivided into irreducible segments of length $w = a_0\sqrt{6}/3$ (equal to the periodicity along the line direction $1/6\langle 112 \rangle$), where a_0 is the lattice parameter.

The insertion rate of super-jogs per unit length is:

$$q_n^{\text{jog}}(T; t) = \nu_0 [\ell/w - n(t)] (1 - n(t)/n_0(T)) \quad (3.1)$$

where T is the absolute temperature, ν_0 is a temperature-independent vacancy nucleation attempt frequency, $n(t)$ is the number of super-jogs at time t (the current number of super-jogs), and $n_0(T)$ is the equilibrium super-jog concentration (to be defined in Section 3.2.3). Here, the ratio ℓ/w represents the number of potential nucleation sites on a dislocation with total length ℓ for a super-jog to form, while $[\ell/w - n(t)] > 0$ represents the number of available nucleation sites¹. The ‘height’ of a jog segment is the unit lattice parameter along the y -direction: $h = \|^{1/2}[110]\| = a_0\sqrt{2}/2$. Note that, while thermodynamically possible, super-jog reabsorption is highly unlikely because it requires either the arrival of self-interstitial atoms or emission of vacancies, both of which are discarded in this model due to their high penalizing energies.

2. Existing super-jogs can translate along the glide x -direction via diffusive jumps to a location separated one Burgers vector’s distance from the original position (Fig. 3.1b). This process is akin to the jump of a vacancy located on the edge dislocation core along the glide $[111]$ direction, which corresponds to a nearest-neighbor jump in a bcc lattice. The rate of this process can be written as:

$$q_m^{\text{jog}}(T) = \nu'_0 \exp(-\Delta H_m^\perp + \Delta E_{\text{el}}^{\text{jog}}/kT) \quad (3.2)$$

where ν'_0 is the jump attempt frequency and ΔH_m^\perp is the vacancy migration enthalpy, which incorporates contributions from the stress state at the super-jog location, and $\Delta E_{\text{el}}^{\text{jog}}$ is the extra elastic energy incurred by the bending of

¹The function $[x]$ is the mathematical floor function.

dislocation segments adjacent to the super-jog (as shown in Fig. 3.1b). Both of these quantities will be defined and calculated in Sec. 3.2.3. The above rate must be defined for both forward and backward jumps, with the direction of the jump assigned by defining the resolved shear stress as positive when it creates a force aligned with the glide direction.

A summary of the properties of each type of event is given in Table 3.1.

Table 3.1: Summary of super-jog transitions.

Segment	Rate	Definition	Distance
super-jog (nucleation)	q_n^{jog}	eq. (3.1)	(super-jog dimensions: $h \times w$)
super-jog (forward/backward)	q_m^{jog}	eq. (3.2)	b

Using kMC, the set of event rates is sampled at each iteration and the appropriate process is selected and executed. Time is evolved as a Poisson variate:

$$\delta t = -\frac{\log \eta}{R_t} \quad (3.3)$$

where η is a uniform random number, $R_t = \sum_{\alpha=n,m} \left(\sum_j q_\alpha^{\text{jog}} \right)$, and the subindices α and i apply to the type of transition (‘ n ’ nucleation, ‘ m ’ migration) and to the number of existing super-jogs, respectively. In between thermal events, i.e., during a time δt , the dislocation evolves elastically in response to the existing stresses using a suitable DD model (explained in Sec. 3.2.2). A flow diagram of the numerical method is given in 3.6, Fig. 3.9.

3.2.2 Dislocation dynamics model

The DD model must be sensitive to the scale of discrete steps on the dislocation line to capture the formation of vacancy induced jogs. As such, the main difference between the dislocation dynamics approach used here and standard DD codes [?] is that the positions of the nodes delimiting the jogs are constrained to have specific lengths. Beyond that, dislocation segments interact in an isotropic elastic manner with one another using the elastic constants of the alloy obtained with the potentials described in Sec. 3.2.3.

As is customary in most DD formulations, the segment glide velocity v_i^{gl} is linearly dependent on stress as:

$$v^{\text{gl}} = \frac{b\Delta\tau}{B_t(T, \theta)} \quad (3.4)$$

where $b = \|\mathbf{b}\|$ is the Burgers vector's modulus, θ represents the dislocation character ($\cos \theta = \mathbf{s} \cdot \mathbf{t}$, where $\mathbf{s} = b^{-1}\mathbf{b}$ is the slip direction and \mathbf{t} the local line tangent), B_t is a temperature-dependent drag coefficient, and $\Delta\tau$ is the excess glide stress, obtained as the difference between the resolved shear stress τ_{RSS} calculated at the segment or nodal position and a temperature and dislocation character dependent critical stress, τ_c which is a material constant.

$$\Delta\tau = \tau_{\text{RSS}} - \tau_c(T, \theta) \quad (3.5)$$

with:

$$\tau_c(T, \theta) = \tau_c^{\text{screw}}(T) \cos^2 \theta + \tau_c^{\text{edge}}(T) \sin^2 \theta \quad (3.6)$$

Likewise, for the drag coefficient B_t , the same dependences on T and θ are used:

$$B_t(T, \theta) = B^{\text{screw}}(T) \cos^2 \theta + B^{\text{edge}}(T) \sin^2 \theta \quad (3.7)$$

The parameters $\tau_c^{\text{screw}}(T)$, $\tau_c^{\text{edge}}(T)$, $B_c^{\text{screw}}(T)$, and $B_c^{\text{edge}}(T)$ are temperature dependent critical stresses and glide friction coefficients for screw and edge coefficients, respectively. Here we employ coefficients derived from recent results by Yin [3] for the Nb-Mo-Ta-W equiatomic system, shown in Fig. 3.2. The numerical expressions for the data in the figure used in the present DD simulations are provided in Table 3.2. Here we use a shear modulus of $\mu = 94$ GPa and a Poisson ratio of $\nu = 0.33$ [4].

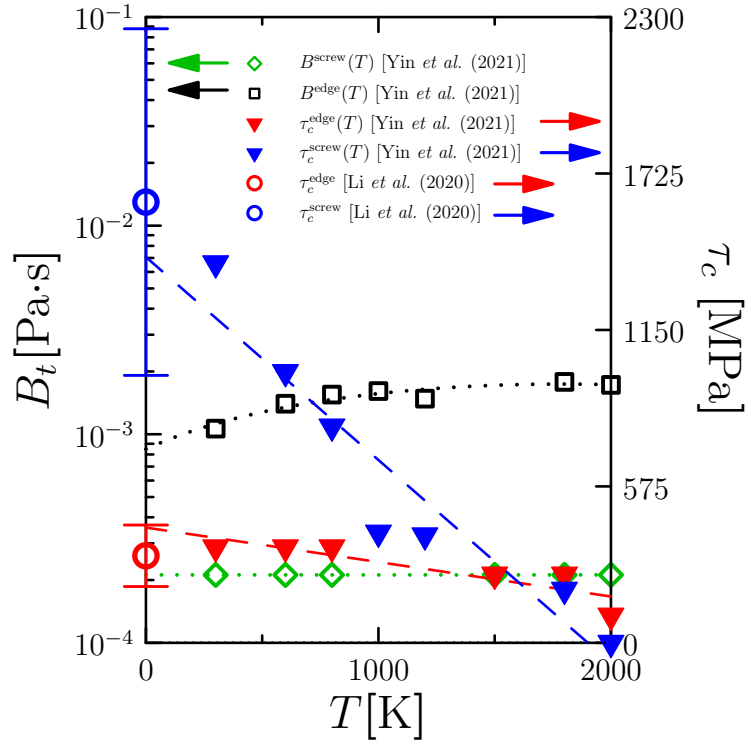


Figure 3.2: Dislocation critical stresses and friction coefficients from ref. [3]. The two data points for screw and edge at 0 K were obtained using a SNAP potential [4].

The geometry used in the DD simulations follows a Cartesian coordinate system with axes $x \equiv [11\bar{2}]$, $y \equiv [111]$, and $z \equiv [1\bar{1}0]$ representing, respectively, the dislocation line direction, the plane normal, and the glide direction (along the Burg-

Table 3.2: Numerical expressions use for the temperature dependence of the coefficients plotted in Fig. 3.2. T is the absolute temperature in K.

Parameter	Expression	Units
$B^{\text{screw}}(T)$	$3.44 \times 10^{-4} \ln(T) - 8.37 \times 10^{-4}$	Pa·s
$B^{\text{edge}}(T)$	2.12×10^{-4}	Pa·s
$\tau_c^{\text{screw}}(T)$	$1418.0 - 0.7T$	MPa
$\tau_c^{\text{edge}}(T)$	$423.6 - 0.1T$	MPa

ers vector \mathbf{b}). With such an orientation, an external stress tensor with τ_{yz} as the only nonzero component is applied and added to the total segment-segment elastic stresses at each point. While a shear stress τ_{yz} produces a net force on segments aligned with the z direction, i.e., jog segments, we only allow slip on close-packed $\{110\}$ these segments and thus these segments cannot glide conservatively during the simulations. They can, however, move non-conservatively, which as will be shown is dealt with by the kMC module.

3.2.3 Model parameterization

3.2.3.1 Atomistic calculations of vacancy formation and migration energies

The two main processes described earlier are characterized by event rates that involve vacancy transitions at or next to edge dislocation cores. The first one, thermal nucleation of super-jogs, is governed by the vacancy formation energy at edge disloca-

tion cores, $\Delta E_f^{V@^\perp}$. The second one, super-jog translation along the glide direction, is represented by the migration energy along the glide direction of vacancies lying on edge dislocation cores, $\Delta E_m^{0\rightarrow 1}$. For simplicity going forward, we use shorthand notation to refer to $\Delta E_f^{V@^\perp}$ and $\Delta E_m^{0\rightarrow 1}$, as E_f^\perp and E_m^\perp , respectively.

To calculate the distribution of E_f^\perp and E_m^\perp , we first construct an edge dislocation dipole in an atomistic supercell using the same procedure described in detail by Hossain and Marian [59]. In this work we use a spectral neighbor analysis potential (SNAP) for the Nb-Mo-Ta-W system, which has been trained against a comprehensive materials database [198, 4]. A value of $a_0 = 3.24 \text{ \AA}$ is obtained for the lattice parameter of the alloy using this potential.

Fig. 3.3a shows the relaxed atomic structure of the dipole visualized according to common neighbor analysis and the dislocation extraction algorithm using `Ovito` [199], while Fig. 3.3b shows a side view with the two edge dislocation locations (‘ \perp ’ symbols) and two atomic positions, labeled ‘0’ and ‘1’, at and near the dislocation cores. E_f^\perp is calculated at different ‘0’ locations along the dislocation line. Note that while these locations are crystallographically equivalent, they are ‘chemically’ different, which is the source of the variability in E_f^\perp .

For its part, E_m^\perp is calculated as the migration energy between points ‘0’ and ‘1’, which are separated by an amount equal to the first nearest neighbor distance (equivalent to the Burgers vector’s modulus) with both positions located on the same $[11\bar{2}]$ plane. The corresponding normalized distributions, $p(E_f^\perp)$ and $p(E_m^\perp)$, are provided in Fig. 3.4.

As a point of comparison, the statistical means of $p(E_f^\perp)$ and $p(E_m^\perp)$, denoted by \bar{E}_f^\perp and \bar{E}_m^\perp are tabulated here for the random Nb-Mo-Ta-W system along with

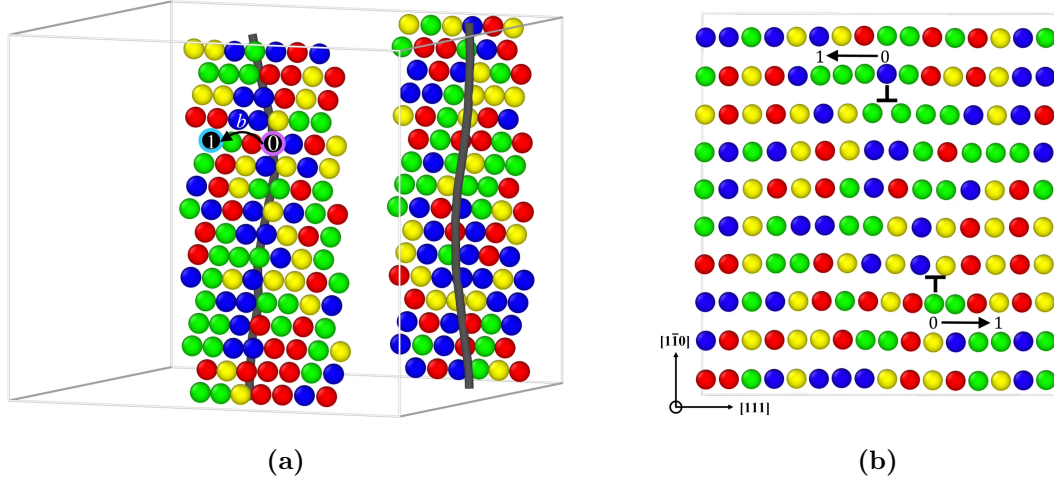


Figure 3.3: Relaxed edge dislocation dipole utilized for vacancy formation energy calculations. (a) Atomistic representation according to common neighbor analysis and equivalent line representation, both extracted using Ovito [5]. (b) Side view showing the edge pole dislocation locations (\perp symbols) and atoms from three consecutive $[11\bar{2}]$ planes. Atoms are colored by chemical species (green for Nb, red for Mo, blue for Ta, and yellow for W). The atomic positions ‘0’ and ‘1’ (of significance in the text) are indicated in both images. The distance between positions 0 and 1 is equal to the first nearest neighbor distance (i.e., one Burgers vector) with both positions located on the same $[11\bar{2}]$ plane.

the corresponding formation and migration energies in bulk Nb-Mo-Ta-W and in the gray material. As Table 3.3 shows, formation energies are substantially lower than in the bulk (averages of 0.93 versus 2.40 eV). Critically, however, some of the calculated energies are zero or negative, introducing the possibility for spontaneous vacancy formation. In other words, thermal vacancies are expected to form with considerable ease at edge dislocation cores compared to bulk positions, but, most importantly, in certain locations vacancies will form athermally to lower the total local configurational energy around the dislocation. This essentially implies that

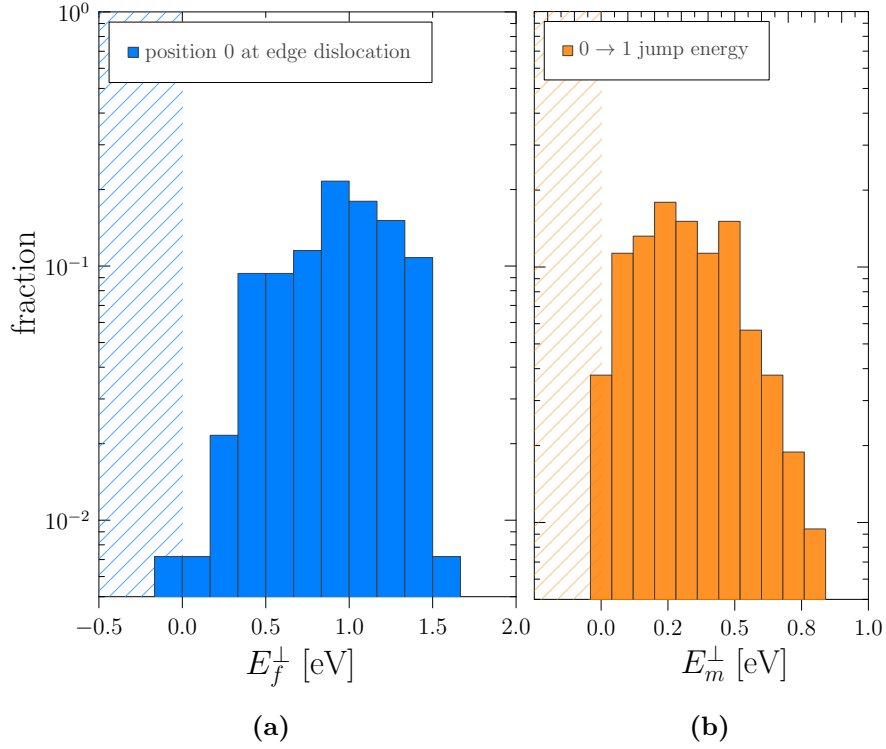


Figure 3.4: (a) Vacancy formation energy distribution in the Nb-Mo-Ta-W alloy at position ‘0’ near the edge dislocation core in Fig. 3.3b. (b) Migration energy distribution for the 1→0 jump at the edge dislocation core positions shown in Fig. 3.4a. Negative energies (shaded area in the graphs) signal the spontaneous formation of vacancies and transitions, respectively.

super-jogs, which are the manifestation of monovacancies in terms of dislocation lines, may naturally exist along the edge dislocation in equilibrium conditions at any temperature.

Table 3.3: Mean energies for the vacancy formation and migration energy distributions at dislocations cores (‘ \perp ’, highlighted in red) and in the bulk (‘V’), for both the random Nb-Mo-Ta-W system and the *gray* alloy. The relevant energies are highlighted in red.

Energies [eV]	Nb-Mo-Ta-W	‘gray’ alloy
\bar{E}_f^\perp	0.93	–
\bar{E}_f^V	2.40	2.62
\bar{E}_m^\perp	0.32	–
\bar{E}_m^V	1.71	1.53

3.2.3.2 Activation enthalpies and attempt rates

Next we turn our attention to the parameters in eqs. (3.1) and (3.2). The key quantity to define in eq. (3.1) is the thermal concentration of super-jogs, $n_0(T)$. In general, $n_0(T) = n_0^* \exp(-E_f^\perp/kT)$, where n_0^* is a pre-factor determined by the crystal geometry. In our case, n_0^* is set by the inverse of the periodicity along the the dislocation line direction, which is equal to $1/w$.

Similarly, the jump rate in eq. (3.2) can be expressed as:

$$q_m^{\text{jog}}(T) = 2\nu'_0 \exp\left(-\frac{\Delta E_m^\perp + \Delta E_{\text{el}}^{\text{jog}}}{kT}\right) \sinh\left(\frac{\Delta\tau (wb^2)}{kT}\right) \quad (3.8)$$

This expression captures forward and backward jumps² through the sinh term, whose argument is the work done by the excess stress (refer to eq. (3.5)) to move the super-

²Forward jumps are taken as those for which the stress tensor projected along the Burgers vector’s direction results in a positive resolved shear stress along the glide direction, i.e., when $(\boldsymbol{\sigma} : \mathbf{b}) \cdot \mathbf{s} > 0$.

jog a distance b . The area swept during the process is equal to the width of the super-jog times b , i.e., wb . The product wb^2 comes out to approximately $1.2\Omega_a$ ($\Omega_a = a_0^3/2$). $\Delta E_{\text{el}}^{\text{jog}}$ is the extra elastic energy due to the bending of the dislocation segments adjacent to the super-jog, which is obtained directly by the DD module of the code.

With respect to the attempt frequencies ν_0 and ν'_0 , here we adopt a value of 10^{12} Hz for both.

3.3 Results

3.3.1 Thermal super-jog concentration

Fig. 3.5 shows an Arrhenius plot of the thermal concentration of super-jogs, n_0 , as a function of temperature in edge dislocations. The figure includes the lower-bound n_0 , characterized by the mean energy of the formation energy distribution in Fig. 3.4a, given in Table 3.3 as $\bar{E}_f^\perp = 0.93$ eV, and also the simulated n_0 , obtained by sampling from the distribution in Fig. 3.4a according to eq. (3.1) (obtained from 10 independent samplings at each temperature). As the data show, the *effective* formation energies are much lower than 0.93 eV, ranging from 0.02 eV below 400 K to 0.15 eV above 1000 K. Both distributions converge to the common prefactor of $n_0^* = 1/w$ at very high temperatures. Overall the simulated thermal concentration of super-jogs is orders of magnitude larger than that given by the Arrhenius form of n_0 . Moreover, it displays an almost athermal dependence with T , particularly at low temperatures. This is yet another manifestation of the unique properties of compositionally-complex alloys such as Nb-Mo-Ta-W, which display enhanced

thermal defect concentrations due to asymmetric samplings of $p(E_f^\perp)$.

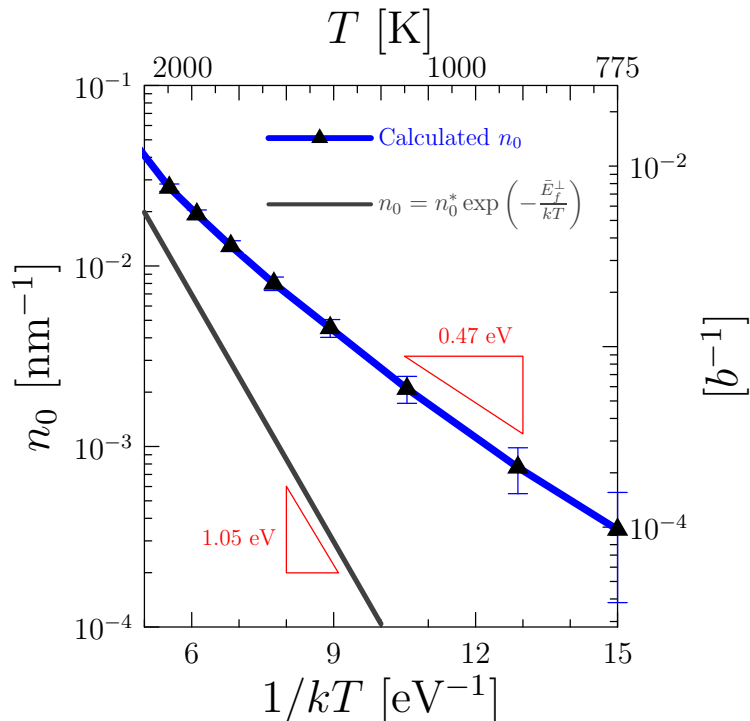


Figure 3.5: Arrhenius plot of the thermal concentration of super-jogs, n_0 , as a function of temperature on edge dislocations. The figure includes both the lower-bound n_0 , characterized by the mean energy of the formation energy distribution in Fig. 3.4a, $\bar{E}_f^\perp = 0.93$ eV, and also the simulated n_0 , obtained by sampling from the distribution in Fig. 3.4a according to eq. (3.1) (obtained from 10 independent samplings at each temperature).

3.3.2 Dislocation dynamics under stress

Next we track dislocation motion under stress. We simulate a Frank-Read source with a fixed length L pinned at its endpoints. L is generally obtained as $L \approx (\rho_d)^{-1/2}$, so that its value is consistent with the dislocation density in the material, ρ_d . Values as low as $\rho_d = 5 \times 10^{12} \text{ m}^{-2}$ have been reported in Nb-Mo-Ta-W [156, 200]. However,

this is three to four orders of magnitude smaller than dislocation densities measured in other bcc RMEA, such as $2 \times 10^{15} \text{ m}^{-2}$ in Ti-Nb-Hf-Ta [201], $2.1 \times 10^{16} \text{ m}^{-2}$ in Hf-Nb-Ti-Zr [202], or 10^{15} m^{-2} in V-Nb-Mo-Ta-W [195]. Thus, we take values of $1 \sim 2 \times 10^{15} \text{ m}^{-2}$ as being more representative of the dislocation density in the alloy. This gives rise to average dislocation source lengths on the order of $100 \sim 300b$. Note that, in accordance with the results in Fig. 3.5, these lengths are sufficient to contain at least one super-jog at temperatures above 580 K. The effect of ρ_d on the model results is further discussed in Sec. 3.4.3.

3.3.3 Time evolution of the plastic strain

The plastic strain, ε_p , is the response function in the DD simulations, and is calculated from the aggregate area swept by each dislocation segment during a time iteration [203, 204]. As such, in the DD/kMC simulations we track ε_p as a function of time at different temperatures and stresses. A representative example is shown in Fig. 3.6, where we plot the plastic strain versus time at different temperatures for a dislocation source with length $L = 150b$ containing two super-jogs under 1500 MPa of applied stress. While the ε_p - t curve for $\tau = 500 \text{ K}$ is smooth, indicating the absence of super-jog jumps, the rest of the curves display some roughness associated with sharp super-jog transitions of magnitude $\pm b$. Note that these transitions are both stress and temperature-assisted, as determined by eq. (3.8).

The graph shows that, for a fixed dislocation length and super-jog separation, higher temperatures lead to a faster dislocation evolution. This can all be attributed to the diffusional part of the dislocation dynamics, as the viscous contribution, governed by B^{edge} , displays practically no thermal dependence.

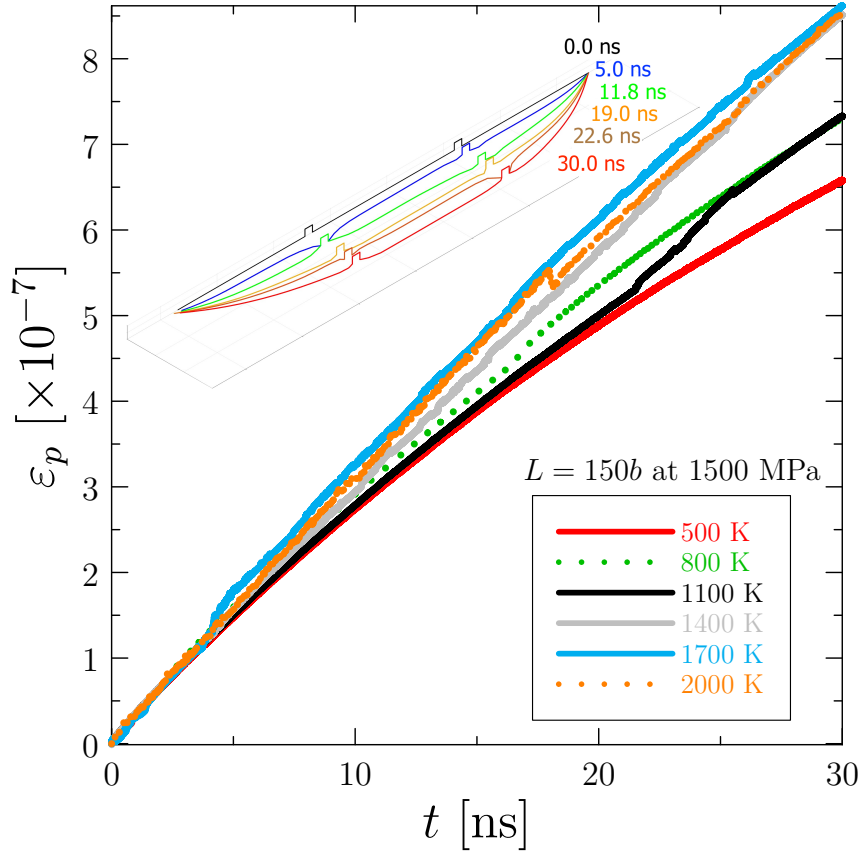


Figure 3.6: Plastic strain rate as a function of time at several temperatures under an applied stress of 1500 MPa for a dislocation source with a total length of $150b$ containing two super-jogs evenly spread at $+L/3$ and $+2L/3$. The inset shows an overlapping sequence of time frames of the dislocation configuration at 1700 K covering 30 ns of DD/kMC simulation.

3.3.4 Strain rate-temperature relations

First it is useful to note that the cases without super-jogs are trivially modeled by the Orowan equation for the ideal case of infinite dislocation lengths:

$$\dot{\epsilon}_p = \rho_d b v = \frac{\rho_d b^2}{B^{\text{edge}}} (\tau - \Delta\tau - \tau_c^{\text{edge}}) = \frac{\rho_d b^2}{B^{\text{edge}}} \left(\tau - \frac{\alpha\mu b}{L} - \tau_c^{\text{edge}} \right) \quad (3.9)$$

where, from Fig. 3.2, the only temperature dependence comes via the critical stress τ_c (B^{edge} is a constant, cf. Table 3.1). As such, the (plastic) strain rate given by eq. (3.9) is linear both in τ and T with a proportionality constant independent of temperature. From the values in Tables 3.1 and 3.4 and $1/L = \sqrt{\rho_d}$:

$$\dot{\epsilon}_p = 3.72 \times 10^5 (\tau - 850 + 0.1T) [\text{s}^{-1}] \quad (3.10)$$

Next we analyze all the ϵ_p - t curves of dislocation sources in the $75 < L < 310b$ range to extract the relationship between the plastic strain rate, $\dot{\epsilon}_p$, with temperature and stress. The results are shown in Fig. 3.7. Fig. 5.1a gives the stress dependence of $\dot{\epsilon}_p$ for a fixed line length of $150b$ containing two super-jogs. Fig. 5.1b shows its dependence with line length (all containing two super-jogs) for a fixed applied stress of 1000 MPa. Finally, Fig. 3.7c gives the ϵ_p - t relation as a function of the number of super-jogs on a $210b$ line at 1000 MPa. All three figures show cases of straight dislocations containing no-super-jogs for comparison. As expected, the super-jogs confer an extra strength to the dislocation, clearly seen at lower temperatures. This extra strength is negated at above 1100~1300 K, when super-jog diffusion becomes prolific at high temperatures. Thus, in general, the DD/kMC simulations validate the notion that as the temperature increases the super-jogs lose their strengthening power thanks to stress-assisted diffusion. However, that must be coupled to the fact that, as the temperature increases, dislocation lines contain more thermal super-jogs

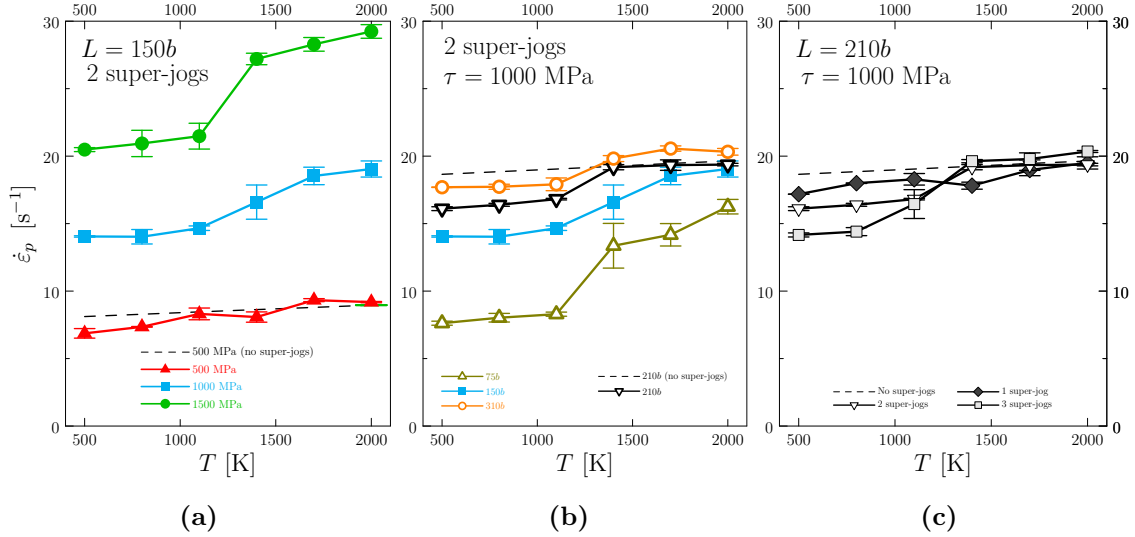


Figure 3.7: Plastic strain as a function of: (a) stress for a fixed line length of $L = 150b$ and fixed number of super-jogs (two), (b) line length for a fixed applied stress of 1000 MPa and fixed number of super-jogs (two), and (c) number of super-jogs for fixed stress (1000 MPa) and line length ($210b$). The error bars represent the numerical variability obtained from five independent simulations for each case.

(see Fig. 3.5), which results in higher strength (i.e., lower plastic strain rates).

3.4 Discussion

3.4.1 Physical model

The framework that we use in this paper to study edge dislocation dynamics in RMEA is that of thermally-activated processes modeled using the residence-time algorithm. Thermally-activated events dictate the global timescale of the system, which evolves under elastic forces using the DD method between events. In other

words, DD relaxation periods are subordinated to take place within time intervals prescribed by the kMC simulator. This generally fits the timescales on which both methods evolve the dislocation, as typical DD time steps in our calculations are on the order of 10^{-10} s, while sampled time steps from kMC are in the 10^{-3} to 10^{-8} s range between 500 and 1700 K. The only exception is 2000 K, where the event times are on the order of 10^{-12} s. There, the dislocation evolution is governed by super-jog jumps, without time for elastic relaxation.

We have used a SNAP potential for the Nb-Mo-Ta-W system [198, 4] as the underlying ‘first-principles’ model to calculate defect energetics. This effectively supersedes models that assume that a multielement alloy can be decomposed into a substrate or matrix that possesses the average properties of its elementary constituents and on which every lattice atom constitutes a solute atom [205, 206]. Defect energies do reveal a ‘high entropy’ effect, i.e., they display statistical averages that deviate beyond numerical error from weighted averages of single-valued energies of the individual alloy elements. Specifically, uniform sampling of the energy distributions results in disproportionate numbers of vacancies with energies below the distribution’s mean. What is more, in certain conditions, vacancies appear spontaneously (i.e., athermally) as a consequence of occasional samplings that lead to zero or even negative formation energy values. This effect confers a very particular nature to the Nb-Mo-Ta-W alloy that cannot be surmised from ‘average’ material properties.

What is true for bulk systems is also true for atomistic environments surrounding edge dislocation cores, i.e., vacancies exist thermally (and even spontaneously) on the dislocation line. These vacancies on dislocation lines are topologically equivalent to super-jogs, consistent with a number of works in the literature [207, 188, 208, 209]. It is clear that these super-jogs act as pinning points for the dislocation line,

increasing the activation stress and strengthening the material [210, 211, 212, 213]. The athermal presence of super-jogs can also be put in the context of the relaxed configurations of the lines. The evidence from numerous MD studies in several RMEA consistently points to a ground state of dislocations characterized by rough line shapes [174, 214, 215, 171]. Such states are likely to be micro-states, i.e., reflective of the length scale over which compositional fluctuations take place, which is on the order of one atomic distance. Indeed, such roughness is not captured experimentally with conventional microscopy [216, 217]. From a topological point of view, this roughness may manifest itself as *wiggles* along the dislocation line on the glide plane (i.e., kinks) or as steps on the extra half-plane (jogs). While in our model the effect of the line roughness on the glide plane is subsumed into the temperature dependence of the critical stresses and dislocation friction coefficients, roughness in the form of (super)jogs in the extra half-plane is captured explicitly. This is reminiscent of the existence of cross-kinks in screw dislocation lines in thermal equilibrium recently seen in medium-entropy bcc alloys [189].

Super-jog segments display two potential modes of motion. One is along the line, requiring *climb* by emission or absorption of vacancies. However, our atomistic calculations show that there is no energy benefit in having a super-jog expand laterally by vacancy emission compared to having two super-jogs in adjacent positions on the line. As such, this mode of motion is no different than allowing for natural (thermal) nucleation of super-jogs along the dislocation line. The second degree of freedom is the one considered in our model, i.e., forward/backward translation of a super-jog by a diffusive process. Such process is strongly influenced by the resolved shear stress, favoring motion in the direction along which it is applied. The migration energies for this mode of motion are conceptually equivalent to vacancy migration energies from

a position on the dislocation line to the next lattice site along the glide direction, i.e., one Burgers vector distance, which is of course the atomic jump distance in the bcc lattice. As we will show in the next section, this motion leads to a softening of the increased activation stresses due to super-jog pinning.

3.4.2 An analytical model of edge dislocation strength based on the present numerical results

Using the various contributions to the dislocation evolution model presented in Sec. 3.2.1, a compact expression for the strength of the material due to edge dislocations can be derived (full derivation provided in 3.7):

$$\tau = \tau_c^{\text{edge}}(T) + \Delta\tau^*(T) + B^{\text{edge}}(T) \left[\frac{\dot{\epsilon}_0}{\rho_d b^2} - 2q_m^{\text{jog}}(T) \right] \quad (3.11)$$

where τ_c^{edge} is the critical stress, Table 3.2, $\Delta\tau^*$ represents the super-jog hardening, eq. (3.15), the term $(B^{\text{edge}}\dot{\epsilon}_0/\rho_d b^2)$ represents the driving force, eq. (3.20), and the term $(2B^{\text{edge}}q_m^{\text{jog}})$, eq. (3.8), represents stress relief due to super-jog motion. The variation of τ with temperature using the parameters given in Table 3.4 is shown in Fig. 3.8, along with each separate contributions from the terms in eq. (3.11). The figure clearly shows that the evolution of the strength is controlled by the interplay between the intrinsic hardening due to super-jog nucleation and softening due to super-jog diffusion. This interplay results in a monotonic decrease of τ with T as shown in the figure. Note that the effect of the applied stress is negligible compared to super-jog-related mechanisms, amounting to no more than 1 MPa at a strain rate of 10^3 s^{-1} . Most importantly, the strength decreases slowly with temperature, bolstered by a higher thermal concentration of super-jogs (leading to more pinning points) as T increases, and modulated by an easier diffusive glide of the super-jogs with

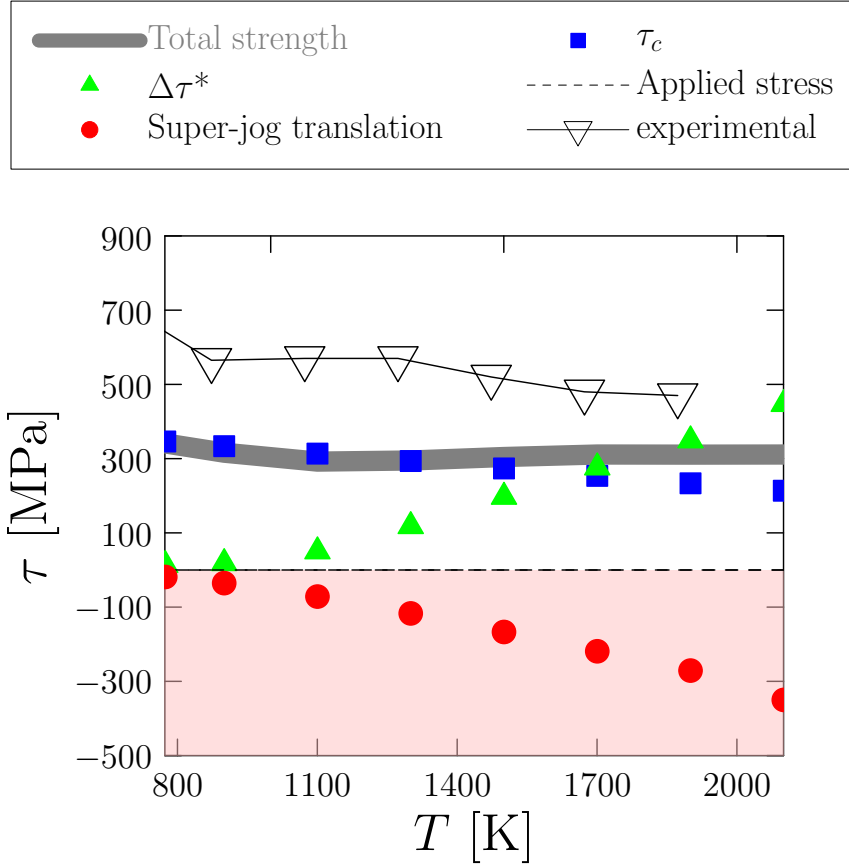


Figure 3.8: Variation of τ with temperature together with different terms contributing to it in eq. (3.11) for a strain rate of $\dot{\epsilon} = 10^{-4} \text{ s}^{-1}$. Experimental data from refs. [6, 7].

temperature. Such behavior bears a significant resemblance with the temperature dependence of the yield strength of a number of different RMEA [6, 218, 219, 196, 220]. As such, we believe that these mechanisms explain –to a large degree– the high temperature strength of these alloys, as quantitatively confirmed by our model and calculations. The obtained response is reminiscent of the high temperature behavior of Ni-based superalloys, where the strength results from a balance between the formation and dissolution of Kear-Wilford locks, both of which are temperature-enhanced [221].

It is also interesting to derive an expression for the extra strengthening of a RMEA relative to a pure bcc metal under the same loading conditions (cf. 3.7):

$$\Delta\tau_{\text{RMEA}}(T) \approx \tau_{\text{RMEA}}(T) - \tau_{\text{bcc}}(T) = \tau_c^{\text{edge}}(T) + \Delta\tau^*(T) - 2B^{\text{edge}}(T)q_m^{\text{jog}}(T) \quad (3.12)$$

This expression gives the terms that contribute to hardening due to the chemical nature of RMEA versus pure or dilute bcc systems. As the equation shows, all terms display a temperature dependence. τ_c^{edge} displays a weak one in the manner typical of thermal softening, while the other two terms display quasi-exponential (Arrhenius) dependencies. Eq. (3.12) shows that the commonly cited mechanism of lattice fluctuation interactions (local solute interactions) is only one of several terms that contribute to the strength. We believe that non-conservative processes that are unique to RMEA play a fundamental role in explaining the temperature dependence of the alloy strength.

3.4.3 Discussion on model predictions

Our model results show that the contribution of edge dislocations to the strength of Nb-Mo-Ta-W stems from the balance between two opposing mechanisms. The first is a strengthening contribution associated with a thermal concentration of super-jogs which increases with temperature. The second is a softening effect brought about the thermal motion of the super-jogs, which also increases with temperature. The combination of these two contrary effects dictates the temperature dependence of the edge dislocation contribution.

In terms of comparison with experimental data, we add the yield strength measurements in equiatomic Nb-Mo-Ta-W alloys in Fig. 3.8 [6, 7]. We see that, while below 800 K there is a gap of over 500 MPa between our model and the experimen-

tal measurements, at higher temperatures the match is almost exact. Evidently, the alloy yield strength measured experimentally includes other sources of strengthening beyond edge dislocations, particularly at low temperatures where contribution from screw dislocations, small intermetallic particles and/or short range order could play a role. While this may explain the observed gap, it is clear that edge dislocations should be counted as a significant source of strength in this and other similar RMEA.

We end with a note on the role played by the dislocation density in the strength of edge dislocations. As mentioned in Sec. 3.3.2, values of ρ_d as low as $5 \times 10^{12} \text{ m}^{-2}$ have been measured for Nb-Mo-Ta-W [200]. However, here we have used more realistic values in the vicinity of 10^{15} m^{-2} to be consistent with most experimental data in bcc RMEA. In eq. (3.11), the term $(B^{\text{edge}}\dot{\epsilon}_0/\rho_d b^2)$ represents the driving force and is the only one with an explicit dislocation density dependence. The stress due to this term ranges between 2.7×10^{-9} and 5.4×10^{-7} MPa for $\rho_d = 10^{15}$ and $5 \times 10^{12} \text{ m}^{-2}$, respectively, when $\dot{\epsilon}_0 = 10^{-3} \text{ s}^{-1}$. This effectively renders the driving force term irrelevant in the global picture of strength, which makes the value of the dislocation density in the range of interest also irrelevant.

3.5 Conclusions

We finish with our main conclusions:

1. We have proposed a new mechanism for edge dislocation dynamics in Nb-Mo-Ta-W alloys. The mechanism provides a qualitative explanation for the elevated intermediate-temperature strength of refractory multi-element alloys, which is governed by non-conservative edge dislocation dynamics.

2. Our mechanism is postulated on the favorable thermal existence –sometimes even spontaneous– of vacancies along edge dislocation lines. These vacancies relax into super-jogs that act as extra pinning points that increase the activation stress. At the same time, these super-jogs are able to diffuse along the glide direction, relieving some of this extra stress. The total strength is a balance between these two processes added on top of the lattice friction due to chemical fluctuations and short-range order.
3. We have developed a numerical model based on a kinetic Monte Carlo module –which captures thermally activated events (super-jog nucleation and translation)– and a discrete dislocation dynamics module –which evolves the line configuration in response to elastic forces– that are coupled to one another via timescale evolution. The global timescale is set by the kMC module on the basis of a Poisson sampling of the thermally activated event rates, while the DD subcycle takes place in between KMC events.
4. All material parameters and alloy energetics have been obtained using a machine-learning SNAP potential. The vacancy formation and migration energies are characterized by distributions with means that deviate from the weighted averages of the elemental constituents of the alloy. Thermal sampling of these distributions results in an equilibrium super-jog concentration that is substantially larger than those predicted by the mean formation energy.
5. An analytical model that captures the essential features of the system yields a strength temperature dependence in excellent qualitative agreement with experimental measurements.

3.6 Computational flow diagram

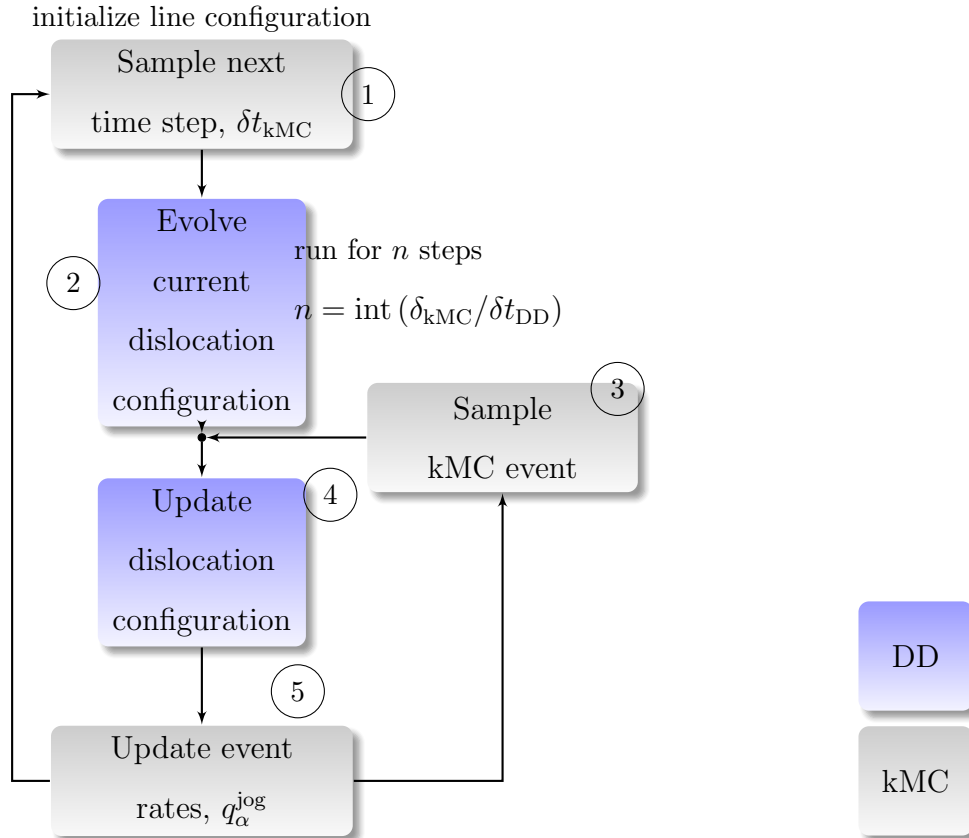


Figure 3.9: Flow diagram of the numerical procedure employed here. Processes pertaining to the kMC module are colored in shaded gray, while those pertaining to the DD module are colored in shaded blue. Each box is numbered according to the sequence of steps.

3.7 Analytical model of edge dislocation strength due to super-jog evolution

For an edge dislocation source with a length ℓ , one can calculate the activation stress in the standard way as:

$$\Delta\tau = \frac{\alpha\mu b}{\ell}$$

which is independent of temperature if we neglect the thermal softening of the elastic constants of the material. When super-jogs appear, the total dislocation length is shortened into segments of average length ℓ^* :

$$\Delta\tau^*(T) = \frac{\alpha\mu b}{\ell^*(T)} \quad (3.13)$$

where $\ell^*(T)$ is the inverse of the super-jog concentration at temperature T :

$$\ell^*(T) = n_0(T)^{-1} = w \exp\left(\frac{\bar{E}_f^\perp}{kT}\right) \quad (3.14)$$

where we have used $n_0^* = \ell/w$ as the pre-factor of $n_0(T)$, which is equal to the total number of independent nucleation sites along the dislocation line. Equation (3.13) then becomes:

$$\Delta\tau^*(T) = \frac{\alpha\mu b}{w} \exp\left(-\frac{\bar{E}_f^\perp}{kT}\right) \quad (3.15)$$

where we are assuming an exponential temperature dependence of $n_0(T)$ defined by the mean energy value of $p(E_f^\perp)$ (Fig. 3.4a). Below, this will be replaced with the actual dependence of n_0 on T obtained in Fig. 3.5. The *excess* stress available for dislocation glide is then obtained by subtracting $\Delta\tau^*(T)$ and $\tau_c^{\text{edge}}(T)$ (Table 3.2) from the resolved shear stress τ :

$$\Delta\tau_{\text{gl}} = \tau - (\Delta\tau^*(T) + \tau_c^{\text{edge}}(T)) \quad (3.16)$$

The glide velocity can then be defined as:

$$v_{\text{gl}} = \frac{b\Delta\tau_{\text{gl}}}{B^{\text{edge}}(T)} \quad (3.17)$$

Concurrently, super-jogs can advance along the glide direction with a velocity given by:

$$v_{\text{sj}} = bq_m^{\text{jog}} = 2b\nu'_0 \exp\left(-\frac{\bar{E}_m^\perp}{kT}\right) \sinh\left(\frac{1.2\Omega_a\tau}{kT}\right) \quad (3.18)$$

where the ‘sinh’ term captures the balance of forward and backward jumps. Here again, we take \bar{E}_m^\perp as representative of the $p(E_m^\perp)$ energy distribution (Fig. 3.4b).

The total velocity of the dislocation line is:

$$v_{\text{tot}} = v_{\text{gl}} + v_{\text{sj}} \quad (3.19)$$

which can be related to a prescribed strain rate $\dot{\epsilon}_0$ using Orowan’s equation:

$$\dot{\epsilon}_0 = b\rho_d v_{\text{tot}} \quad (3.20)$$

where ρ_d is the dislocation density. Combining eqs. (3.17), (3.18), and (3.20), we arrive at:

$$\dot{\epsilon}_0 = b\rho_d \left[\frac{b\Delta\tau_{\text{gl}}}{B^{\text{edge}}(T)} + 2b\nu'_0 \exp\left(-\frac{\bar{E}_m^\perp}{kT}\right) \right] \quad (3.21)$$

Operating and using the various definitions for the different terms in the above equations, we can write a compact expression for the strength of the material due to edge dislocations:

$$\tau = \tau_c^{\text{edge}}(T) + \Delta\tau^*(T) + B^{\text{edge}}(T) \left[\frac{v_{\text{tot}}}{b} - 2q_m^{\text{jog}}(T) \right] \quad (3.22)$$

with:

$$\begin{aligned}
\tau_c^{\text{edge}}(T) &= 423.6 - 0.1T \text{ [MPa]} \\
\Delta\tau^*(T) &= \frac{\alpha\mu b}{w} \exp\left(-\frac{\bar{E}_f^\perp}{kT}\right) \\
v_{\text{tot}} &= \frac{\dot{\epsilon}_0}{\rho_d b} \\
q_m^{\text{jog}}(T) &= \nu'_0 \exp\left(-\frac{\bar{E}_m^\perp}{kT}\right) \sinh\left(\frac{1.2\Omega_a\tau}{kT}\right)
\end{aligned}$$

For convenience, we list all the material constants in Table 3.4. Eq. (3.22) shows that

Table 3.4: Parameters and material constants used to evaluate eq. (3.22).

Parameter	Description	Value	Units	Source
α	hardening coefficient	0.5	–	this work
μ	shear modulus	94	GPa	[4]
a_0	lattice parameter	3.24	Å	this work
b	$a_0\sqrt{3}/2$	2.81	Å	this work
w	$a_0\sqrt{6}/3$	2.64	Å	this work
Ω_a	$a_0^3/2$	1.7×10^{-29}	m ³	this work
B^{edge}	dislocation friction coefficient	2.12×10^{-4}	Pa·s	[3]
\bar{E}_f^\perp	effective super-jog formation energy	0.02~0.13	eV	this work (Fig. 3.5)
ρ_d	dislocation density	$1 \sim 2 \times 10^{15}$	m ⁻²	Sec. 3.3.2
ν'_0	attempt frequency	10^{13}	Hz	this work
\bar{E}_m^\perp	effective super-jog migration energy	0.32	eV	this work (Fig. 3.4b)

the sources of strengthening for edge dislocations are the intrinsic lattice stress, τ_c^{edge} (decreases linearly with temperature), the extra stress due to the existence of super-jogs, $\Delta\tau^*(T)$ (increases exponentially with temperature), and the applied stress, $\dot{\epsilon}_0 B^{\text{edge}}/\rho_d b^2$ (independent of temperature). Conversely, the motion of super-jogs,

represented by q_m^{jog} , reduces the strength of the material (increasing also exponentially with temperature). However, to obtain the true temperature dependence of the strength of the system, we must substitute the standard Arrhenius expression for $n_0(T)$ in $\Delta\tau^*(T)$, eqs. (3.14) and (3.15), with its actual thermal dependence given in Fig. 3.5. Such substitution gives rise to the temperature response shown in Fig. 3.8.

It is also interesting to derive the extra strengthening due to multielement alloy effects. The equivalent of eq. (3.22) for a pure system or dilute alloy would read:

$$\tau_{\text{bcc}} = \tau_c^{\text{edge}}(T) + \alpha\mu b\sqrt{\rho_d} + B^{\text{edge}}(T) \frac{\dot{\epsilon}_0}{b^2\rho_d} \quad (3.23)$$

i.e., $\Delta\tau(T)^* \equiv \Delta\tau(T)$ takes the standard Taylor form ($\alpha\mu b\sqrt{\rho_d}$) and becomes independent of temperature. Assuming, as it is customary, that $\tau_c^{\text{edge}} \approx 0$ in bcc metals, and that $w \ll \rho_d^{-1/2}$, i.e., neglecting the Taylor hardening term, we can subtract eq. (3.23) from (3.22), we arrive at the extra strengthening associated with RMEA effects:

$$\begin{aligned} \Delta\tau_{\text{RMEA}}(T) \approx \tau_{\text{RMEA}}(T) - \tau_{\text{bcc}}(T) &= \tau_c^{\text{edge}}(T) + \frac{\alpha\mu b}{w} \exp\left(-\frac{\bar{E}_f^\perp}{kT}\right) + \\ &- 2B^{\text{edge}}\nu'_0 \exp\left(-\frac{\bar{E}_m^\perp}{kT}\right) \sinh\left(\frac{1.2\Omega_a\tau}{kT}\right) \end{aligned} \quad (3.24)$$

This expression gives the terms that contribute to hardening due to the chemical nature of RMEA versus pure or dilute bcc systems. As the equation shows, only the last term has an explicit dependence on stress. In other words, the difference between RMEA and bcc systems decreases with increasing stress on account of the super-jog diffusion term.

CHAPTER 4

Geometrically Necessary Dislocations signal analysis

4.1 Introduction

We present a numerical methodology to compute the Nye-tensor fingerprints of dislocation loop absorption at grain boundaries (GBs) for comparison with TEM observations of irradiated polycrystals. Our approach links atomistic simulations of self-interstitial atom (SIA) prismatic loops gliding toward and interacting with GBs in body-centered cubic iron with experimentally-extracted geometrically necessary dislocation (GND) maps to facilitate the interpretation of damage processes. The Nye-tensor analysis is strongly mesh-size dependent—corresponding to resolution-dependent TEM observations. The method computes GND fingerprints from discretized dislocation line segments extracted from molecular dynamics simulations of dislocation loops being absorbed at a GB. Specifically, we perform MD simulation of prismatic loops of two diameters and monitor the three stages of the absorption process: loop glide, the partial, and full absorption of the loops at a $[1\ 0\ 0]$ symmetric tilt GB. These methods provide a framework for future investigations of the nature of defect absorption by grain boundaries under irradiation conditions.

4.2 Introduction

Radiation damage in structural materials leads to microstructural evolution[76, 77, 78, 79, 80, 81] and mechanical property changes[82, 83, 84, 85, 86] as a consequence of complex interactions between radiation-induced defects (vacancies, self-interstitials, point defect clusters, transmutation elements, ...) and intrinsic material defects such as dislocations and grain boundaries (GBs). GBs are particularly powerful defect sinks, absorbing defects from within grain interiors and accommodating these within the GB structure [87, 88, 89, 90, 91, 92]. Carefully tailored GB microstructures have the potential to confer high irradiation resistance to structural materials [89, 93, 94, 95].

Experimentally, a telltale signature of defect adsorption is the observation of *denuded* (i.e., defect-free) zones adjacent to the GBs [88, 89, 96]. A denuded zone is a region of finite spatial extent over which defect concentrations decay from their bulk values to near zero. The denuded zone size may be used as a measure of GB sink efficiency; albeit an indirect one. Denuded zone size has been shown to vary based on a variety of factors, including but not limited to specific GB type (5 macroscopic degrees of freedom), material, type of defect, defect transport coefficients and generation rates within the bulk, point defect interactions with each other, type and extent of irradiation, necessitating a more robust method for the quantification of defect absorption by GBs [97, 96, 98, 99, 88, 89]. A more direct marker of defect absorption by GBs would allow a more robust characterization of sink efficiency, as well as characterization of absorption response and understanding of the denuded zone phenomenon. Because modifications of GB macrostates necessarily result in lattice curvature changes, a popular technique to characterize these changes is to

infer the density of geometrically-necessary dislocations (GND) from lattice curvature measurements; this is commonly represented as a spatial map of the Nye tensor [93, 100, 101, 2, 102]. Strictly speaking, GNDs are associated with slip gradients in lattice plastic rotations in the lattice; these are seen as net nonzero Burgers vector densities [102]. Changes in measured Burgers vector distributions and the resultant Nye tensor distribution provide a direct means of characterizing GB point defect absorption. In this paper, we explore GND measurements as a direct method of characterising defect absorption by GBs by linking atomistic descriptions of defect absorption with experimental observations of changing Nye tensor measurements.

Primary radiation damage is characterized by the introduction of equal numbers of vacancies and self-interstitial atoms (SIA) [103, 104, 105]. In sufficiently dense displacement cascades, vacancy clusters assemble into small compact voids or stacking fault tetrahedra, depending on whether irradiation takes place in high (e.g., body centered cubic (bcc) crystals) or low (face centered cubic, fcc) stacking fault energy metals, respectively [106, 107, 108]. SIA clusters, on the other hand, tend to assemble into prismatic dislocation loop structures which are highly mobile, diffusing rapidly in the direction parallel to their Burgers vector.¹ In bcc metals, these glissile loops have a Burgers vector of $(a_0/2)\langle 111 \rangle$, where a_0 is the lattice parameter. Therefore, the only feature in the bulk capable of contributing a GND signal to the Nye tensor analysis are prismatic loops. Here, we use molecular dynamics (MD) simulations of these loops bcc iron to illustrate these ideas.

Interactions of dislocations and grain boundaries have been observed both experimentally in TEM [109, 110, 111, 112] and in simulation [113, 114, 115, 116], but

¹There have been sporadic observations of vacancy platelet collapse into dislocation loops as well, both in bcc and fcc metals.

direct effects of these interactions in large volumes are not yet fully understood and require a method of direct observation at larger scales. A number of indirect measures of defect absorption effects and absorption correlations have been presented, including but not limited to characterizations of the denuded zone [88, 89, 96], effects of grain boundary structure on sink efficiency [97], and effect of grain boundary character on sink efficiency [89]. In this paper, we present a direct method for detecting dislocation loop absorption by GBs, which provides a framework to further quantify the absorption response.

The procedure to extract GND densities from molecular dynamics simulations, i.e., linking atomic-level information with experimental measurements of Nye tensor signals involves the integration of different approaches: (1) MD simulations of SIA loop structure and kinetics at/near the GB; (2) conversion of spatial coordinate information (from MD) into a dislocation line representation; (3) spatial discretization of dislocation lines into volumetric cells; and (4) calculation of GND densities in each discrete cell. Of particular interest are the differences in the GND footprint of bulk loops, partially absorbed loops into the GB, and fully absorbed loops; all scenarios in irradiated microstructures. Our correlation between simulated prismatic loop absorption and experimental observables provides a method of detection and fingerprinting of absorption phenomena at GBs.

4.3 Experimental Observations

Nanocrystalline (NC) Fe specimens for transmission electron microscopy (TEM) analysis were created from 100-150 nm thick magnetron sputtered iron thin-films on $\langle 100 \rangle$ NaCl substrates. Final cross sections were prepared by focused ion beam

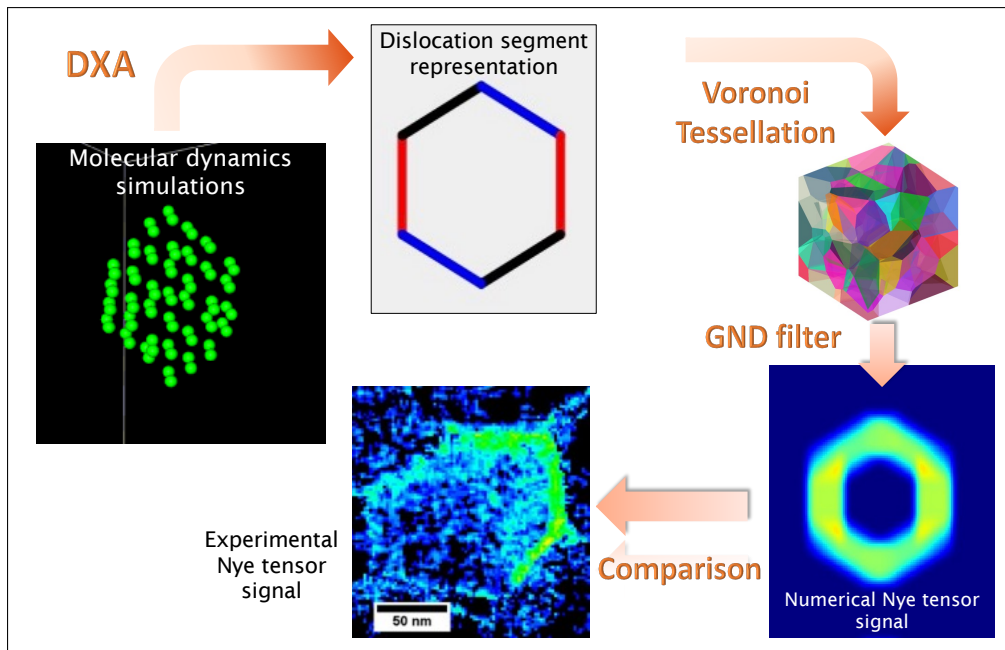


Figure 4.1: Schematic illustration of the computational workflow of the methods developed in this paper.

(FIB) milling. For irradiation, thin planar iron films were mounted on 200 mesh TEM grids. The as-deposited films were annealed in-situ using a Gatan 628 TEM heating stage at 675°C in preparation for irradiation. The annealing conditions were chosen to obtain stable grain structures of appropriate grain sizes (comparable to bulk samples).

The large grain, NC Fe samples were irradiated using a Hitachi H-9000NAR IVEM-Tandem at Argonne National Laboratory using 1 MeV Kr²⁺ ions accelerated using a 650-kV ion implanter at 300°C to damage levels of 5 dpa. The substrate temperature during deposition was maintained at about 370°C.[117, 118, 119] Post-irradiation orientation data was acquired using NanoMEGAS ASTAR(TM) precession electron diffraction and ASTAR(TM) ACOM-TEM systems on a JEOL 2100 Lab6 TEM operated at 200 kV with a spot size of 15 nm, step size of 5 nm, and precession angle of 0.60°.

Orientation data was analyzed using the EDAX TSL OIM Analysis software package. The deformation associated with lattice curvature were deduced using local orientation spread and kernel averaged misorientation [120]. Each point in the image was treated as a kernel with a specified number of nearest neighbors and the misorientation between each point is averaged for each given kernel. Contortion tensors for each center of a kernel (at its nearest neighbor points) were used to estimate the GND density using a least-squares fitting procedure. The least-squares contortion values were used to calculate a single Nye tensor, describing the state of dislocation surrounding each point [2]. The lower bound GND density is calculated using a dislocation density tensor normalized by the Burgers vector [121, 122], assuming a dislocation Burgers vector of $(a_0/2)\langle 111 \rangle$ for bcc Fe [2]. Estimated lower-bound GND densities were then generated in Origin for direct comparison to the

TEM micrograph region of interest (ROI) [2].

4.3.1 Results

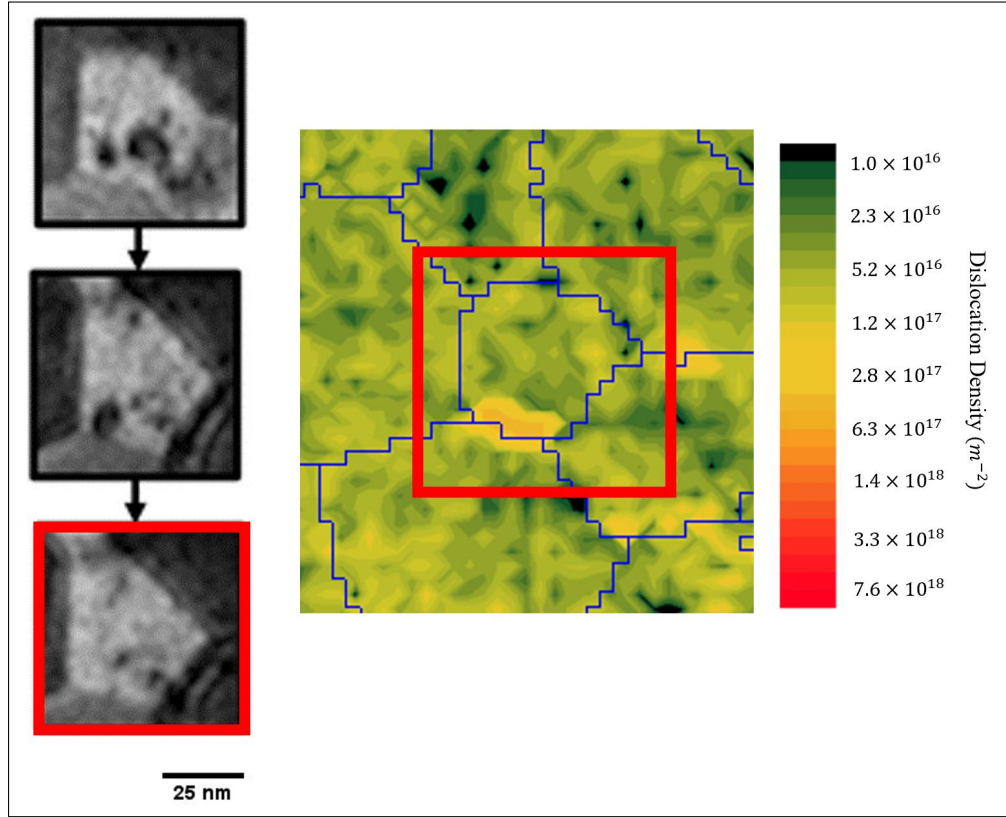


Figure 4.2: Bright field micrographs of a grain with $(a_0/2)\langle 111 \rangle$ Burgers vector dislocation loop being absorbed onto a $\langle 110 \rangle$ GB plane. Nye dislocation tensor map generated from PED ACOM orientation data highlighted increased signal at the $25^\circ [1 -3 -6]$ GB [2].

The left-hand side of Fig. 4.2 shows bright field micrographs of a grain containing an $(a_0/2)\langle 111 \rangle$ prismatic dislocation loop being absorbed into a $\langle 110 \rangle$, $25^\circ [1 -3 -6]$ grain boundary. Contortion measurements were conducted as described above to produce a Nye tensor map and estimated GND density at discrete points [2]; the

results are shown in the right image of Fig. 4.2 after the absorption of the dislocation loop. The observed processes suggest a number of questions that are challenging to address exclusively experimentally. However, they provide an excellent platform from which to start looking at these complex processes from a computational point of view. We perform atomistic and mesoscale simulations of the phenomenon captured in the experiments, i.e., full prismatic loop absorption. Our goal is the development of a computational methodology needed to interpret Nye tensor signals associated with dislocation absorption for future experiments.

4.4 Theoretical Background

Geometrically necessary dislocations (GNDs) are dislocations that accommodate lattice curvature due to nonuniform plastic deformation. These dislocation have net nonzero Burgers vector and do not contribute to plastic strain per se (although they can contribute to strain hardening [123, 124]). As a consequence, GNDs are a measure of plastic distortion and can thus provide useful information on lattice rotation associated with slip, grain boundary motion, or plastic strain gradients. GND may be characterized by the *Nye* tensor (also referred to as the ‘dislocation density’ tensor, or the ‘GND’ tensor), which can be obtained as a line integral over all dislocations within a volumetric element (of volume V). If \mathbf{b} is the Burgers vector of a dislocation with local unit tangent line direction \mathbf{t} , the Nye tensor, $\boldsymbol{\alpha}$ is defined as [125]

$$\boldsymbol{\alpha} = V^{-1} \int_L (\mathbf{b} \otimes \mathbf{t}) dl, \quad (4.1)$$

where the differential dl runs along the entire dislocation line length $L \in V$. When L is discretized into N piecewise segments of length Δl inside the volume element,

as is common in dislocation dynamics simulations, Eq. (4.1) can be expressed as a discrete sum where each segment i is represented by \mathbf{b}_i and a segment length vector $\mathbf{l}_i = \Delta l \mathbf{t}_i$

$$\boldsymbol{\alpha} = V^{-1} \sum_i^N (\mathbf{b}_i \otimes \mathbf{l}_i). \quad (4.2)$$

As such, a closed loop (all segments with identical \mathbf{b}_i) fully enclosed in the volume V necessarily leads to zero GND signal due to the mutual cancellation of contribution from segments with positive and negative \mathbf{t}_i projections. When representing the GND tensor graphically, it is customary to plot the L1 norm of $\boldsymbol{\alpha}$: $|\boldsymbol{\alpha}|_1 = \max_n \sum_m \|\alpha_{nm}\|$. The connection between Eq. (4.2) and this norm and the scalar dislocation density ρ used in plasticity is given in Appendix 4.9.²

The GND tensor can also be obtained from lattice curvature measurements as:

$$\boldsymbol{\alpha} = \boldsymbol{\kappa}^T - \text{Tr}(\boldsymbol{\kappa})\mathbf{I} \quad (4.3)$$

where $\boldsymbol{\kappa}$ is the lattice curvature tensor and \mathbf{I} is the identity matrix. $\boldsymbol{\kappa}$ is a measure of the spatial gradient of the lattice orientation, i.e.,

$$\kappa_{ij} = \partial \omega_i^e / \partial x_j \approx \delta \omega_i^e / \delta x_j.$$

Here, $\boldsymbol{\omega}^e$ is the rotation axis (i.e., part of the axis-angle pair of the crystal with respect to a fixed reference). $\delta \omega_i^e$ is the misorientation between each point and its neighbors [2, 126] separated by distance δx_j . Equation (4.3) is known as Nye's formula and links the dislocation density tensor and the lattice curvature in the context of small elastic strains and rotations. Full derivations of these equations are provided in Appendix 4.9. In essence, the method presented here provides a physical connection

²Note that in both Eqs. (4.2) and (4.3), the GND density has units of inverse length, instead of the standard inverse length squared of the scalar dislocation density.

between the representations of the dislocation density tensor encoded in Eqs. (4.2) and (4.3).

Disconnections are line defects that are contained to lie along interfaces/GBs that have both Burgers vector and step character [127]. While Burgers vectors of common lattice dislocations are determined by the slip planes of the crystal structure and material, disconnection Burgers vectors are determined by displacement-shift-complete (DSC) vectors of the bicrystal. Since the DSC vectors are determined by the relative orientations of the crystals involved, the possible disconnection Burgers vectors of different GBs will differ. Disconnection Burgers vectors and step heights are pairs in the sense that each Burgers vector has a discrete set of possible step heights and vice versa. A step accounts for the shift in the coincidence site lattice (CSL) produced by the DSC vector translation. Lattice dislocations can be expressed as DSC vector sums, and these lattice Burgers vectors when intact create a special case of disconnection where the step height is zero [127].

4.5 Computational Methods

4.5.1 Atomistic

Dislocation loops were created in a simulation cell with relaxed GBs which were subsequently absorbed by the GBs during molecular dynamics simulations. A (012)[100] symmetric tilt grain boundary was constructed in bcc Fe and energy-minimized in LAMMPS [55] using an interatomic potential for Fe selected for its ability to reproduce defect formation energies, dislocation kink formation energies, and general dislocation dynamics parameters [128]. Simulation cell dimensions were determined based

consistent with coincident-size lattice (CSL) requirements for a periodic boundary conditions. The simulation cell size was fixed such that the dimensions of the grains were at least three times the diameter of the dislocation loop, in order to avoid overlap of displacement fields between the loop and its periodic images. Vacancy and interstitial dislocation loops of radii 20 Å and 80 Å were constructed by either removing or inserting circular discs of three $\{111\}$ planes of atoms, then performing an energy minimization of the immediate surrounding region to produce dislocation loops with $(a_0/2)\langle 111 \rangle$ Burgers vectors. Loops were initially located 20 Å from the grain boundary in order to facilitate absorption. The dislocation loop/GB simulations were performed using molecular dynamics at 1300 K for 1 ns beyond the time required for complete dislocation absorption by the GBs using with a timestep of 1 fs.

The dislocation structure was observed using `OVITO` and its dislocation line representation obtained using Dislocation Extraction Algorithm (DXA) [5, 129] (based upon a Burgers circuit construction). Sequences of atomistic frames with high time resolution were inspected in `OVITO` to track absorption and identify disconnections within the GB and/or metastable states present. Disconnections were located by detecting shifts in the grain boundary plane, after which their Burgers circuits and corresponding steps were determined.

4.5.2 Discrete GND analysis

The final stage of the modeling sequence involves the calculation of spatially-resolved GND signals from DXA-filtered loop configurations. This effectively links atomic-level information (where fundamental loop properties are defined) with experimental

measurements of Nye tensor signals based on lattice curvature gradients (see Section 4.3). To mimic the spatial discretization in precession electron diffraction tests, we use a three-dimensional tessellation of the MD supercells. We study GND footprints using both regular structured meshes (uniform cell size and shape) as well as general Voronoi tessellations with fixed average cell size. Subsequently, we perform cell edge detection procedure by overlaying DXA-filtered three-dimensional supercells on the discretized meshed volume, following by Nye tensor determination according to the methods described in Section 4.4. The GND signal is then obtained as the L1-norm of the Nye tensor, and final intensities are represented as smeared versions of discrete signals using a normalized Gaussian spread function.

The Voronoi tessellations were performed using the Polytope Bounded Voronoi Diagram `MATLAB` library [130]. The main controlling parameter for the cell volume is the concentration of individual cell generators, i.e., the number of spatially random points introduced as centroids of each Voronoi cell.

4.6 Results

4.6.1 Molecular dynamics simulations

The process of GB absorption of the dislocation loop consists of three stages: (i) period preceding dislocation contact with the GB, (ii) partial absorption of the dislocation loop, and (iii) loop fully absorbed into the GB. Figs. 4.3a and 4.3c show atomistic images obtained using common neighbor analysis of MD of stages (i) and (ii).

DXA analysis of the atomic configuration data is used to transform the three-

dimensional atomic configurations into a sharp dislocation line representation. DXA results for stages (i) and (ii) are shown in Fig. 4.3, while the fully absorbed state is given in Fig. 4.4. Figs. 4.3b and 4.3d show the DXA representations.

The colors in Figs. 4.4a and 4.4b represent the following: green segments indicate a dislocation line with Burgers vector of $(a_0/2)[111]$, magenta represents $[100]$ Burgers vectors, the array of GB dislocations are shown in dark blue, and red lines represent dislocation segments with Burgers vectors which DXA was unable to identify.

After loop absorption, the MD simulations show the decomposition of the original Burgers vector into a pair of disconnection loops (similar for both the 20-Å and 80-Å radius loops). The decomposition of the original dislocation loop into disconnections consistent with the following Burgers vector reaction:

$$\frac{a_0}{2}[111] \rightarrow \frac{a_0}{10}[531] + \frac{a_0}{5}[012]. \quad (4.4)$$

These disconnection Burgers vectors are consistent with an analysis of the displacement-shift-complete (DSC) vectors of the bicrystal. The disconnections remained intact after annealing for 1 ns at the simulation temperature, indicating a stable absorption reaction as suggested by the simple application of Frank’s rule (i.e., no further disconnection decomposition into other bicrystallography-allowed disconnections occur).

Note that in the preceding MD results, the dislocation loop absorption occurred at a grain boundary that had not previously absorbed point defects, dislocations, or dislocation loops (this was done to clarify dislocation loop/GB interactions). In irradiation experiments, a GB will likely be less perfect; having previous absorbed other defects and/or exhibit a distribution of microstates [95, 131]. Such structural inhomogeneities/defects within the GB may affect subsequent dislocation loop ab-

sorption. During irradiation experiments, the grain boundary structure may achieve a steady-state distribution of such inhomogeneities/defects. On the other hand, periodic denuded zone collapse may imply that a true steady-state GB structure is never achieved. While this is beyond the scope of the present paper, we will return to some of these issues in Section 4.7. In any case, the single loop absorption case is used to showcase that a change in GND signal results from the presence of a Burgers vector in the grain boundary. The single loop absorbed by a perfect grain boundary allows better characterization of the incoming and resulting Burgers vectors, which are then used to generate the GND signal.

4.6.2 GND density calculations

Nye tensor calculations are highly sensitive to the size of the mesh employed in the spatial discretization (as discussed above). The natural upper bound of such a discretization is a mesh with a single element (i.e., no discretization of the supercell volume), while the number of elements divergent as the mesh size tends to zero. We now analyze the GND signal of the 20 and 80-Å loops during the three stages of loop-GB interactions, i.e., pre-absorption, partial absorption, and full absorption.

Equation (4.2) implies that a closed dislocation loop generates no net GND signal. In a numerical sense, a discretized closed loop may not strictly cancel due to limitations on numerical precision; this nonzero value constitutes the ‘numerical zero’ of the structure. As such, our first calculation involves a single volumetric element consisting of the entire MD simulation cell; this serves as the *floor* value of the GND signal. Our calculations based on the MD loop data yield an average GND density of $1.15 \times 10^{10} \text{ m}^{-2}$; this may be considered the zero GND signal for numerical pur-

poses. Regions with GND signals below this threshold are shaded gray in subsequent figures.

We obtain the average signal contributed by loops as a function of the mesh size used in the tessellation of the three-dimensional space. Fig. 4.6a shows an image of the 80-Å prismatic loop highlighting only the cells that contain dislocation loop segments for a particular Voronoi representation of the MD supercell with an average mesh size of 8.0 nm. A heat map of the GND intensity of the loop is given in Fig. 4.6b.

Repeating this process as a function of tessellation cell size leads to the results shown in Fig. 4.7a and 4.7b for the 80 and 20-Å loops, respectively. The average cell size is defined as $\bar{d} = \sum_i v_i^{1/3}/N$, where N is the total number of cells and v_i , $i = 1, \dots, N$, is the volume of each cell. The error bars shown in the figure reflect the variability in tessellation morphology for a constant average mesh size. The smallest mesh size considered corresponds to the estimated resolution limit of ≈ 10 nm from our experimental measurements, as discussed in Section 4.3.1. For internal verification, we compare the analysis of loops using regular hexahedral regular meshes (translucent lines in Figs. 4.7a and 4.7b) in addition to the Voronoi tessellation; very good agreement between both approaches is obtained.

Unlike for the full prismatic loop, the partially absorbed loop does contribute a nonzero GND signal (the volume contains the entire partial loop). For this case, the GND density converges to a finite nonzero value above a threshold mesh size, as shown in Fig. 4.7. Fig. 4.8 shows the highlighted Voronoi cells containing net dislocation content colored by the value of its GND density for both cases. The case for the fully absorbed loop is more difficult to analyze; it is not a full bulk crystal dislocation loop even though it represents a closed linear structure in the GB plane.

The present results indicate that the mean GND density for the full loop (before absorption) decreases towards zero as the mesh size increases, while the partially and fully absorbed cases converge to a nonzero GND value. These results correlate the GND signal to the loop radius (defect size) and the mesh size (volumetric spatial resolution) and, as such, can be used to interpret the experimental observations. In particular, these correlations are quantitative when the experimental resolution limit is known. TEM analysis can be correlated to simulation by utilizing comparable mesh sizes (10 - 70 nm) and PED-ACOM step sizes (5 nm) to effectively replicate the resolution at which experimental data was captured. Our results indicate that the experimental spatial resolution of 30 nm (at which the crossover in GND signal between the full loop and the partially absorbed loop takes place) or less is needed to capture the closed nature of the full 80-Å loop, and of 17 nm or less for the 20-Å loop. The experimental system reports nominally higher GND intensity, which could be due to a number of factors: larger loop size than simulation, thin film sample curvature and texture that contribute to an inherently higher GND density (opposed to a perfect bicrystal in the simulated case), smaller step size that could correspond to an increase in fraction of dislocation observed [2]. A difference in GND intensity is also recognizable in Fig. 4.7 and Fig. 4.8, which show calculations of an intensity based on the entire simulation volume, about 2×10^8 Å, and based on the discretization volume, between 5000 and 3×10^7 Å for the regular mesh cases, respectively. While the model and experiment may not exhibit the same fingerprint for loop absorption, this work presents the first reported case of a fingerprint for GB-loop interaction with a simulated proof that structural changes in a GB after loop absorption produce a GND signal change. Based on our analysis, the spatial resolution under which lattice orientation measurements are provided has a noticeable impact on the final result of

the GND tensor.

As is common in computational methods that depend on spatial resolution, the CPU cost of the approach presented here displays a strong mesh dependence. The computational efficiency of these calculations is discussed in Appendix [4.10](#).

4.7 General Discussion

The main goal of the present paper is to link atomistic representations of irradiation defects with experimental measurements of GND densities based on lattice curvature. We developed software to determine scalar projections of the Nye tensor for prismatic loops as a function of the scale of the spatial discretization. The input to the model is a line representation of dislocation structures filtered from atomic configurations. The output is the scalar norm of the Nye (GND) tensor, which may be directly compared with experiments. In this way, the atomistic scale, at which irradiation defects are unequivocally defined, can be connected to experimental-level observations, from which radiation damage features may be inferred. While the grain boundary studied here was perfect and only absorbed a single dislocation loop, these results affirm the effect of a change in Burgers vector on the GND signal produced. The idea is then to establish a rigorous link between atomic models and TEM-based observations, and to enable further analysis of defect-GB interactions than would be possible through direct TEM characterization; for example, in identifying defect absorption locations and effects in GBs with existing structural defects, or in analysis over length scales that do not lend themselves to direct structural analysis of the GB.

Thus, our approach address several outstanding questions on the interpretation of

experimental measurements. First, are the ‘line’ and the ‘curvature’ representations of the GND tensor interchangeable? While addressing this is beyond the scope of this paper, our methodology is a first step in the direction of clarifying this point. Second, does the GND fingerprint of absorbed loops provide information about intrinsic GB states? Thus far, we can conclude that –perhaps as one might expect– that is not the case. However, our calculations reveal some interesting features of these structures: e.g., the apparent ‘dual’ nature of these absorbed loops, which, on one hand, yield a net nonzero GND fingerprint, while on the other, they are fully closed in the GB plane. We understand that this is a direct consequence of how the atomistic→line conversion used in this work (DXA method) interprets loops fully absorbed by the GB. As such, additional research is required to validate and catalogue GND fingerprints and to establish whether they have an interpretable experimental equivalent signal.

The experimental results shown here prompt a number of additional questions that remain unanswered at this point in the development of our computational tools. For example, how is a finite concentration of semi-absorbed loops with some degree of overlap manifested in terms of a GND signal? How do potential changes in the microstates of the GBs due to sustained loop absorption affect GND density fingerprints? How can the formation and disappearance of dislocation loop denuded zones near a GB at high dose be observed by Nye tensor characterizations. These questions are part of a longer term research effort to quantitatively interpret experimental TEM images to shed light on the interactions between radiation damage and grain boundary sink behavior.

4.8 Conclusions

The major elements of this research report may be summarized as follows:

1. We developed a numerical approach to aid the interpretation of experimental measurements of changes in GND density observed under irradiation conditions.
2. Our approach connects atomic-scale information and experimental measurement by linking MD simulations of prismatic loop structures with spatial representations of the scalar norm of the GND tensor.
3. Analysis of 20 and 80 Å loops indicates a strong dependence of the GND signal on the discretization mesh size/experimental resolution.
4. A change in the GND signal does not, on its own, provide a unique description of GB phenomena associated with dislocation loop absorption, but does confirm the change of Burgers vector(s) on the GB associated with defect absorption from the abutting grain lattices.

4.9 Kinematic and physical definitions of the Nye tensor

4.9.1 Derivation of the dislocation density tensor

Nye's theory relating lattice curvature to dislocation density has been discussed, at length, in the literature [132, 133, 134, 135]. The total deformation gradient \mathbf{F} is a compatible field which may be written in terms of the displacement vector field

$\mathbf{u} = \mathbf{x} - \mathbf{X}$ as:

$$\mathbf{F} = \nabla \mathbf{x} = \nabla (\mathbf{X} + \mathbf{u}) = \mathbf{I} + \nabla \mathbf{u} = \mathbf{I} + \mathbf{E}, \quad (4.5)$$

where $\mathbf{E} = \nabla \mathbf{u}$ is the strain tensor³ The compatibility of \mathbf{F} implies that $\text{Curl } \mathbf{F} = 0$. However, under the multiplicative decomposition generally adopted in finite deformation theory, $\mathbf{F} = \mathbf{F}^e \mathbf{F}^p$, neither the elastic nor the plastic deformation gradients, \mathbf{F}^e and \mathbf{F}^p need be compatible. Multiplicative decomposition takes the system from initial to final configurations by way of an arbitrary intermediate configuration (represented by the coordinate vector $\boldsymbol{\xi}$) that, in crystal plasticity, has the meaning of pure plastic slip:

$$\mathbf{F} = \left(\frac{d\mathbf{x}}{d\boldsymbol{\xi}} \right) \left(\frac{d\boldsymbol{\xi}}{d\mathbf{X}} \right), \quad (4.6)$$

where $d\boldsymbol{\xi} = \mathbf{F}^p d\mathbf{X}$ and $d\mathbf{x} = \mathbf{F}^e d\boldsymbol{\xi}$.

The potential incompatibility of the plastic deformation leads to a closure failure of a suitable Burgers circuit C, defined as the change in length of a path on the surface enclosed by the circuit S associated with generation of dislocations in a given volume V (see Fig. 4.9). In terms of the deformed configuration \mathbf{x} , this closure failure is

$$\mathbf{b} = \oint_C d\boldsymbol{\xi} = \oint_C \mathbf{F}^{e-1} d\mathbf{x}, \quad (4.7)$$

where we have used

$$d\boldsymbol{\xi} = \mathbf{F}^p d\mathbf{X} = (\mathbf{F}^{e-1} \mathbf{F}) d\mathbf{X} = \mathbf{F}^{e-1} d\mathbf{x} / d\mathbf{X} d\mathbf{X} = \mathbf{F}^{e-1} d\mathbf{x}.$$

³Following standard notation, differential operators may be written in terms of the initial coordinates \mathbf{X} or with respect to the current coordinates \mathbf{x} of the material points. In the former case, the notation ∇ , Grad, Div, and Curl are used, while in the latter, $\nabla_{\mathbf{x}}$, grad, div, and curl are used.

Application of Stokes theorem converts Eq. (4.7) into a surface integral:

$$\mathbf{b} = \oint_{\mathbf{C}} \mathbf{F}^{e-1} d\mathbf{x} = - \int_{\mathbf{S}} (\text{curl } \mathbf{F}^{e-1}) \cdot \mathbf{n} ds = \int_{\mathbf{S}} \boldsymbol{\alpha} \cdot \mathbf{n} ds,$$

where \mathbf{n} is a unit vector normal to S. This expression contains the definition of the dislocation density tensor:

$$\boldsymbol{\alpha} = -\text{curl } \mathbf{F}^{e-1} \quad (4.8)$$

Fig. 4.9 shows a schematic illustration with dislocation lines crossing surface S bounded by closed circuit C. The Burgers vector can also be computed by means of a closed circuit C_0 in the reference configuration:

$$\begin{aligned} \mathbf{b} &= \oint_{\mathbf{C}} \mathbf{F}^{e-1} d\mathbf{x} = \oint_{\mathbf{C}_0} \mathbf{F}^{e-1} \mathbf{F} d\mathbf{X} = \oint_{\mathbf{C}_0} \mathbf{F}^p d\mathbf{X} \\ &= - \int_{\mathbf{S}_0} (\text{Curl } \mathbf{F}^p) \cdot d\mathbf{S}. \end{aligned} \quad (4.9)$$

Using Nanson's formula $d\mathbf{s} = J\mathbf{F}^{-T} \cdot d\mathbf{S}$ (where $J = \det(\mathbf{F})$ is the *Jacobian*), one can express the dislocation density tensor with respect to the reference configuration as

$$\boldsymbol{\alpha} = -J^{-1} (\text{Curl } \mathbf{F}^p) \cdot \mathbf{F}^T. \quad (4.10)$$

For a discrete representation of dislocation segments, the dislocation density tensor in volume V takes the form given in Eq. (4.2). This may be generalized, in the language of crystal plasticity, as the (ensemble) average of the contributions from all slip systems β in the volume to the closure failure in circuit C:

$$\boldsymbol{\alpha} = V^{-1} \sum_{\beta} \langle \mathbf{b}^{\beta} \otimes \mathbf{l}^{\beta} \rangle = \sum_{\beta} \langle \mathbf{b}^{\beta} \otimes \boldsymbol{\rho}^{\beta} \rangle, \quad (4.11)$$

where $\boldsymbol{\rho} = V^{-1}\boldsymbol{l}$ is the line density crossing surface S. Note $\boldsymbol{\alpha}$ has units of inverse length rather than length squared, as does traditional dislocation density in plasticity, ρ .

The connection between the dislocation density tensor and ρ (the scalar quantity that is invariant with respect to the frame of reference) may be understood from the autocorrelation function of the Nye tensor:

$$\langle \boldsymbol{\alpha}(\boldsymbol{x}) \cdot \boldsymbol{\alpha}(\boldsymbol{x}') \rangle = \langle \boldsymbol{b}(\boldsymbol{x}) \otimes \boldsymbol{\rho}(\boldsymbol{x}) \otimes \boldsymbol{b}(\boldsymbol{x}') \otimes \boldsymbol{\rho}(\boldsymbol{x}') \rangle = \boldsymbol{\Lambda}(\boldsymbol{x}, \boldsymbol{x}')$$

which is a fourth order tensor ($\Lambda_{ijkl}(\boldsymbol{x}, \boldsymbol{x}) = \chi_{ij}(\boldsymbol{x})$). $\chi(\boldsymbol{x}) = 1$ when there is a dislocation at \boldsymbol{x} and is 0 otherwise. The integral of this quantity over the volume V yields the invariant quantity:

$$\frac{1}{V} \int_V \boldsymbol{\Lambda}(\boldsymbol{x}, \boldsymbol{x}) dv = \frac{1}{V} \int_V \chi(\boldsymbol{x}) dv = \frac{L}{V} = \rho,$$

where L is the total line length enclosed in volume V .

4.9.2 Dislocation density tensor: small deformation limit

In the small deformation limit, we adopt an additive decomposition of the strain tensor, \boldsymbol{E} , into elastic and plastic parts:

$$\boldsymbol{E} = \boldsymbol{E}^e + \boldsymbol{E}^p,$$

which in turn may be decomposed into symmetric $\boldsymbol{\varepsilon}$ and anti-symmetric $\boldsymbol{\omega}$ (rotation) parts:

$$\boldsymbol{E}^e = \boldsymbol{\varepsilon}^e + \boldsymbol{\omega}^e$$

$$\boldsymbol{E}^p = \boldsymbol{\varepsilon}^p + \boldsymbol{\omega}^p.$$

By definition, $\mathbf{F} = \mathbf{I} + \mathbf{E}$, such that:

$$\mathbf{F} = \mathbf{I} + \mathbf{E} = \mathbf{I} + \boldsymbol{\varepsilon}^p + \boldsymbol{\omega}^p + \boldsymbol{\varepsilon}^e + \boldsymbol{\omega}^e$$

Assuming that $\boldsymbol{\varepsilon}^e$, $\boldsymbol{\omega}^e$, $\boldsymbol{\varepsilon}^p$, and $\boldsymbol{\omega}^p$ are all small, and neglecting second order terms, we may make the approximation:

$$\mathbf{I} + \boldsymbol{\varepsilon}^p + \boldsymbol{\omega}^p + \boldsymbol{\varepsilon}^e + \boldsymbol{\omega}^e \approx (\mathbf{I} + \boldsymbol{\varepsilon}^p + \boldsymbol{\omega}^p)(\mathbf{I} + \boldsymbol{\varepsilon}^e + \boldsymbol{\omega}^e).$$

By equivalence with the multiplicative decomposition of the deformation gradient, $\mathbf{F} = \mathbf{F}^e \mathbf{F}^p$, the above expression implies that

$$\mathbf{F}^e \approx \mathbf{I} + \mathbf{E}^e$$

$$\mathbf{F}^p \approx \mathbf{I} + \mathbf{E}^p$$

and thus, from Eq. (4.10),

$$\boldsymbol{\alpha} \approx -\text{Curl } \mathbf{E}^p = \text{Curl } \mathbf{E}^e \quad (4.12)$$

since $\text{Curl } \mathbf{E} = 0$ due to the compatibility of the deformation gradient.

4.9.3 Dislocation density and lattice curvature

Experimental techniques like EBSD provide the lattice orientation field and, consequently, the lattice rotation \mathbf{R}_e during deformation. Invoking the polar decomposition of Eq. (4.8) we may write the dislocation density tensor as

$$\boldsymbol{\alpha} = -\text{curl } \mathbf{F}_e^{-1} = -\text{curl } (\mathbf{U}_e^{-1} \mathbf{R}_e^T).$$

In the small elastic strain limit

$$\boldsymbol{\alpha} \approx -\text{curl } \mathbf{R}_e^T,$$

If, in addition, elastic rotations are small, we have

$$\boldsymbol{\alpha} \approx -\text{curl}(\mathbf{I} - \boldsymbol{\omega}^e) = \text{curl } \boldsymbol{\omega}^e, \quad (4.13)$$

where

$$\boldsymbol{\omega}^e = \begin{pmatrix} 0 & -\overset{\times}{\omega}_3^e & \overset{\times}{\omega}_2^e \\ \overset{\times}{\omega}_3^e & 0 & -\overset{\times}{\omega}_1^e \\ -\overset{\times}{\omega}_2^e & \overset{\times}{\omega}_1^e & 0 \end{pmatrix} \quad (4.14)$$

is a skew-symmetric matrix containing the principal rotation axis $\overset{\times}{\boldsymbol{\omega}}^e$ and which, as indicated in Sec. 4.4, is obtained from the axis-angle pair of the crystal at every spatial point.

The gradient of the lattice rotation field delivers the lattice curvature tensor. In the small deformation limit, the gradient of the rotation tensor is represented by the gradient of the axial vector

$$\boldsymbol{\kappa} := \nabla_x \overset{\times}{\boldsymbol{\omega}}^e, \quad (4.15)$$

i.e.,

$$\kappa_{ij} = \frac{\partial \overset{\times}{\omega}_i^e}{\partial x_j}.$$

Expanding the curl of $\boldsymbol{\omega}^e$ (Eq. (4.13)) using Eq. (4.14) yields

$$\begin{aligned}
\text{curl } \boldsymbol{\omega}^e &= \begin{pmatrix} -\frac{\partial \omega_3^e}{\partial x_3} - \frac{\partial \omega_2^e}{\partial x_2} & \frac{\partial \omega_2^e}{\partial x_1} & \frac{\partial \omega_3^e}{\partial x_1} \\ \frac{\partial \omega_1^e}{\partial x_2} & -\frac{\partial \omega_3^e}{\partial x_3} - \frac{\partial \omega_1^e}{\partial x_1} & \frac{\partial \omega_3^e}{\partial x_2} \\ \frac{\partial \omega_1^e}{\partial x_3} & \frac{\partial \omega_2^e}{\partial x_3} & -\frac{\partial \omega_1^e}{\partial x_1} - \frac{\partial \omega_2^e}{\partial x_2} \end{pmatrix} \\
&= \begin{pmatrix} -(\kappa_{33} + \kappa_{22}) & \kappa_{21} & \kappa_{31} \\ \kappa_{12} & -(\kappa_{11} + \kappa_{33}) & \kappa_{32} \\ \kappa_{13} & \kappa_{23} & -(\kappa_{22} + \kappa_{11}) \end{pmatrix} \\
&= \boldsymbol{\alpha}.
\end{aligned} \tag{4.16}$$

In tensorial form, this is equivalent to

$$\boldsymbol{\alpha} = \boldsymbol{\kappa}^T - \text{Tr}(\boldsymbol{\kappa})\mathbf{I}, \tag{4.17}$$

which is Nye's formula,[102, 136] given as Eq. (4.3) in Section 4.4.

4.10 CPU cost of Nye tensor extraction software

The scaling of the computational cost associated with mesh size in our GND tensor analysis is shown in Fig. 4.10 (for the 80-Å loop calculations). The two main trends observed in the figure are:

- There is a clear association between CPU cost and mesh size, characterized by an inverse nonlinear law (continuous lines in the figure). Above approximately a mesh size of 30 nm, the CPU cost saturates at values of 0.3 s per nm of dislocation segment length. This occurs as a consequence of the fact that mesh elements fully contain the loop beyond that size.

- The CPU cost t_{CPU} is seen to decay exponentially with mesh size. However, the decay rate falls into two different regimes punctuated by a critical mesh size x^* . Accordingly, we fit the t_{CPU} data points to general exponential functions of the form:

$$t_{\text{CPU}} = \begin{cases} a_1 e^{b_1 x + c_1} & x < x^* \\ a_2 e^{b_2 x + c_2} & x \geq x^* \end{cases} \quad (4.18)$$

The fitting coefficients are given in Table 4.1. The transition at x^* takes place when the number of segment-cell intersections reaches a critical value, and is likely to be loop size and shape dependent.

- Involving the grain boundary in the analysis results in a two-to-three fold increase in CPU cost. This is related to the increased overhead associated with GB dislocations and extra cell-segment intersections.

The trends shown in the figure are virtually independent of supercell volume, as the code can parse through empty cells very quickly at practically no cost. They can be used a priori to estimate the CPU overhead of larger-scale computation involving high numbers of dislocation segments.

Table 4.1: Fitting parameters for CPU cost vs mesh size

Loop case	a_1	b_1	c_1	a_2	b_2	c_2	x^* [nm]
Before absorption	11.63	-0.23	1.37	11.43	-0.12	-0.93	21.5
Partially absorbed	16.70	-0.21	-0.16	16.57	-0.11	-2.42	22.5
Fully absorbed	8.30	-0.23	1.99	11.41	-0.10	-1.15	22.3

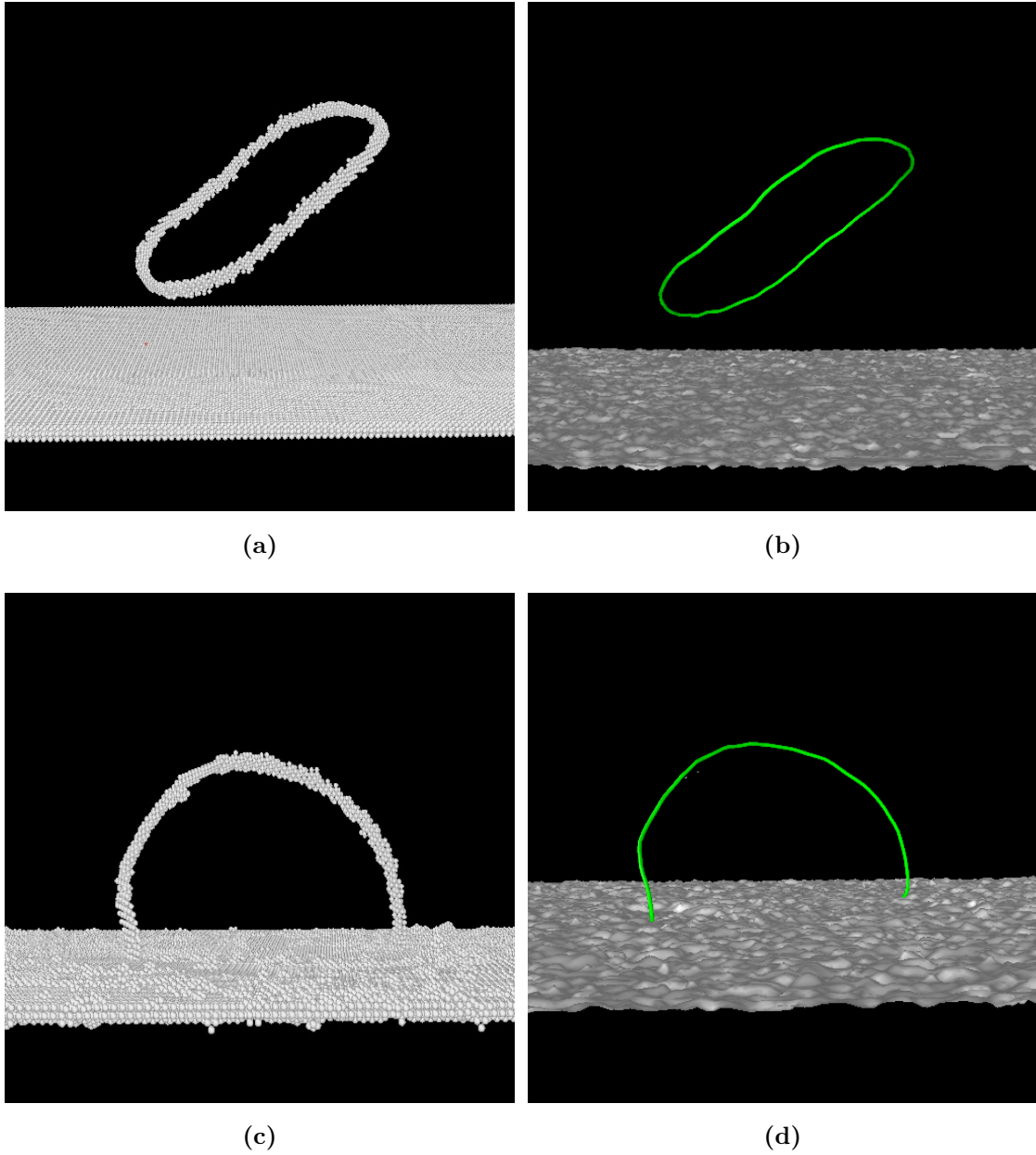


Figure 4.3: (a) Atomistic and (b) discrete line representation of an 80-Å $(a_0/2)[111]$ loop before absorption. (c) Atomistic and (d) discrete line representation of the partial absorption stage.

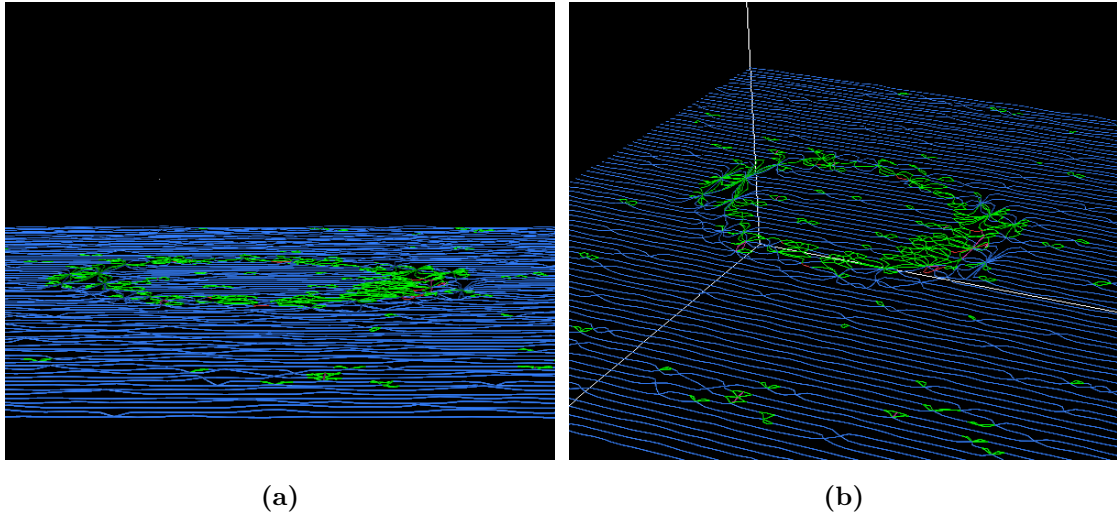


Figure 4.4: Two oblique views of the fully absorbed loop and the grain boundary using a DXA representation.

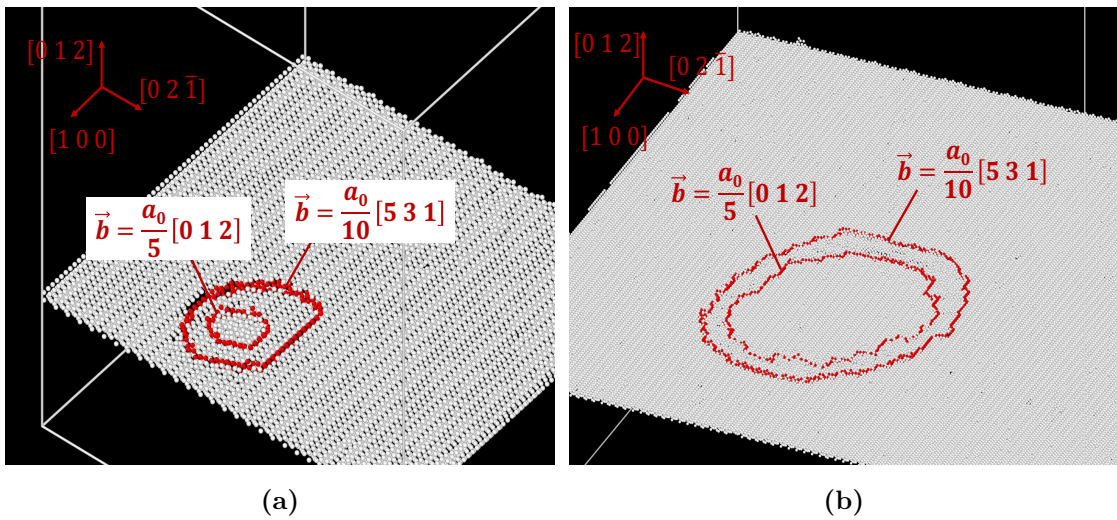


Figure 4.5: Absorbed dislocation loops in bcc Fe with original Burgers vector $(a_0/2)[111]$ and initial radii of (a) 20 Å and (b) 80 Å. The resulting disconnection loops and their corresponding Burgers vectors are shown and labeled.

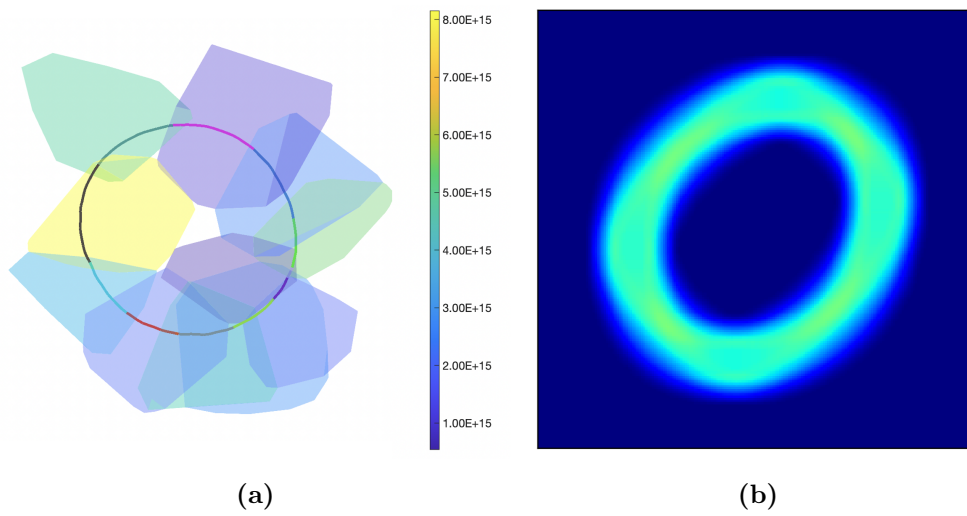


Figure 4.6: (a) Cells containing net dislocation loop segment length for an 8.0-nm Voronoi discretization of the full 80-Å loop. (b) Heat map of the full loop according to the GND intensity of the loop.

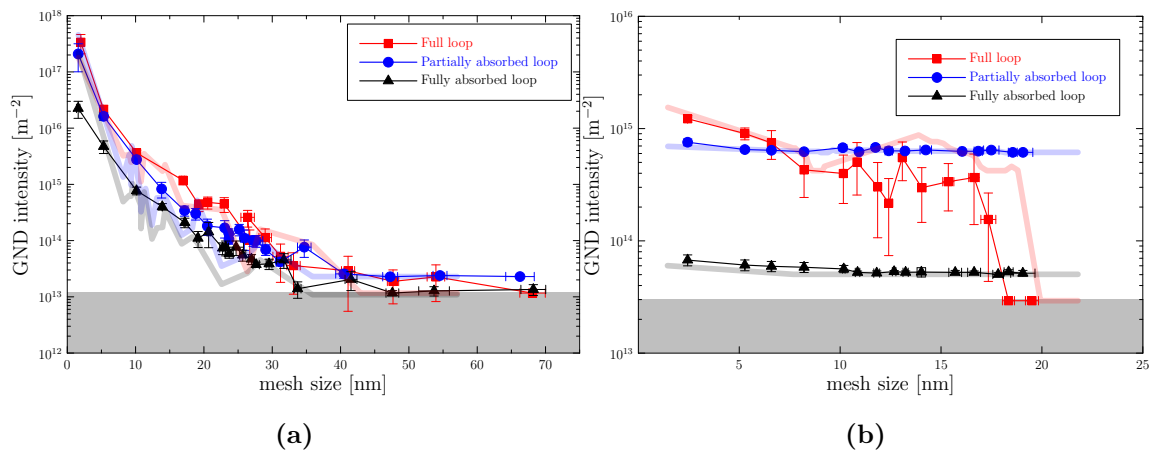


Figure 4.7: Normalized GND density for the (a) 80-Å and (b) 20-Å loops before, during and after absorption by the GB as a function of average Voronoi cell size. The error bars reflect the variability in tessellation morphology for a constant average mesh size. The shaded region represents the GND signal detection limit, while the translucent lines show the GND signal calculated based on regular hexahedral meshes for reference.

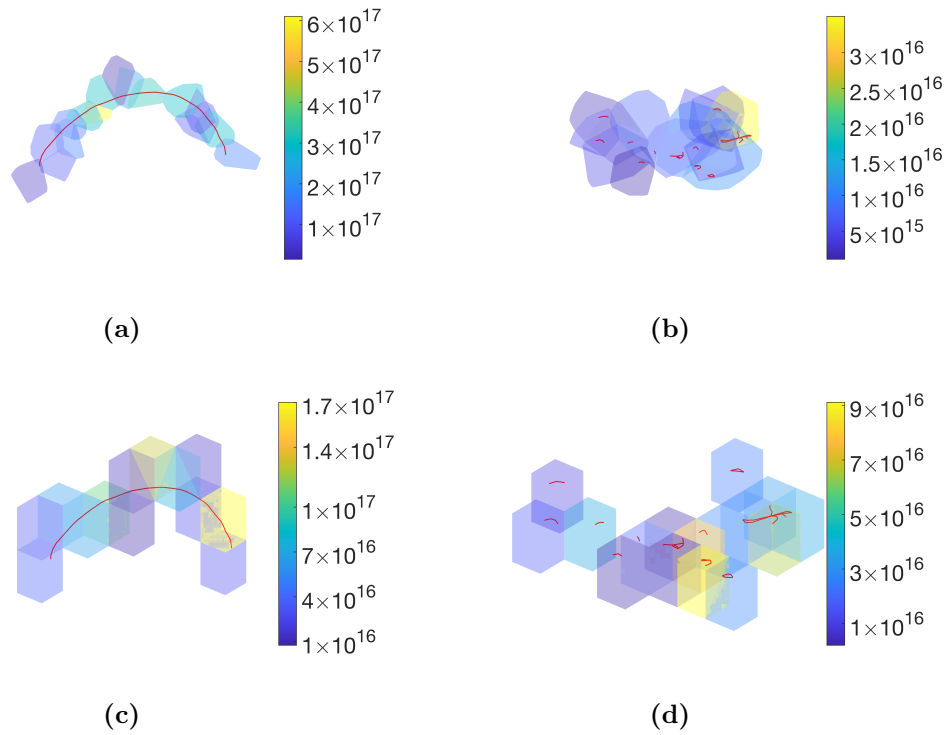


Figure 4.8: Highlighted Voronoi cells with net dislocation content for the (a) partially- and (b) fully-absorbed loops. The corresponding regular hexahedral mesh representations are given in (c) and (d), respectively. Cells are colored according to their GND density (shown in the color bars in units of m^{-2}).

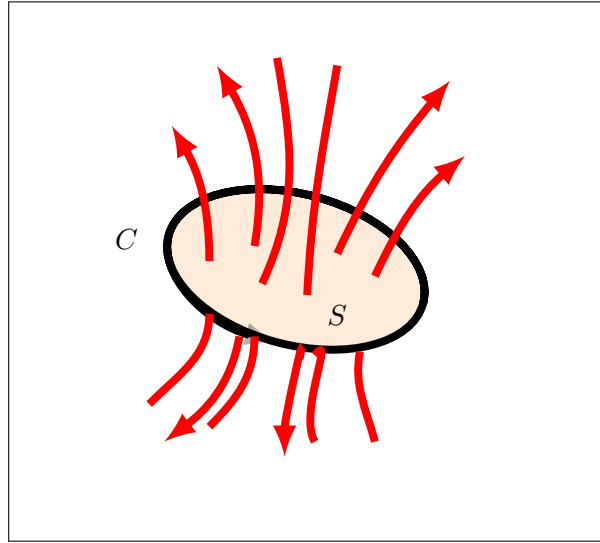


Figure 4.9: Dislocation lines crossing surface S bounded by closed circuit C .

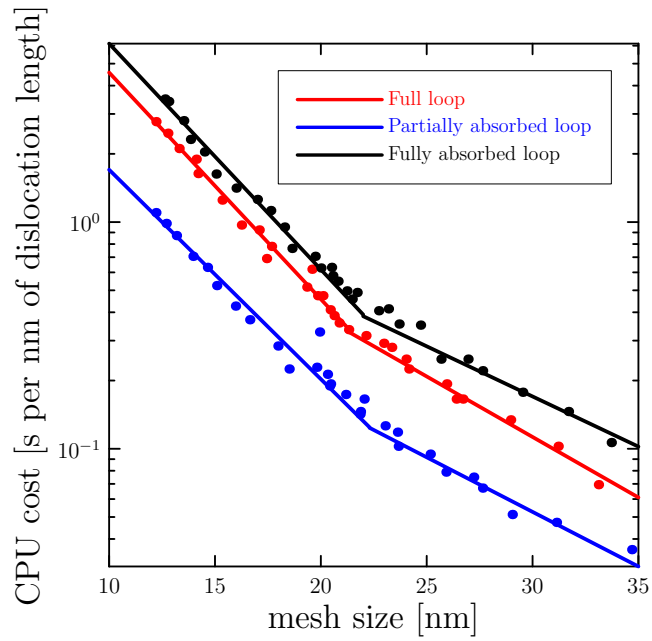


Figure 4.10: CPU cost per (dislocation segment length) of the GND analysis software for the three cases considered in the main text of this paper.

CHAPTER 5

Simulation of the evolution of Grain boundary's ability to absorb irradiation defects

The development of radiation-tolerant structural materials is an essential element for the success of advanced nuclear energy concepts. One of the most direct strategies to improve the response of materials to irradiation is to promote a high density of internal defect sinks. Sinks absorb and remove damage from the crystal, prolonging the material's lifetime by suppressing or delaying mechanical property degradation and maintaining safe performance. Grain boundaries (GB) have long been considered as effective damage sinks due to their flexibility to adjust their internal atomic structure to accommodate absorbed defects. As such, nanograined/nanostructured materials are considered to be optimal candidates as radiation-tolerant structural materials. However, as GB absorb defects, they suffer internal transitions to higher-energy microstates that limit their subsequent ability to continue to operate as effective sinks. In this paper, we show that, as the sink efficiency of GB becomes exhausted with increasing irradiation dose, networks of irradiation loops form in the vicinity of saturated or near-saturated GB, maintaining and even increasing their capacity to continue absorbing irradiation defects. The formation of these networks fundamentally changes the driving force for defect absorption at GB, from chemical (concentration gradient) to elastic (loop coalescence and Burgers vector reactions). Once formed, a

strong Nye tensor signal can be detected using precession electron diffraction, corresponding to measurable changes in lattice orientation due to geometrically-necessary dislocation (GND) accumulation. We show using dislocation dynamics simulations with thermally-activated diffusion in nanocrystalline iron that these GND signals are consistent with sessile structures stabilized by $\langle 100 \rangle$ segments formed by reactions among small prismatic loops with $1/2\langle 111 \rangle$ Burgers vectors. Our results display a remarkable quantitative agreement between the simulated and measured GND densities, validating the idea that loop networks are a natural continuation of the GB once they exhaust their defect absorption capacity.

5.1 Introduction

Materials containing a large internal surface-to-volume ratio are important in many technologically important areas of science, including catalysis [222, 223, 224], mechanical strength [225], magnetism [226] or corrosion [227, 228, 229]. In irradiated materials, grain boundaries (GBs) can act as effective sinks for defects, potentially resulting in an enhanced radiation resistance compared to their single crystal counterparts [230, 231, 232, 233, 234, 235, 236]. The best experimentally quantifiable indicator of GB sink efficiency has been the width of defect free areas adjacent to interfaces known as defect *denuded zones* (DZ). Denuded zones are a consequential side effect of defect interactions with GBs. Broadly speaking, these interactions can be related to the overall GB character¹, although extensive studies in recent times culminating in new findings and a much-improved understanding of the internal

¹Defined by the five-dimensional space consisting of misorientation and inclination degrees of freedom.

structure of GBs is fast changing this picture [227, 237, 238, 239, 240]. Indeed, in a previous work [8], we have shown that the evolution of the width of the DZ with irradiation dose is associated with changes in GB (internal) microstates. Transitions between different allowable GB microstates occur as a consequence of alterations in the atomic structure of GB due to absorption of irradiation defects. Such transitions are governed by a spectrum of time relaxation constants that reflect the hierarchy of microstate free energies and its partition function. Together, they set the interplay between irradiation dose rate and internal GB changes, leading to evolution equations that predict the time behavior of the DZ [95]. In other words, under irradiation, certain GBs exhibit denuded zone collapse without altering their overall macroscopic degrees of freedom (DOFs), i.e., these changes are solely navigated by internal transformations at the level of GB microstates.

However, while the macroscopic descriptors of the GB are seen to remain unchanged, Nye tensor analysis performed on these GBs reveals that DZ collapse manifests itself as an accumulation of *geometrically necessary dislocations* (GND) in the region previously occupied by the denuded zone itself. GND accumulation is typically interpreted as resulting from lattice curvature changes associated with the emergence of dislocation populations with an unbalanced Burgers vector. A problem immediately arises when trying to reconcile the observation of GND with the known fact that the only source of dislocation content in irradiated metals is the production of small, perfect prismatic loops originating within displacement cascades [241, 242, 243]. As such, these loops contribute no net GND density in a global sense (i.e., when the Nye tensor is calculated along the entire loop contour in a single sweep), and thus the puzzle of how they form still remains. Moreover, how these geometrically necessary dislocations are connected to DZ suppression is also lacking a proper physical

explanation.

In a previous paper we have shown that caution must be used when reconciling experimental GND footprints with a formal definition of the Nye tensor [244]. For one, we have shown that GND intensities are strongly dependent on the resolution of the discretization employed. This is crucially important when comparing simulated images with experimental signals extracted using a fixed spatial resolution. Trivially, the loop size sets the threshold discretization limit under which calculated GND densities deviate from the continuum definition of the Nye tensor. Ideally then, the experimental resolution should be tailored to the defect sizes expected under the particular irradiation conditions, which is of course highly impractical. Another aspect worth mentioning when comparing simulations and experiments is that pixelated Nye tensor images obtained under the microscope are eminently two-dimensional, which projects three-dimensional features onto the imaging plane with the consequent loss of configurational information.

The above issues relate to the handling of microscopic experimental information and its relationship to the numerical aspects of the Nye tensor determination. They do not address, however, the physics gap separating the emergence of a GND footprint with the collapse of the denuded zone in irradiated materials. The main objective of the present paper is to provide a physical picture that reconciles experimental GND density measurements, notional definitions of the Nye tensor, and a connection between microstructural evolution under irradiation and changes in the microstates of a GB. Our model is based on the presumption that a dislocation network emerges in the GB-adjacent region during irradiation as the GB defect absorption efficiency evolves toward saturation. Indeed, we consider this dislocation network to be a main component of the sink efficiency, and thus, it must be taken into account in our con-

sideration of the role played by GBs during irradiation. Our work provides potential channels to control sink strength by tailoring these GB-adjacent regions, which could have a marked impact on the effectiveness of optimizing radiation tolerance using techniques such as GB engineering.

The paper is organized as follows. First, we present the physical hypotheses behind the formation of imbalanced GND networks forming as a consequence of GB sink efficiency loss and the accumulation of small irradiation loops. Second, we introduce the experimental observations and the techniques employed to extract and interpret quantitative information from them. We then describe the numerical methods used to generate Nye tensor signals and discuss the main simulation parameters. Next, we show that dislocation networks of the type hypothesized earlier, are a natural manifestation of the irradiation damage microstructure during the loss of defect absorption efficiency by GBs. Subsequently, a comparison between the Nye tensor signals emerging from these networks and experimental signals is carried out, providing the basis for validation of our mechanistic hypotheses and confirmation of the physical interpretation of the experimental images. We finalize with a discussion of the results and our most important conclusions.

5.2 Mechanism of network formation near saturated grain boundaries under irradiation

A closed dislocation loop of any character yields no net GND signal. This is readily seen from the mathematical definition of the Nye tensor, $\boldsymbol{\alpha}$:

$$\boldsymbol{\alpha} = \frac{1}{V} \oint \mathbf{b} \otimes d\mathbf{l} \quad (5.1)$$

where V is the system volume, \mathbf{b} is the Burgers vector, and $d\mathbf{l}$ is an infinitesimal length vector that runs along the loop's geometric contour, and which is usually expressed as a normalized vector so that $\boldsymbol{\alpha}$ can directly represent a dislocation density. For convenience, it is common to use scalar values of the Nye tensor by working with the norms $\|\boldsymbol{\alpha}\|_1$ or $\|\boldsymbol{\alpha}\|_\infty$.

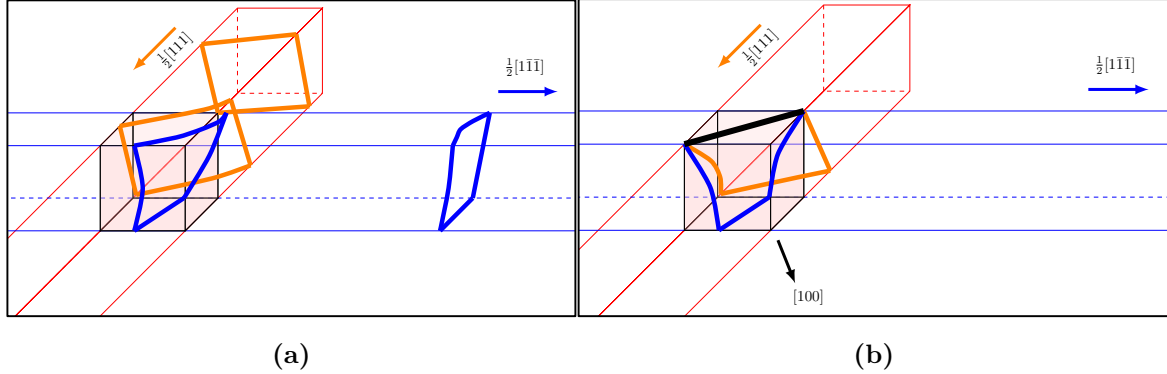


Figure 5.1: Schematic sequence of two square $\frac{1}{2}\langle 111 \rangle$ prismatic dislocation loops (orange and blue) (a) gliding along their glide prisms (delineated by the thin orange and blue lines) on a collision trajectory; (b) coming into contact within the reaction volume (shaded cube); and (c) reacting to form a $[100]$ junction along their common intersection. The process is driven by elasticity and unidimensional random diffusion (1D Brownian motion). The junction (black segment) is unbalanced and satisfies the Burgers vector reaction $\frac{1}{2}[111] + \frac{1}{2}[1\bar{1}\bar{1}] \rightarrow [100]$.

From eq. (5.1), a nonzero $\boldsymbol{\alpha}$ implies the existence of a Burgers vector imbalance which is incompatible with a closed loop. However, the notion of a net nonzero GND signal originating from irradiation defects consisting exclusively of closed prismatic

can be reconciled considering the following two processes: The first one involves the incomplete absorption of prismatic loops, either as a consequence of GB saturation or due to a topological incompatibility between a loop’s Burgers (lattice) vector and admissible displacement-shift complete (DSC) vectors [244]. The second involves processes such as that presented in Fig. 5.1, which shows a schematic diagram of the reaction between two $\frac{1}{2}\langle 111 \rangle$ prismatic dislocation loops gliding in their respective glide cylindrical (shown as quadrangular prisms for simplicity). This is consistent with motion by one-dimensional random walk typical of small prismatic loops generated in displacement cascades [245, 246]. In isolation, each of these loops contributes zero Nye tensor signal. However, the two loops eventually enter the coincident glide volume (shown as a shaded orange cube) and react according to the dislocation reaction:



which is an exothermic reaction according to Frank’s rule [247]. As a result, a $[100]$ segment is created, shown in black in Fig. 5.1. Specifically, in α -Fe-Fe, $\langle 100 \rangle$ segments have very high migration energies and anchor otherwise highly-mobile $\frac{1}{2}\langle 111 \rangle$ loops into sessile, i.e., immobile, structures [248, 249, 250]. Crucially, the $\langle 100 \rangle$ segment is now unbalanced and it then does contribute a net GND signal when the spatial discretization over which such signal is analyzed has a similar size as the original loops. This can be seen in Fig. 5.2a, where the simulated GND footprint of two hexagonal $\frac{1}{2}\langle 111 \rangle$ prismatic loops in 2D is shown both when they are separated by some distance and also when they react forming a $\langle 100 \rangle$ segment. It is clear that, in isolation, the loops do not produce a significant footprint, whereas an intense

signal is detected for the unbalanced $\langle 100 \rangle$ segment. However, for discretizations larger than the whole reacted structure, the net GND signal still adds up to zero for a closed loop. See mesh size analysis in ref. [247].

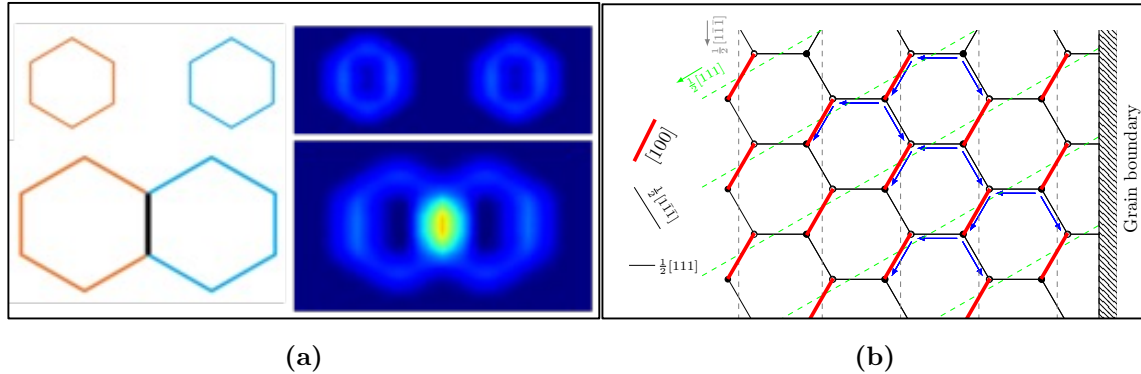


Figure 5.2: (a) Simulated GND footprints of two hexagonal $1/2\langle 111 \rangle$ prismatic loops when (top) they are separated beyond their reaction distance, and (bottom) after reaction along one of their edges (color map in arbitrary units). Color coding: ■ $1/2[\bar{1}11]$; ■ $1/2[\bar{1}\bar{1}\bar{1}]$; ■ $[\bar{1}00]$. (b) Schematic representation of an idealized prismatic loop network composed of $\langle 111 \rangle$ and $\langle 100 \rangle$ segments forming from a saturated grain boundary (located on the right edge of the image).

The above two processes are not mutually exclusive and constitute the elementary mechanisms by which a ‘network’ composed of $1/2\langle 111 \rangle$ and $\langle 100 \rangle$ segments can form by the sustained arrival of irradiation loops to a saturated GB. The mechanism would proceed in a series of sequential steps, described in the following:

1. Once the GB is no longer able to absorb the incoming defects at the speed dictated by the irradiation dose rate, SIA loops become only partially absorbed. This leads to a population of ‘half’-loops on top of the GB plane. This is illustrated by the segments that directly abut to the GB in Fig. 5.2b (righthand

side of the image).

2. Subsequent migration of prismatic loops results in segment-segment interactions near the GB. Occasionally, some of those interactions result in reactions of the type shown in Fig. 5.1 and eq.(5.2). With time, a network consisting of $1/2\langle 111 \rangle$ and $\langle 100 \rangle$ segments starts to form adjacent to the GB.
3. Several layers of reactions lead to the buildup of a network against the saturated GB. An idealized representation of this network is shown in Fig. 5.2, where all four $1/2\langle 111 \rangle$ Burgers vectors of the body-centered cubic lattice are indicated.

In reality, actual networks are not ideal, and consist instead of irregular configurations of dislocation segments, some looking like coalesced loops, some containing $\langle 100 \rangle$ junctions, generally arranged spatially in a heterogeneous manner. Note that, once a GB has saturated its capacity to absorb damage, the main driving force for the arrival of prismatic loops to the GB is the elastic energy reduction associated with the reaction shown in eq.(5.2) (which results in a 33% reduction in elastic energy). Also, it is worth noting that, while the present analysis does not require that the nature of the loops –i.e., whether they are of self-interstitial atom (SIA) or vacancy type–, be specified, it is known that in cubic crystals the vast majority of prismatic loops created are of SIA type, transitioning from 3D to 1D migration paths above a critical loop size [251, 252].

Next, we carry out detailed simulations of the mechanism just presented under constraints designed to mimic experimental conditions and obtain their corresponding Nye tensor representation. The network structure depends, among others, on the diffusion behavior of the loops (set by the temperature), their relative trajectories (set by the crystal structure), mutual elastic interactions (set by the loop sizes and

shapes), and their production rate (primarily set by the irradiation particle energy and dose rate). More importantly, these relaxed networks give rise to Nye tensor fingerprints that can then be directly compared with experiments specifically performed to enable such evaluations.

5.3 Methods

5.3.1 Experimental

5.3.1.1 Film preparation, irradiation, and characterization

Nanocrystalline iron thin films were deposited via balanced DC magnetron sputtering using a 99.9% pure Fe target onto polished substrates of NaCl (100) single crystal substrates and prepared as detailed by Vetterick et al [253]. The resulting thin films had a nominal thickness of 100~150 nm. In preparation for thin film liftouts, cleaved thin film samples were prepared by floating off and bonding films onto 200-mesh TEM grids. Liftouts of columnar, polycrystalline Fe film were generated using a focused ion beam (FIB) and cross sections were characterized using a 200-kV JEOL 2100 LaB66 TEM at Sandia National Laboratories. The samples were irradiated using 10-keV He⁺ ions with a 10-kV Colutron source at a dose of 3.7×10^{-3} dpa/s and a temperature of 573 K [88]. As explained in these and other studies, a large proportion of the implanted He ions is likely to bind itself by to vacancies of their own creation [254], or created by recoils, thus immobilizing and disconnecting them from further evolution.

Bright-field TEM images acquired during in situ irradiation were collected at a constant two-beam diffraction condition, and in situ irradiation videos were captured

at a frame rate of 30 frames per second. Intermittent precession electron diffraction (PED) automated crystallographic orientation mapping (ACOM) was conducted throughout irradiation at doses of 0.0, 6.1, 12.2, and 18.3 dpa to demonstrate structural evolution with respect to dose [255, 256]. PED-ACOM data was used for GND density calculation inputs [2].

5.3.1.2 Grain boundary structure and experimental Nye tensor analysis

GND signals are observed via mapping of lattice curvature gradients according to:

$$\boldsymbol{\alpha} = \boldsymbol{\kappa}^T - \text{Tr}(\boldsymbol{\kappa})\mathbf{I} \quad (5.3)$$

which is known as Nye’s equation, linking the curvature gradient tensor to the GND tensor cote [257, 2, 258]. The components κ_{ij} are obtained as the local gradient of the lattice orientation map, i.e., $\kappa_{ij} = \partial\omega_i/\partial x_j$, where ω is the lattice orientation vector, which is in turn obtained from discrete pixelations of spatially resolved PED-ACOM data. A scalar metric of the GND density ($\|\boldsymbol{\alpha}\|_1$ in our case) is then used for graphical representation [244].

5.3.2 Computational models

5.3.2.1 Physics modeling of irradiation loop dynamics

The computational methodology developed in this work is designed to capture irradiation loop diffusion and elastic interactions, including self-interactions (i.e., between segments belonging to the same loop) and loop-loop interactions (between segments belonging to different loops). Diffusion is modeled following the physical

mechanism ascribed to prismatic loops generated in displacement cascades, namely, one-dimensional diffusion (1D) along the Burgers vector direction. The diffusivity for one such loop is inversely proportional to the loop size, given by the expression [252]:

$$D(T, \boldsymbol{\sigma}; n) = D_0(n) \exp\left(-\frac{\Delta Q(\boldsymbol{\sigma})}{kT}\right) \quad (5.4)$$

where T is the absolute temperature, $\boldsymbol{\sigma}$ is the stress tensor at the position of the loop, and n is the number of SIA in the loop. $D_0(n) = 8.89 \times 10^{-3} n^{-0.61}$ (in cm^2s^{-1}) is a diffusion pre-factor that captures the defect size dependence of the loop diffusivity and $\Delta Q(\boldsymbol{\sigma})$ is an activation energy that depends on the local stress state. $\boldsymbol{\sigma}$ is obtained within a non-singular linear elasticity framework implemented in a dislocation dynamics (DD) code. $\Delta Q(\boldsymbol{\sigma})$ comprises a crystallographic contribution, ΔE_m , associated with migration along the prismatic coordinate, and an elastic contribution, $\Delta W_{el}(\boldsymbol{\sigma})$, associated with the work done by the elastic forces during loop glide:

$$\Delta Q(\boldsymbol{\sigma}) = \Delta E_m - \Delta W_{el}(\boldsymbol{\sigma}) = \Delta E_m - \mathbf{f}_{el} \mathbf{b} L \quad (5.5)$$

where \mathbf{b} is the Burgers vector and \mathbf{f}_{el} is total elastic force on a segment of length L . In DD methods, \mathbf{f}_{el} is obtained as the linear superposition of the Peach-Köhler force originating from all other segments in the simulation cell, i.e., $\mathbf{f}_{el} = \sum_i \boldsymbol{\sigma}_i (\mathbf{b} \times \mathbf{t})$, where the subindex i runs over all dislocation segments (43). With this, the loop dynamics is controlled by the following set of equations:

$$\mathbf{v} = \mathbf{M} \mathbf{f}_{el} \quad (5.6)$$

$$\delta x = v\delta t \pm \xi\sqrt{2D\delta t} \quad (5.7)$$

where \mathbf{M} is the dislocation mobility tensor (further explanation about \mathbf{M} is given in the Supplementary Materials), v is the velocity vector ($v = \|\mathbf{v}\|$ is its modulus), ξ is a uniform random number between 0 and 1, and δt is the timestep. The segment displacement, δx , is thus a combination of a ‘mechanical’ contribution, and a ‘thermal’ or diffusive one. Note that the diffusive contribution is treated here as a stochastic (Wiener) process and thus can be in the direction of or against the elastic forces (as represented by the ‘ \pm ’ symbol in the equation). Moreover, for a closed prismatic loop, the mechanical contribution has the effect of torquing the loop, which induces no net displacement. As such, defect migration is controlled by the thermal component until segment-segment collisions take over as the dominant process.

5.3.3 Calculation and processing of GND fingerprints

The relaxed network configurations are processed with GND fingerprint parsers developed by the authors [244]. First, the simulation volume containing the network is discretized by tessellating it with the desired spatial resolution. The parser then identifies the intersections between mesh cells and dislocation loops, and places nodes at the intersection sites on the cell boundaries. The GND density is then calculated in each cell according to eq. (5.1) and the resulting cell densities are processed using the Plotly library [259] to generate 3D color maps with a prescribed signal intensity spread.

5.4 Results

5.4.1 Experimental GND maps as a function of irradiation dose

Fig. 5.2b shows the change in GND density with dose of four distinct grains in the irradiated material (illustrated in rows A-D in the figure). The microstructure is seen to undergo a highly heterogeneous temporal and spatial GND density evolution, with clear distinctions depending on the grain matrix observed. The most salient features that can be reasonably extracted from the observations are:

1. As shown in all figures, different grain boundaries behave differently, even in adjacent GBs belonging to the same grain,
2. Figs. 5.3A and 5.3C reveal a gradual transfer with increasing irradiation dose of GND density from the grain interior towards the GB.
3. Figs. 5.3B and 5.3C display the existence of twin boundaries, captured as elongated high-GND intensity planes.
4. Strong redistributions of GND content can be appreciated in Fig. 5.3B. GND appear to concentrate first near GBs and in selected locations inside the grain (possibly along native dislocation lines), subsequently accumulating in half of the grain volume, depleting the other half to practically zero GND concentration.
5. None of the native grain boundaries is seen to displace or suffer any transformation that suggests changes in GB macrostates.

Next, we present simulation results designed to put our network formation hypothesis to the test and add insight to the experimental observations.

5.4.2 Simulation results

To carry out the simulations, we construct a computation cell with dimensions $20 \times 20 \times 20$ nm, with the grain boundary being one of the external edges of the computational cell and periodic boundary conditions in the two directions parallel to the GB. The GB normal corresponds to the crystallographic direction [012] of the computational cell's crystal lattice, representing a $\Sigma 5$ boundary with 53.1° misorientation. Loops are generated at a distance of 20 nm from the GB at a random location relative to the two-dimensional GB plane. The Burgers vector is assigned at random among the four $\langle 111 \rangle$ independent directions in the body-centered cubic (BCC) crystal lattice. The loops all have hexagonal shape and have a size (hexagon width) ranging between 2.5 and 5.0 nm, assigned at random. This mimics reasonably well the defect shapes and size distributions observed in most studies of Fe irradiation [260, 261]. Using the GB area and the number of loops entering the simulation cell, we correlate loop densities to irradiation dose.

5.4.2.1 Formation and evolution of the dislocation loop network

We start with a pristine planar GB assumed to be in a saturated state, i.e., unable to fully absorb incoming defect loops. Instead, loops become partially absorbed, giving rise to substructures such as that shown in Fig. 5.4a. After a certain irradiation dose, these substructures 'blanket' the GB, leaving no exposed surface for subsequent loops to directly interact with the boundary, Fig. 5.4b. The next loop interacts instead with one or several of the partially absorbed loops, as shown in Fig. 5.4c. This interaction is spatially complex, as it is governed by elasticity in 3D and loops of various sizes and orientations. Here is where the DD module becomes critical, to

capture long-range elastic interactions and apply short-range inelastic interaction rules (segment-segment reactions). After considering several hundred loop arrivals corresponding to an approximate a total dose of 1.0 dpa, a network is formed in the near-GB region, as shown in Fig. 5.4d.

This network displays several interesting features. The main outcome of loop-loop interactions in the near-GB region is (i) coalescence of two loops with the same Burgers vector, and (ii) the formation of $\langle 100 \rangle$ segments from reactions between loops with dissimilar ones. Both of these can be appreciated in Fig. 4d ($\langle 100 \rangle$ junctions colored in pink). The conditions for prismatic loop coalescence have been studied in detail by McElfresh et al. (refs) and are also briefly discussed in Section S.2 in the Supplementary Material. We have simulated 10 independent configurations with the same conditions as those in Fig. 5.4, all with similar qualitative outcome (see Section S.3 in the Supplementary Material for more examples). For statistical significance, we also have simulated 60×60 -nm GB plane configurations, which we use to generate GND fingerprint images in the next subsection.

5.4.2.2 GND analysis

Fig. 5.5 shows a color map of a loop network configuration relaxed over a GB plane with 60×60 (nm dimensions). The image is then processed according to the procedure described in Section 3.2.2 using a pixel resolution of 10 nm and a spread of 5 nm. Note that this is consistent with the experimental resolution of 10–12 nm used in the studies referenced earlier [88, 2], and appropriate to avoid any analysis artifacts related to the spatial discretization, i.e., sufficiently coarse to not produce a net GND signal for individual loops, but fine enough to detect segments with unbalanced

Burgers vectors due to loop reactions. Fig. 5.5 shows two views, one directly edge-on to the GB plane and another tilted by 30° for oblique view. The color map has been chosen to capture the range of GND densities measured in the experiments (using the same color palette as well for ease of comparison). Our analysis thus confirms that irradiation loop networks can indeed furnish GND fingerprints detectable through lattice curvature measurements with nanometer resolution.

As well, it is of interest to analyze the intense GND bands traversing the grains in Figs. 5.3B and 5.3C. Our starting hypothesis is that these correspond to pre-existing low-angle boundaries (e.g., $\Sigma 3$ or $\Sigma 5$) created during processing prior to irradiation. Taking as an example the configuration contained in the area indicated by the dashed line in Fig. 5.3C, we carry out an analysis of the GND density assuming that it corresponds to a thin twin plate bounded by two $109^\circ\langle 110\rangle\Sigma 3$ twin boundaries. The results are shown in Fig. 5.6, where the associated lattice orientation component along the $\langle 110\rangle$ direction is shown along with its gradient, the lattice curvature. As shown, the GND fingerprints corresponding to this configuration display are characterized by dislocation densities that are one order of magnitude larger than those shown in Fig. 5.5. A similar analysis performed for a $\approx 37^\circ\langle 100\rangle\Sigma 5$ boundary led to identical results, thus confirming the nature of the structure shown in the inset of the figure.

Next, we discuss the most important aspects of our results and the implications for the interpretation of microstructural evolution in irradiated nanocrystalline materials.

5.5 Discussion

The present paper incorporates two original contributions that are worth discussing in more detail. First, we introduce a hypothesis explaining the reasons behind the emergence of strong GND fingerprints with irradiation dose near grain boundaries. This hypothesis is then tested using our advanced models for defect transport and evolution. Second, we provide a quantitative comparison of simulated/calculated GND fingerprints with experimental images, with considerable agreement achieved between both approaches.

5.5.1 Phenomenology of denuded zone evolution near grain boundaries in irradiated crystals

Structural materials for advanced nuclear energy concepts (e.g., fusion energy) will have to contend, among other things, with unprecedented levels of irradiation dose. Materials will not be capable of withstanding these high doses unless the concomitant irradiation damage defects are removed –to a large degree– as they are being produced. Grain boundaries have long thought to be effective defect sinks, which has brought nanocrystalline materials to the forefront of radiation tolerant material design strategies. However, GBs are not ideal sinks, at least not permanently, and their efficacy in removing irradiation defects must be carefully studied. Denuded zone formation and ‘collapse’ is seen as a strong marker of GB defect absorption efficiency, as its existence –or lack of– can be directly mapped to defect concentration profiles near GBs that are directly influenced by their sink strength. Previous work has established a clear connection between this sink efficiency and the macroscopic GB character [237, 262], as well as between sink efficiency and DZ formation

[88, 81, 263, 264, 265, 89]. However, we have recently demonstrated that changes in absorption efficiency can lead to denuded zone collapse without the need for a change in macroscopic GB degrees of freedom [8]. Our work has also shown that changes in irradiation defect concentration can be mapped to changes in the GND density [8, 244, 2]. However, interpreting these GND signals in the context of irradiation damage production was not clear, as defects are universally produced as small, closed loops that should in principle contribute no net Nye tensor fingerprints. The work presented in this paper attempts to provide the link that explains the equivalence between observed GND fingerprints and what we know about damage production. We prove that networks of damage loops can be shown to produce nonzero Nye tensor signals. The preconditions for these networks to form are:

1. DZ collapse must have occurred as a prior condition. This means that the GB may have run through its entire hierarchy of available microstates, exhausting its ability to accommodate defects via changes in its internal degrees of freedom.
2. Subsequently, the exposed surface of the saturated GB must undergo a partial coverage with semi-absorbed loops (Fig. 5.4b). This process is likely to be the rate-limiting step in the entire process.
3. The material in question must allow reactions among damage loops that change the balance of Burgers vector along the loops' perimeters. Mathematically, this amounts to a closure failure of the integral in eq.(5.1). In the present case, such reactions are represented by eq.(5.2).
4. The formation of these networks immobilizes defects near the GB region, resulting in a gradual transfer of matter from the grain's interior towards the

grain boundary. The kinetics of the process switches from being driven by chemical forces (concentration gradients) to mechanical ones (elastic forces). This represents a partial paradigm change, as it is the network now—instead of the GB *per se*—who acts as the sink for defects going forward in time.

5.5.2 Discussion on simulation methods and comparison with experimental results

While DD models have been extensively used to simulate dislocation loop dynamics [266], our model adds two original elements that are worth discussing. First, it captures loop reactions of the type described by eq.(5.2), which gives rise to experimentally-observed $\langle 100 \rangle$ segments typical of irradiated Fe microstructures. Second, it simulates a (semi-)saturated GB as a planar boundary with partially absorbed, immobile, prismatic loops. This is based on molecular dynamics simulations of prismatic loop interactions with a $\Sigma 5$ boundary [244]. Our model also captures all four independent $1/2\langle 111 \rangle$ Burgers vectors of the bcc crystal lattice, which thus sets no geometric limitations on the space of dislocation reactions among different irradiation loops.

In terms of comparison, as Fig. 5.5 shows, the color map of the GND fingerprints in the simulated structures and the experimental images are in good agreement in regard to the accumulated GND densities. Although GND fingerprints are a scalar integrated quantity where much of the fine details of the microstructure are lost, this confirms (i) that the loop sizes, shapes, densities, and network structure considered in the models are consistent with the experimentally revealed structures, and (ii) the correspondence between the physical manifestation of the Nye tensor according to its

two definitions, eqs.(5.1) and (5.3), i.e., the equivalence between the dislocation based definition used in the DD model and the one based on lattice curvature gradients considered in the experiments.

In real specimens, which are thin TEM discs with thicknesses on the order of 150 nm, surface sinks will compete with grain boundaries for mobile loops [267] likely delaying the onset or formation of the absorbing loop network near GBs relative to bulk specimens such as those nominally represented by the simulations. A proper treatment of the effect of the free surfaces on the time scale of network formation requires a more detailed computational analysis where the geometry of the TEM is explicitly considered, but this is presently beyond the scope of this work. For this reason, however, the comparison between the observed doses at which the network forms in experiments and simulations should be done with caution.

5.5.3 Consistency of the present results with radiation damage theories

Defects are produced in displacement cascades in numbers and sizes that vary across material type, particle type and energy, temperature, and existing microstructure. Thanks to several decades of research combining detailed electron microscopy and atomistic simulations, we now have a deep understanding of the structure and numbers of these irradiation defects. Although we cannot ascertain from images such as those shown in Fig. 5.3 what the nature of the observed defect is, we can confidently infer that they are of SIA type. Indeed, it is known that in cubic metals the large mobility difference between SIA and vacancy defects tilts the balance towards a preferential arrival of self-interstitial clusters at defect sinks. Moreover, SIA clusters move along rectilinear paths, covering much longer distances than vacancy defects in

the same amount of time. Such features form the basis of one of the pillars on which irradiation damage theory rests: the so-called production bias model. This informs our models, and the relatively good agreement between the simulated and experimental GND fingerprints, both qualitative and quantitative (referred to the total GND densities) is an indirect confirmation of the partial validity of our assumptions as it relates to prismatic loop sizes and shapes.

Moreover, while the temperature at which the irradiations were carried out (573 K) is well above the stage III temperature in Fe (≈ 200 K [268], at which monovacancies become mobile), it is worth remarking that the injection of He ions during implantation has the immediate effect of immobilizing monovacancies and vacancy clusters, allowing self-interstitial clusters to escape the cascade region and favor their accumulation near the GB without the delayed recombination effect. This is likely to facilitate the formation of loop networks with strong GND signals, as vacancies remain trapped by He atoms in the interior of the grain, or are released in negligible concentrations, not sufficient to affect the formation of the network.

The other pillar, referred to as the dislocation bias model, refers to the preferential absorption of SIA clusters by defect sinks. Once again, our models are consistent with this picture, taking a saturated GB –i.e., one which has exhausted its ability to absorb more damage loops– as the starting configuration for our simulations. From this, an interesting picture emerges wherein as a GB exhausts its capacity to absorb damage loops, the system ascribes a strip of material immediately adjacent to the grain boundary to continue storing defects. In other words, the effective thickness of the GB widens as to maintain a high sink efficiency overall. This could be a natural mechanism to keep absorbing damage when the actual GB has become saturated. This is reminiscent of the notion of complexions in deformed nanocrystalline systems

[269, 270, 271], which act as extensors of the disordered region of a GB beyond the strict interface separating two grains with dissimilar orientations.

5.6 Conclusions

We finish the paper with our most important conclusions:

1. We have developed a discrete dislocation dynamics that incorporates thermal motion of dislocation loops to simulate loop network formation and evolution near grain boundaries in irradiated Fe. The model successfully predicts the formation of a prismatic dislocation loop network near a saturated grain boundary. The network is stabilized by energy-reducing dislocation-dislocation interactions such as coalescence and the formation of $\langle 100 \rangle$ junctions.
2. We have processed the complex dislocation loop network structure with software that extracts and images its GND content, enabling direct comparison with Nye tensor analysis of experimental lattice curvature observations using precession electron diffraction. We find a remarkable agreement between the GND fingerprints generated by the simulated network and those measured experimentally.
3. We find that loop networks can maintain a high defect sink efficiency once the actual GB has become saturated, switching the absorption mode from being concentration-driven to elastically driven. The network thus acts as a functional extension of the GB as a defect sink once the latter have exhausted their ability to absorb damage.

4. One of the implications of our findings is that the collapse of the denuded zone does not necessarily imply an inability for self-healing in irradiated materials. In systems that favor (or enable) the formation of loop networks, a high sink efficiency can be maintained even after DZ collapse, maintain the material's ability to tolerate higher irradiation doses.

Finally, although our work is helping reveal some of the fundamental mechanism of microstructural evolution in irradiated nanocrystalline systems, several outstanding questions remain, including:

- Once DZ collapse takes place and the network forms, can the DZ establish itself again by self-healing processes in the GB? In that case, what happens to the loop network?
- How do the processes in the interior of the grain inform the dynamics of DZ collapse/network formation?
- Here we have studied what takes place in a specific GB, but how is the formation/evolution of the network affected by other grain boundaries in the same grain or in the other side of the same GB?
- What controls the thickness of the network that can form? What is the extent of the region near the grain boundary that can sustain the formation of the network. Put differently, can the network grow indefinitely to maintain a high sink efficiency?

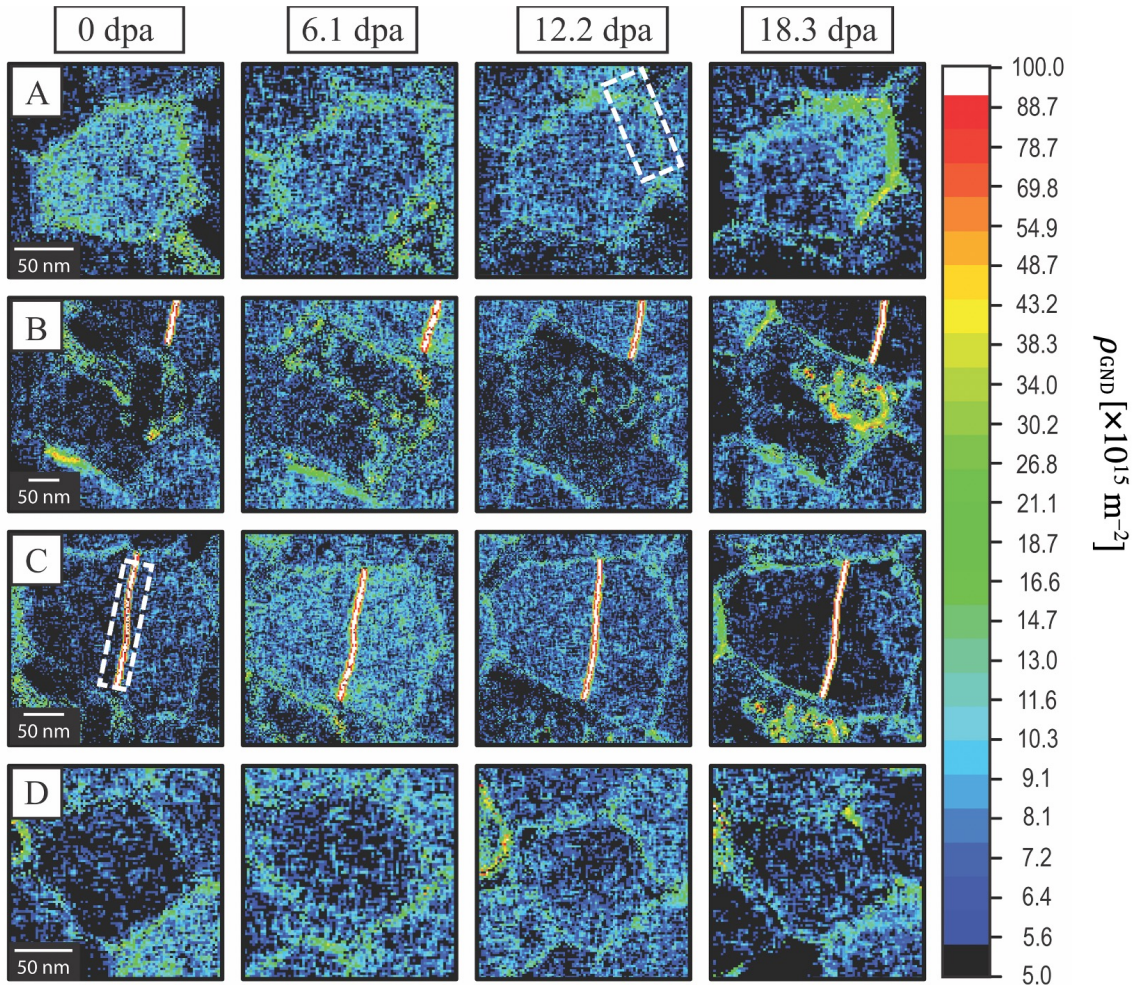


Figure 5.3: Nye dislocation tensor maps generated from PED ACOM orientation data, highlighting the increase of GND density at the GBs, as well as the evolution of Nye tensor signals, proposed to be dislocation networks, throughout differing nanocrystalline grain matrices (A-D) with the increase in He ion damage from 0.0 to 18.3 dpa. Fig. 5.3A is reproduced with permission from El-Atwani et al. [8].

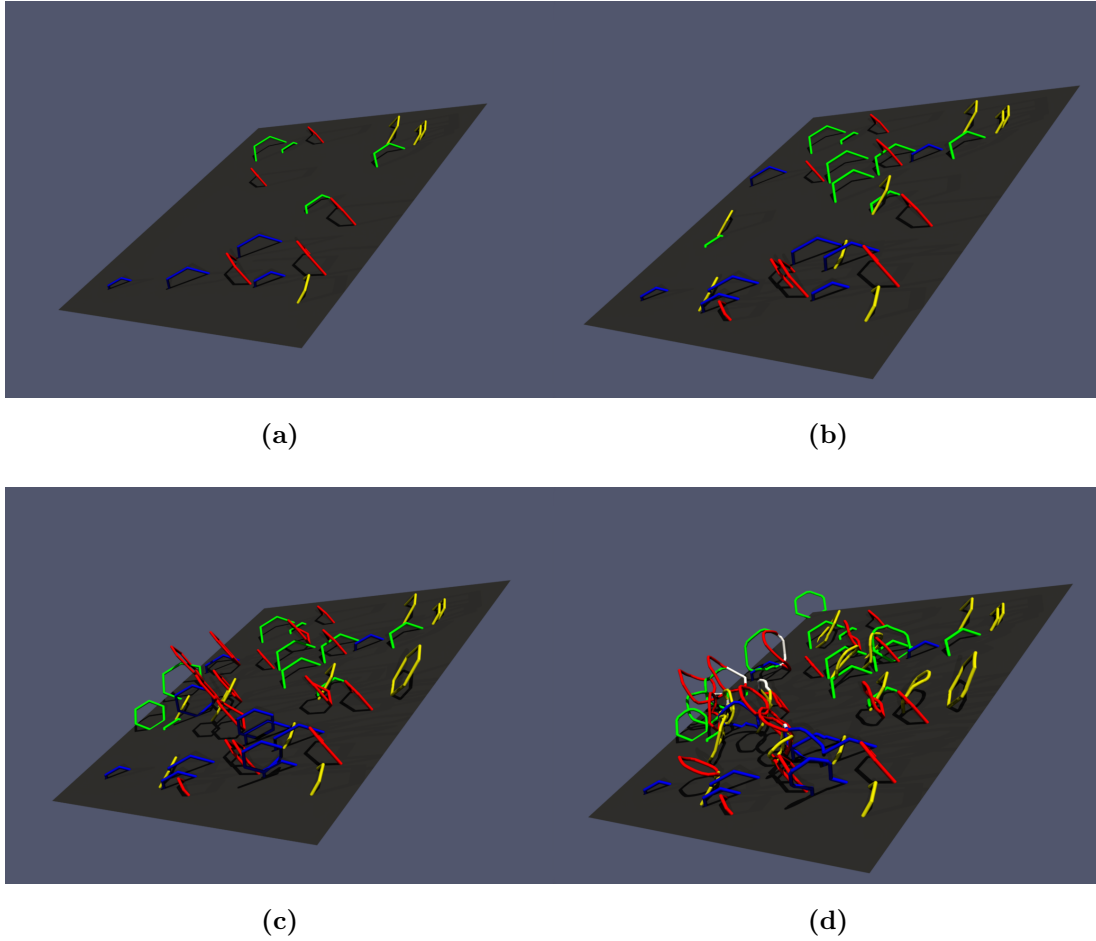


Figure 5.4: (a) Initial formation of partial loop substructures on a saturated GB. The loops are colored according to their Burgers vectors. (b) The GB is fully ‘blanketed’ by partial loops. (c) Snapshot showing the arrival of the first loop that does not reach the GB (interacting instead with the half-loops). (d) Final loop network after 1.0 dpa of irradiation. Color coding: ■ $\frac{1}{2}[11\bar{1}]$; ■ $\frac{1}{2}[\bar{1}11]$; ■ $\frac{1}{2}[1\bar{1}1]$; ■ $\frac{1}{2}[\bar{1}\bar{1}\bar{1}]$; white $\langle 100 \rangle$.

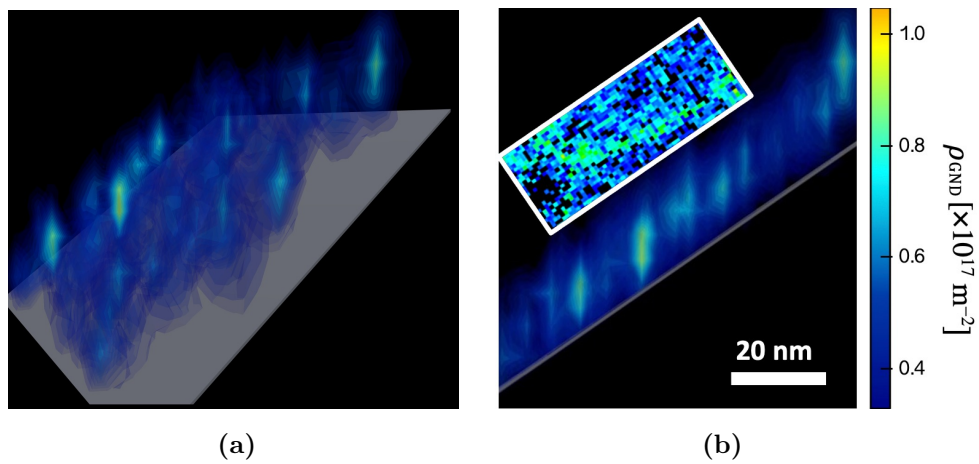


Figure 5.5: Rendition of the configuration shown in Fig. 5.3b processed as explained in Section 5.3.3. The left image is a side view (edge-on to the GB), while the one on the right is the same configuration tilted at an angle. The inset corresponds to the box highlighted in Fig. 5.3 (pane A). The color bar for the GND density is quantitatively equivalent in both cases.

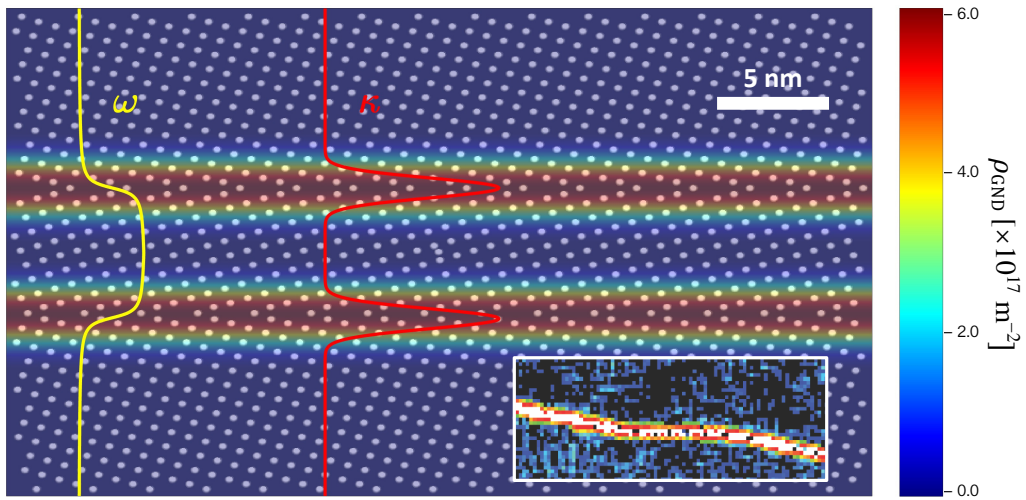


Figure 5.6: Calculated GND fingerprint of a twin plate bounded by two $\Sigma 3$ boundaries ($\approx 109^\circ$ -misorientation GB), showing the underlying atomistic structure seen along a $\langle 110 \rangle$ crystal direction. Superimposed on the image are the profiles for the lattice orientation ω and the lattice curvature κ profiles. The inset corresponds to the box highlighted in Fig. 5.3 (pane C).

REFERENCES

- [1] Vladimir P Zhdanov. Relaxation of a dislocation in a nanocrystallite. *Physics Letters A*, 2018.
- [2] A.C. Leff, C.R. Weinberger, and M.L. Taheri. Estimation of dislocation density from precession electron diffraction data using the nye tensor. *Ultramicroscopy*, 153:9–21, June 2015.
- [3] Sheng Yin, Yunxing Zuo, Anas Abu-Odeh, Hui Zheng, Xiang-Guo Li, Jun Ding, Shyue Ping Ong, Mark Asta, and Robert O Ritchie. Atomistic simulations of dislocation mobility in refractory high-entropy alloys and the effect of chemical short-range order. *Nature communications*, 12(1):1–14, 2021.
- [4] Xiang-Guo Li, Chi Chen, Hui Zheng, Yunxing Zuo, and Shyue Ping Ong. Complex strengthening mechanisms in the nbmotaw multi-principal element alloy. *npj Computational Materials*, 6(1):1–10, 2020.
- [5] Alexander Stukowski. Visualization and analysis of atomistic simulation data with ovito—the open visualization tool. *Modelling and Simulation in Materials Science and Engineering*, 18(1):015012, January 2010.
- [6] O.N. Senkov, G.B. Wilks, J.M. Scott, and D.B. Miracle. Mechanical properties of $\text{nb}_{25}\text{mo}_{25}\text{ta}_{25}\text{w}_{25}$ and $\text{v}_{20}\text{nb}_{20}\text{mo}_{20}\text{ta}_{20}\text{w}_{20}$ refractory high entropy alloys. *Intermetallics*, 19(5):698 – 706, 2011.
- [7] Oleg N. Senkov, Daniel B. Miracle, Kevin J. Chaput, and Jean-Philippe Couzinie. Development and exploration of refractory high entropy alloys? a review. *Journal of Materials Research*, 33(19):3092–3128, 2018.
- [8] El-Atwani Osman. Grain boundary metastability controls irradiation resistance in nanocrystalline metals.
- [9] Hossein Beladi, Qi Chao, and Gregory S Rohrer. Variant selection and inter-variant crystallographic planes distribution in martensite in a ti–6al–4v alloy. *Acta Materialia*, 80:478–489, 2014.
- [10] Cecile Marichal, Helena Van Swygenhoven, Steven Van Petegem, and Camelia Borca. $\{110\}$ slip with $\{112\}$ slip traces in bcc tungsten. *Scientific Reports*, 3(ARTICLE), 2013.

- [11] C R Weinberger, B L Boyce, and C C Battaile. Slip planes in bcc transition metals. *International Materials Reviews*, 58(5):296–314, 2013.
- [12] JL Bassani, K Ito, and V Vitek. Complex macroscopic plastic flow arising from non-planar dislocation core structures. *Materials Science and Engineering: A*, 319:97–101, 2001.
- [13] Di Kang, Derek Baars, Thomas Bieler, Chris Compton, Farhang Pourboghrat, and Aboozar Mapar. Study of slip and deformation in high purity single crystal nb for accelerator cavities. 2015.
- [14] Alfred Seeger and Uwe Holzwarth. Slip planes and kink properties of screw dislocations in high-purity niobium. *Philosophical Magazine*, 86(25-26):3861–3892, 2006.
- [15] O. Barrera, D. Bombac, Y. Chen, T. D. Daff, E. Galindo-Nava, P. Gong, D. Haley, R. Horton, I. Katzarov, J. R. Kermode, C. Liverani, M. Stopher, and F. Sweeney. Understanding and mitigating hydrogen embrittlement of steels: a review of experimental, modelling and design progress from atomistic to continuum. *Journal of Materials Science*, 53(9):6251–6290, May 2018.
- [16] David Rodney and Laurent Proville. Kink-pair nucleation on dislocations under stress in the two-dimensional frenkel-kontorova model. *Physical Review B*, 78(10):104115, 2008.
- [17] A Seeger. The flow stress of high-purity refractory body-centred cubic metals and its modification by atomic defects. *Le Journal de Physique IV*, 5(C7):C7–45, 1995.
- [18] Frank RN Nabarro and Mike S Duesbery. *Dislocations in solids*, volume 11. Elsevier, 2002.
- [19] Yue Zhao and Jaime Marian. Direct prediction of the solute softening-to-hardening transition in w–re alloys using stochastic simulations of screw dislocation motion. *Modelling and Simulation in Materials Science and Engineering*, 26(4):045002, 2018.
- [20] RJ Arsenault. The double-kink model for low-temperature deformation of bcc metals and solid solutions. *Acta Metallurgica*, 15(3):501–511, 1967.
- [21] Roger Chang. Screw dislocation core structure in body-centred cubic iron. *Philosophical Magazine*, 16(143):1021–1029, 1967.

- [22] Guofeng Wang, Alejandro Strachan, Tahir Çağın, and William A Goddard III. Atomistic simulations of kinks in $1/2 \langle 111 \rangle$ screw dislocations in bcc tantalum. *Physical Review B*, 68(22):224101, 2003.
- [23] Lucile Dezerald, David Rodney, Emmanuel Clouet, Lisa Ventelon, and Francois Willaime. Plastic anisotropy and dislocation trajectory in bcc metals. *Nature communications*, 7:11695, 2016.
- [24] R Gröger and V Vitek. Breakdown of the schmid law in bcc molybdenum related to the effect of shear stress perpendicular to the slip direction. In *Materials Science Forum*, volume 482, pages 123–126. Trans Tech Publ, 2005.
- [25] K Ito and V Vitek. Atomistic study of non-schmid effects in the plastic yielding of bcc metals. *Philosophical Magazine A*, 81(5):1387–1407, 2001.
- [26] M and-S Duesbery and V Vitek. Plastic anisotropy in bcc transition metals. *Acta Materialia*, 46(5):1481–1492, 1998.
- [27] A Seeger and W Wasserbäch. Anomalous slip—a feature of high-purity body-centred cubic metals. *physica status solidi (a)*, 189(1):27–50, 2002.
- [28] Peter R Morris and SL Semiatin. The prediction of plastic properties of polycrystalline aggregates of bcc metals deforming by $\langle 111 \rangle$ pencil glide. *Texture, Stress, and Microstructure*, 3(2):113–126, 1979.
- [29] C. Marichal, K. Srivastava, D. Weygand, S. Van Petegem, D. Grolimund, P. Gumbsch, and H. Van Swygenhoven. Origin of anomalous slip in tungsten. *Physical Review Letters*, 113(2), jul 2014.
- [30] H Matsui and H Kimura. Anomalous $\{110\}$ slip in high-purity molybdenum single crystals and its comparison with that in v (a) metals. *Materials Science and Engineering*, 24(2):247–256, 1976.
- [31] Alfred Seeger. Why anomalous slip in body-centred cubic metals? *Materials Science and Engineering: A*, 319:254–260, 2001.
- [32] J Eo Sinclair. Improved atomistic model of a bcc dislocation core. *Journal of Applied Physics*, 42(13):5321–5329, 1971.
- [33] JP Simmons, SI Rao, and DM Dimiduk. Atomistics simulations of structures and properties of $1/2 \langle 110 \rangle$ dislocations using three different embedded-atom method potentials fit to γ -tial. *Philosophical Magazine A*, 75(5):1299–1328, 1997.

- [34] Yun Tang and Min Ouyang. Tailoring properties and functionalities of metal nanoparticles through crystallinity engineering. *Nature materials*, 6(10):754, 2007.
- [35] M. R. Gilbert, P. Schuck, B. Sadigh, and J. Marian. Free energy generalization of the peierls potential in iron. *Phys. Rev. Lett.*, 111:095502, Aug 2013.
- [36] Christopher R. Weinberger, Garritt J. Tucker, and Stephen M. Foiles. Peierls potential of screw dislocations in bcc transition metals: Predictions from density functional theory. *Phys. Rev. B*, 87:054114, Feb 2013.
- [37] HB Huntington. Modification of the peierls-nabarro model for edge dislocation core. *Proceedings of the Physical Society. Section B*, 68(12):1043, 1955.
- [38] David Rodney and Laurent Proville. Stress-dependent peierls potential: Influence on kink-pair activation. *Physical Review B*, 79(9):094108, 2009.
- [39] Roger Chang and LJ Graham. Edge dislocation core structure and the peierls barrier in body-centered cubic iron. *physica status solidi (b)*, 18(1):99–103, 1966.
- [40] V Celli, M Kabler, T Ninomiya, and R Thomson. Theory of dislocation mobility in semiconductors. *Physical Review*, 131(1):58, 1963.
- [41] Pierre Guyot and John E Dorn. A critical review of the peierls mechanism. *Canadian Journal of Physics*, 45(2):983–1016, 1967.
- [42] Keiichi Edagawa, Takayoshi Suzuki, and Shin Takeuchi. Motion of a screw dislocation in a two-dimensional peierls potential. *Physical Review B*, 55(10):6180, 1997.
- [43] John E Dorn, J Mitchell, and F Hauser. Dislocation dynamics. *Experimental mechanics*, 5(11):353–362, 1965.
- [44] John P Hirth and Jens Lothe. *Theory of dislocations*. 1982.
- [45] H Koizumi, HOK Kirchner, and T Suzuki. Kink pair nucleation and critical shear stress. *Acta Metallurgica et Materialia*, 41(12):3483–3493, 1993.
- [46] Hirokazu Koizumi, Helmut OK Kirchner, and Takayoshi Suzuki. Nucleation of trapezoidal kink pairs on a peierls potential. *Philosophical Magazine A*, 69(4):805–820, 1994.

- [47] Laurent Proville, Lisa Ventelon, and David Rodney. Prediction of the kink-pair formation enthalpy on screw dislocations in α -iron by a line tension model parametrized on empirical potentials and first-principles calculations. *Physical Review B*, 87(14):144106, 2013.
- [48] Lisa Ventelon, F Willaime, and P Leyronnas. Atomistic simulation of single kinks of screw dislocations in α -fe. *Journal of Nuclear Materials*, 386:26–29, 2009.
- [49] Alexander Stukowski, David Cereceda, Thomas D Swinburne, and Jaime Marian. Thermally-activated non-schmid glide of screw dislocations in w using atomistically-informed kinetic monte carlo simulations. *International Journal of Plasticity*, 65:108–130, 2015.
- [50] TD Swinburne, SL Dudarev, SP Fitzgerald, MR Gilbert, and AP Sutton. Theory and simulation of the diffusion of kinks on dislocations in bcc metals. *Physical Review B*, 87(6):064108, 2013.
- [51] David Cereceda, Alexander Stukowski, MR Gilbert, Sylvain Queyreau, Lisa Ventelon, Mihai-Cosmin Marinica, JM Perlado, and Jaime Marian. Assessment of interatomic potentials for atomistic analysis of static and dynamic properties of screw dislocations in w. *Journal of Physics: Condensed Matter*, 25(8):085702, 2013.
- [52] Mihai-Cosmin Marinica, Lisa Ventelon, MR Gilbert, L Proville, SL Dudarev, J Marian, G Bencteux, and F Willaime. Interatomic potentials for modelling radiation defects and dislocations in tungsten. *Journal of Physics: Condensed Matter*, 25(39):395502, 2013.
- [53] Hyoungki Park, Michael R Fellingner, Thomas J Lenosky, William W Tipton, Dallas R Trinkle, Sven P Rudin, Christopher Woodward, John W Wilkins, and Richard G Hennig. Ab initio based empirical potential used to study the mechanical properties of molybdenum. *Physical Review B*, 85(21):214121, 2012.
- [54] G. Henkelman, G. Jóhannesson, and H Jonsson. *Methods for Finding Saddle Points and Minimum Energy Paths*. Kluwer Academic Publishers, 2000.
- [55] S. Plimpton. Fast parallel algorithms for short-range molecular-dynamics. <http://lammps.sandia.gov>. *Journal Of Computational Physics*, 117(1):1–19, Mar 1 1995.

- [56] TA Arias and JD Joannopoulos. Ab initio theory of dislocation interactions: From close-range spontaneous annihilation to the long-range continuum limit. *Physical review letters*, 73(5):680, 1994.
- [57] Wei Cai, Vasily V Bulatov, Jinpeng Chang, Ju Li, and Sidney Yip. Anisotropic elastic interactions of a periodic dislocation array. *Physical Review Letters*, 86(25):5727, 2001.
- [58] Wei Cai, Vasily V Bulatov, Jinpeng Chang, Ju Li, and Sidney Yip. Periodic image effects in dislocation modelling. *Philosophical Magazine*, 83(5):539–567, 2003.
- [59] MZ Hossain and Jaime Marian. Stress-dependent solute energetics in w-re alloys from first-principles calculations. *Acta Materialia*, 80:107–117, 2014.
- [60] Keonwook Kang, Vasily V. Bulatov, and Wei Cai. Singular orientations and faceted motion of dislocations in body-centered cubic crystals. *Proceedings of the National Academy of Sciences*, 109(38):15174–15178, 2012.
- [61] Wei Cai, Athanasios Arsenlis, Christopher R Weinberger, and Vasily V Bulatov. A non-singular continuum theory of dislocations. *Journal of the Mechanics and Physics of Solids*, 54(3):561–587, 2006.
- [62] Christopher R Weinberger, Garritt J Tucker, and Stephen M Foiles. Peierls potential of screw dislocations in bcc transition metals: Predictions from density functional theory. *Physical Review B*, 87(5):054114, 2013.
- [63] L Dezerald, Lisa Ventelon, E Clouet, C Denoual, D Rodney, and F Willaime. Ab initio modeling of the two-dimensional energy landscape of screw dislocations in bcc transition metals. *Physical Review B*, 89(2):024104, 2014.
- [64] L Dezerald, L Proville, Lisa Ventelon, F Willaime, and D Rodney. First-principles prediction of kink-pair activation enthalpy on screw dislocations in bcc transition metals: V, nb, ta, mo, w, and fe. *Physical Review B*, 91(9):094105, 2015.
- [65] AD Brailsford. Effective line tension of a dislocation. *Physical Review*, 139(6A):A1813, 1965.
- [66] Daniel Caillard and Jean-Luc Martin. *Thermally activated mechanisms in crystal plasticity*, volume 8. Elsevier, 2003.

- [67] Laurent Proville, Lisa Ventelon, and David Rodney. Prediction of the kink-pair formation enthalpy on screw dislocations in α -iron by a line tension model parametrized on empirical potentials and first-principles calculations. *Phys. Rev. B*, 87:144106, Apr 2013.
- [68] Xiaowang W Zhou, Ryan B Sills, Donald K Ward, and Richard A Karnesky. Atomistic calculations of dislocation core energy in aluminium. *Physical Review B*, 95(5):054112, 2017.
- [69] William H Press, Brian P Flannery, Saul A Teukolsky, and William T Vetterling. Numerical recipes. *Cambridge University Press*, 78:134, 1990.
- [70] SP Fitzgerald. Kink pair production and dislocation motion. *Scientific reports*, 6:39708, 2016.
- [71] David Cereceda, Martin Diehl, Franz Roters, Dierk Raabe, J Manuel Perlado, and Jaime Marian. Unraveling the temperature dependence of the yield strength in single-crystal tungsten using atomistically-informed crystal plasticity calculations. *International Journal of Plasticity*, 78:242–265, 2016.
- [72] U. Kocks, A. Argon, and M. Ashby. 1. introduction. *Progress in Materials Science*, 19, 1975. cited By 69.
- [73] CA Sawyer, JW Morris Jr, and DC Chrzan. Dislocation core radii near elastic stability limits. *Physical Review B*, 87(13):134106, 2013.
- [74] Sambit Das and Vikram Gavini. Electronic structure study of screw dislocation core energetics in aluminum and core energetics informed forces in a dislocation aggregate. *Journal of the Mechanics and Physics of Solids*, 104:115–143, 2017.
- [75] Pierre-Antoine Geslin and David Rodney. Thermal fluctuations of dislocations reveal the interplay between their core energy and long-range elasticity. *Physical Review B*, 98(17):174115, 2018.
- [76] Z. Yao, M.L. Jenkins, M. Hernández-Mayoral, and M.A. Kirk. The temperature dependence of heavy-ion damage in iron: A microstructural transition at elevated temperatures. *Philosophical Magazine*, 90(35-36):4623–4634, December 2010.
- [77] Yu N Osetsky, A Serra, and V Priego. Interactions between mobile dislocation loops in cu and a-fe. *Journal of Nuclear Materials*, page 11, 2000.

- [78] M. Hernández-Mayoral, Z. Yao, M.L. Jenkins, and M.A. Kirk. Heavy-ion irradiations of fe and fe–cr model alloys part 2: Damage evolution in thin-foils at higher doses. *Philosophical Magazine*, 88(21):2881–2897, July 2008.
- [79] Z. Yao, M. Hernández-Mayoral, M.L. Jenkins, and M.A. Kirk. Heavy-ion irradiations of fe and fe–cr model alloys part 1: Damage evolution in thin-foils at lower doses. *Philosophical Magazine*, 88(21):2851–2880, July 2008.
- [80] Z. Rong, V. Mohles, D.J. Bacon *, and Yu. N. Osetsky. Dislocation dynamics modelling of dislocation–loop interactions in irradiated metals. *Philosophical Magazine*, 85(2-3):171–188, January 2005.
- [81] I.J. Beyerlein, M.J. Demkowicz, A. Misra, and B.P. Uberuaga. Defect-interface interactions. *Progress in Materials Science*, 74:125–210, October 2015.
- [82] W. Streit Cunningham, Jonathan M. Gentile, Osman El-Atwani, Chase N. Taylor, Mert Efe, Stuart A. Maloy, and Jason R. Trelewicz. Softening due to grain boundary cavity formation and its competition with hardening in helium implanted nanocrystalline tungsten. *Scientific Reports*, 8(1):2897, December 2018.
- [83] T.S Byun and K Farrell. Irradiation hardening behavior of polycrystalline metals after low temperature irradiation. *Journal of Nuclear Materials*, 326(2-3):86–96, March 2004.
- [84] Xunxiang Hu, Takaaki Koyanagi, Makoto Fukuda, N.A.P. Kiran Kumar, Lance L. Snead, Brian D. Wirth, and Yutai Katoh. Irradiation hardening of pure tungsten exposed to neutron irradiation. *Journal of Nuclear Materials*, 480:235–243, November 2016.
- [85] M. Matijasevic and A. Almazouzi. Effect of cr on the mechanical properties and microstructure of fe–cr model alloys after n-irradiation. *Journal of Nuclear Materials*, 377(1):147–154, June 2008.
- [86] M.D. McMurtrey, G.S. Was, B. Cui, I. Robertson, L. Smith, and D. Farkas. Strain localization at dislocation channel–grain boundary intersections in irradiated stainless steel. *International Journal of Plasticity*, 56:219–231, May 2014.
- [87] M. A. Tschopp, K. N. Solanki, F. Gao, X. Sun, M. A. Khaleel, and M. F. Horstemeyer. Probing grain boundary sink strength at the nanoscale: Energet-

ics and length scales of vacancy and interstitial absorption by grain boundaries in α -Fe. *Physical Review B*, 85(6):064108, February 2012.

- [88] O. El-Atwani, J. E. Nathaniel, A. C. Leff, K. Hattar, and M. L. Taheri. Direct observation of sink-dependent defect evolution in nanocrystalline iron under irradiation. *Scientific Reports*, 7(1):1836, December 2017.
- [89] W.Z. Han, M.J. Demkowicz, E.G. Fu, Y.Q. Wang, and A. Misra. Effect of grain boundary character on sink efficiency. *Acta Materialia*, 60(18):6341–6351, October 2012.
- [90] Xinghang Zhang, Khalid Hattar, Youxing Chen, Lin Shao, Jin Li, Cheng Sun, Kaiyuan Yu, Nan Li, Mitra L. Taheri, Haiyan Wang, Jian Wang, and Michael Nastasi. Radiation damage in nanostructured materials. *Progress in Materials Science*, 96:217–321, July 2018.
- [91] N Nita, R Schaeublin, and M Victoria. Impact of irradiation on the microstructure of nanocrystalline materials. *Journal of Nuclear Materials*, 329-333:953–957, August 2004.
- [92] C. Sun, M. Song, K. Y. Yu, Y. Chen, M. Kirk, M. Li, H. Wang, and X. Zhang. In situ evidence of defect cluster absorption by grain boundaries in Kr ion irradiated nanocrystalline Ni. *Metallurgical and Materials Transactions A*, 44(4):1966–1974, April 2013.
- [93] Jiake Wei, Bin Feng, Ryo Ishikawa, Tatsuya Yokoi, Katsuyuki Matsunaga, Naoya Shibata, and Yuichi Ikuhara. Direct imaging of atomistic grain boundary migration. *Nature Materials*, 20(7):951–955, July 2021.
- [94] Timofey Frolov, David L. Olmsted, Mark Asta, and Yuri Mishin. Structural phase transformations in metallic grain boundaries. *Nature Communications*, 4(1):1899, October 2013.
- [95] Jian Han, Vaclav Vitek, and David J. Srolovitz. Grain-boundary metastability and its statistical properties. *Acta Materialia*, 104:259–273, February 2016.
- [96] O. El-Atwani, J. E. Nathaniel, A. C. Leff, J. K. Baldwin, K. Hattar, and M. L. Taheri. Evidence of a temperature transition for denuded zone formation in nanocrystalline Fe under He irradiation. *Materials Research Letters*, 5(3):195–200, May 2017.

- [97] Blas Pedro Uberuaga, Louis J. Vernon, Enrique Martinez, and Arthur F. Voter. The relationship between grain boundary structure, defect mobility and grain boundary sink efficiency. *Scientific Reports*, 5(1):9095, August 2015.
- [98] James E. Nathaniel, Gregory A. Vetterick, Osman El-Atwani, Asher Leff, Jon Kevin Baldwin, Pete Baldo, Marquis A. Kirk, Khalid Hattar, and Mitra L. Taheri. The influence of solute on irradiation damage evolution in nanocrystalline thin-films. *Journal of Nuclear Materials*, 543:152616, January 2021.
- [99] Yipeng Li, Li Wang, Guang Ran, Yue Yuan, Lu Wu, Xinyi Liu, Xi Qiu, Zhipeng Sun, Yifan Ding, Qing Han, Xiaoyong Wu, Huiqiu Deng, and Xiuyin Huang. In-situ TEM investigation of 30 keV he+ irradiated tungsten: Effects of temperature, fluence, and sample thickness on dislocation loop evolution. *Acta Materialia*, 206:116618, March 2021.
- [100] Chang-Yu Hung, Tomotsugu Shimokawa, Yu Bai, Nobuhiro Tsuji, and Mitsuhiro Murayama. Investigating the dislocation reactions on $3\{111\}$ twin boundary during deformation twin nucleation process in an ultrafine-grained high-manganese steel. *Scientific Reports*, 11(1):19298, December 2021.
- [101] S. Sun, B. L. Adams, and W. E. King. Observations of lattice curvature near the interface of a deformed aluminium bicrystal. *Philosophical Magazine A*, 80(1):9–25, January 2000.
- [102] John F Nye. Some geometrical relations in dislocated crystals. *Acta metallurgica*, 1(2):153–162, 1953.
- [103] N. Soneda and T. Diaz de la Rubia. Defect production, annealing kinetics and damage evolution in -fe: An atomic-scale computer simulation. *Philosophical Magazine A*, 78(5):995–1019, November 1998.
- [104] H. Trinkaus, B.N. Singh, and A.J.E. Foreman. Glide of interstitial loops produced under cascade damage conditions: Possible effects on void formation. *Journal of Nuclear Materials*, 199(1):1–5, December 1992.
- [105] S.I Golubov, B.N Singh, and H Trinkaus. Defect accumulation in fcc and bcc metals and alloys under cascade damage conditions – towards a generalisation of the production bias model. *Journal of Nuclear Materials*, 276(1-3):78–89, January 2000.

- [106] B. D. Wirth, V. V. Bulatov, and T. Diaz de la Rubia. Dislocation-Stacking Fault Tetrahedron Interactions in Cu. *Journal of Engineering Materials and Technology*, 124(3):329–334, July 2002.
- [107] R. Schäublin, Z. Yao, N. Baluc, and M. Victoria. Irradiation-induced stacking fault tetrahedra in fcc metals. *Philosophical Magazine*, 85(4-7):769–777, February 2005.
- [108] A Fellman, A E Sand, J Byggmästar, and K Nordlund. Radiation damage in tungsten from cascade overlap with voids and vacancy clusters. *Journal of Physics: Condensed Matter*, 31(40):405402, October 2019.
- [109] T. C. Lee, I. M. Robertson, and H. K. Birnbaum. An In Situ transmission electron microscope deformation study of the slip transfer mechanisms in metals. *Metallurgical Transactions A*, 21(9):2437–2447, September 1990.
- [110] Josh Kacher, B.P. Eftink, B. Cui, and I.M. Robertson. Dislocation interactions with grain boundaries. *Current Opinion in Solid State and Materials Science*, 18(4):227–243, August 2014.
- [111] T. C. Lee, I. M. Robertson, and H. K. Birnbaum. TEM *in situ* deformation study of the interaction of lattice dislocations with grain boundaries in metals. *Philosophical Magazine A*, 62(1):131–153, July 1990.
- [112] Josh Kacher and I.M. Robertson. Quasi-four-dimensional analysis of dislocation interactions with grain boundaries in 304 stainless steel. *Acta Materialia*, 60(19):6657–6672, November 2012.
- [113] J. Chen, K. Dang, H.T. Vo, P. Hosemann, and S.J. Fensin. Associating GB characteristics with its sink efficiency in absorbing Frank loops in Cu. *Scripta Materialia*, 192:61–66, February 2021.
- [114] Devin W. Adams, David T. Fullwood, Robert H. Wagoner, and Eric R. Homer. Atomistic survey of grain boundary-dislocation interactions in FCC nickel. *Computational Materials Science*, 164:171–185, June 2019.
- [115] M de Koning, R.J Kurtz, V.V Bulatov, C.H Henager, R.G Hoagland, W Cai, and M Nomura. Modeling of dislocation–grain boundary interactions in FCC metals. *Journal of Nuclear Materials*, 323(2-3):281–289, December 2003.

- [116] N. Gao, D. Perez, G.H. Lu, and Z.G. Wang. Molecular dynamics study of the interaction between nanoscale interstitial dislocation loops and grain boundaries in BCC iron. *Journal of Nuclear Materials*, 498:378–386, January 2018.
- [117] Gregory A Vetterick, Jacob Gruber, Pranav K Suri, J. K. Baldwin, Marquis A. Kirk, Pete Baldo, Yong Q. Wang, Amit Misra, Garritt J. Tucker, and M. L. Taheri. Achieving Radiation Tolerance through Non-Equilibrium Grain Boundary Structures. *Scientific Reports*, 7, 2017.
- [118] G. Vetterick, J. K. Baldwin, A. Misra, and M. L. Taheri. Texture evolution in nanocrystalline iron films deposited using biased magnetron sputtering. *Journal of Applied Physics*, 116(23):233503, December 2014. Publisher: American Institute of Physics.
- [119] G. Vetterick, C-Y. Hung, E. Hopkins, J.K. Balwin, P. Baldo, M.A. Kirk, A. Misra, S. He, J. Marian, and M.L. Taheri. Temperature effects on the radiation damage morphology in nanocrystalline iron. *Scripta Materialia*, 213:114607, May 2022.
- [120] James E. Nathaniel, Andrew C. Lang, Osman El-Atwani, Pranav K. Suri, Jon K. Baldwin, Marquis A. Kirk, Yongqiang Wang, and Mitra L. Taheri. Toward high-throughput defect density quantification: A comparison of techniques for irradiated samples. *Ultramicroscopy*, 206:112820, November 2019.
- [121] B.S El-Dasher, B.L Adams, and A.D Rollett. Viewpoint: experimental recovery of geometrically necessary dislocation density in polycrystals. *Scripta Materialia*, 48(2):141–145, January 2003.
- [122] T.J. Ruggles and D.T. Fullwood. Estimations of bulk geometrically necessary dislocation density using high resolution ebsd. *Ultramicroscopy*, 133:8–15, October 2013.
- [123] N.A Fleck, M.F Ashby, and J.W Hutchinson. The role of geometrically necessary dislocations in giving material strengthening. *Scripta Materialia*, 48(2):179–183, January 2003.
- [124] Huajian Gao and Yonggang Huang. Geometrically necessary dislocation and size-dependent plasticity. *Scripta Materialia*, 48(2):113–118, January 2003.
- [125] Athanasios Arsenlis and David M Parks. Modeling the evolution of crystallographic dislocation density in crystal plasticity. *Journal of the Mechanics and Physics of Solids*, 50(9):1979–2009, 2002.

- [126] Suchandrima Das, Felix Hofmann, and Edmund Tarleton. Consistent determination of geometrically necessary dislocation density from simulations and experiments. *International Journal of Plasticity*, 109:18–42, October 2018.
- [127] Jian Han, Spencer L. Thomas, and David J. Srolovitz. Grain-boundary kinetics: A unified approach. *Progress in Materials Science*, 98:386–476, October 2018.
- [128] S Chiesa, P M Derlet, S L Dudarev, and H Van Swygenhoven. Optimization of the magnetic potential for -fe. *Journal of Physics: Condensed Matter*, 23(20):206001, May 2011.
- [129] Alexander Stukowski, Vasily V Bulatov, and Athanasios Arsenlis. Automated identification and indexing of dislocations in crystal interfaces. *Modelling and Simulation in Materials Science and Engineering*, 20(8):085007, December 2012.
- [130] Hyongju Park. Polytope bounded voronoi diagram in 2d and 3d. <https://github.com/hyongju/Polytope-bounded-Voronoi-diagram>, 2020.
- [131] J Han, V Vitek, and D J Srolovitz. The interplay between grain boundary structure and defect sink/annealing behavior. *IOP Conference Series: Materials Science and Engineering*, 89:012004, August 2015.
- [132] John Frederick Nye et al. *Physical properties of crystals: their representation by tensors and matrices*. Oxford university press, 1985.
- [133] Samuel Forest, Rainer Sievert, and Elias C Aifantis. Strain gradient crystal plasticity: thermomechanical formulations and applications. *Journal of the mechanical behavior of materials*, 13(3-4):219–232, 2002.
- [134] Samuel Forest and Karam Sab. Stress gradient continuum theory. *Mechanics Research Communications*, 40:16–25, 2012.
- [135] Fabio Sozio and Arash Yavari. On nye’s lattice curvature tensor. *Mechanics Research Communications*, 113:103696, 2021.
- [136] J. Schröder and K. Hackl. *Plasticity and Beyond: Microstructures, Crystal-Plasticity and Phase Transitions*. Springer, 2014.
- [137] B. Cantor, I.T.H. Chang, P. Knight, and A.J.B. Vincent. Microstructural development in equiatomic multicomponent alloys. *Materials Science and Engineering: A*, 375-377:213 – 218, 2004.

- [138] J.-W. Yeh, S.-K. Chen, S.-J. Lin, J.-Y. Gan, T.-S. Chin, T.-T. Shun, C.-H. Tsau, and S.-Y. Chang. Nanostructured high-entropy alloys with multiple principal elements: Novel alloy design concepts and outcomes. *Advanced Engineering Materials*, 6(5):299–303.
- [139] Li Sheng Zhang, Guo Liang Ma, Li Chao Fu, and Jing Yi Tian. Recent progress in high-entropy alloys. In *Materials Engineering for Advanced Technologies (ICMEAT 2012)*, volume 631 of *Advanced Materials Research*, pages 227–232. Trans Tech Publications Ltd, 3 2013.
- [140] Jien Wei Yeh, Yu Liang Chen, Su Jien Lin, and Swe Kai Chen. High-entropy alloys ? a new era of exploitation. In *Advanced Structural Materials III*, volume 560 of *Materials Science Forum*, pages 1–9. Trans Tech Publications Ltd, 11 2007.
- [141] E. J. Pickering and N. G. Jones. High-entropy alloys: a critical assessment of their founding principles and future prospects. *International Materials Reviews*, 61(3):183–202, 2016.
- [142] Michael C. Gao, Jien-Wei Yeh, Peter K. Liaw, and Yong Zhang. *High-Entropy Alloys*. Springer, Cham, 2016.
- [143] D.B. Miracle and O.N. Senkov. A critical review of high entropy alloys and related concepts. *Acta Materialia*, 122:448 – 511, 2017.
- [144] Ming-Hung Tsai and Jien-Wei Yeh. High-entropy alloys: A critical review. *Materials Research Letters*, 2(3):107–123, 2014.
- [145] Michael C. Gao and Junwei Qiao. High-entropy alloys (heas). *Metals*, 8(2), 2018.
- [146] Bernd Gludovatz, Anton Hohenwarter, Dhiraj Catoor, Edwin H. Chang, Easo P. George, and Robert O. Ritchie. A fracture-resistant high-entropy alloy for cryogenic applications. *Science*, 345(6201):1153–1158, 2014.
- [147] Song-qin Xia, WANG Zhen, Teng-fei Yang, and Yong Zhang. Irradiation behavior in high entropy alloys. *Journal of Iron and Steel Research, International*, 22(10):879–884, 2015.
- [148] Songqin Xia, Michael C Gao, Tengfei Yang, Peter K Liaw, and Yong Zhang. Phase stability and microstructures of high entropy alloys ion irradiated to high doses. *Journal of Nuclear Materials*, 480:100–108, 2016.

- [149] NAP Kiran Kumar, C Li, KJ Leonard, H Bei, and SJ Zinkle. Microstructural stability and mechanical behavior of feni-mncr high entropy alloy under ion irradiation. *Acta Materialia*, 113:230–244, 2016.
- [150] T Egami, W Guo, PD Rack, and T Nagase. Irradiation resistance of multi-component alloys. *Metallurgical and Materials Transactions A*, 45(1):180–183, 2014.
- [151] Roksolana Kozak, Alla Sologubenko, and Walter Steurer. Single-phase high-entropy alloys: an overview. *Zeitschrift für Kristallographie - Crystalline Materials*, 230(1):55 – 68, 2015.
- [152] *High-Entropy Alloys: Formation and Properties*, volume ASME 2018 Symposium on Elevated Temperature Application of Materials for Fossil, Nuclear, and Petrochemical Industries of *Pressure Technology*, 04 2018. V001T01A004.
- [153] ON Senkov, JD Miller, DB Miracle, and C Woodward. Accelerated exploration of multi-principal element alloys for structural applications. *Calphad*, 50:32–48, 2015.
- [154] Daniel B. Miracle, Jonathan D. Miller, Oleg N. Senkov, Christopher Woodward, Michael D. Uchic, and Jaimie Tiley. Exploration and development of high entropy alloys for structural applications. *Entropy*, 16(1):494–525, 2014.
- [155] Yong Zhang, Ting Ting Zuo, Zhi Tang, Michael C. Gao, Karin A. Dahmen, Peter K. Liaw, and Zhao Ping Lu. Microstructures and properties of high-entropy alloys. *Progress in Materials Science*, 61:1–93, April 2014.
- [156] Yu Zou, Soumyadipta Maiti, Walter Steurer, and Ralph Spolenak. Size-dependent plasticity in an nb₂₅mo₂₅ta₂₅w₂₅ refractory high-entropy alloy. *Acta Materialia*, 65:85 – 97, 2014.
- [157] Hongwei Yao, Jun-Wei Qiao, Michael C. Gao, Jeffrey A. Hawk, Sheng-Guo Ma, and Hefeng Zhou. Monobinary medium-entropy alloy. *Entropy*, 18(5), 2016.
- [158] Fritz Körmann and Marcel H.F. Sluiter. Interplay between lattice distortions, vibrations and phase stability in nbmotaw high entropy alloys. *Entropy*, 18(8), 2016.
- [159] H.W. Yao, J.W. Qiao, J.A. Hawk, H.F. Zhou, M.W. Chen, and M.C. Gao. Mechanical properties of refractory high-entropy alloys: Experiments and modeling. *Journal of Alloys and Compounds*, 696:1139 – 1150, 2017.

- [160] Henrik Dobbstein, Magnus Thiele, Evgeny L. Gurevich, Easo P. George, and Andreas Ostendorf. Direct metal deposition of refractory high entropy alloy monobutaw. *Physics Procedia*, 83:624 – 633, 2016. Laser Assisted Net Shape Engineering 9 International Conference on Photonic Technologies Proceedings of the LANE 2016 September 19-22, 2016 Fürth, Germany.
- [161] Sebastian Alexander Kube, Sungwoo Sohn, David Uhl, Amit Datye, Apurva Mehta, and Jan Schroers. Phase selection motifs in high entropy alloys revealed through combinatorial methods: Large atomic size difference favors bcc over fcc. *Acta Materialia*, 166:677 – 686, 2019.
- [162] Shou-Yi Chang, Chen-En Li, Yi-Chung Huang, Hsun-Feng Hsu, Jien-Wei Yeh, and Su-Jien Lin. Structural and thermodynamic factors of suppressed interdiffusion kinetics in multi-component high-entropy materials. *Scientific Reports*, 4(1):4162, 2014.
- [163] D. Beke and G. Erdaglyi. On the diffusion in high-entropy alloys. *Materials Letters*, 164, 09 2015.
- [164] Shijun Zhao, Yuri Osetsky, and Yanwen Zhang. Preferential diffusion in concentrated solid solution alloys: NiFe, NiCo and NiCoCr. *Acta Materialia*, 128:391–399, 2017.
- [165] Ankit Roy, Joydeep Munshi, and Ganesh Balasubramanian. Low energy atomic traps sluggish the diffusion in compositionally complex refractory alloys. *Intermetallics*, 131:107106, 2021.
- [166] V. Soni, O. N. Senkov, B. Gwalani, D. B. Miracle, and R. Banerjee. Microstructural design for improving ductility of an initially brittle refractory high entropy alloy. *Scientific Reports*, 8(1):8816, 2018.
- [167] Jien-Wei Yeh and Su-Jien Lin. Breakthrough applications of high-entropy materials. *Journal of Materials Research*, 33(19):3129–3137, 2018.
- [168] J-Ph Couzinié, L Lilensten, Y Champion, G Dirras, L Perrière, and I Guillot. On the room temperature deformation mechanisms of a TiZrHfNbTa refractory high-entropy alloy. *Materials Science and Engineering: A*, 645:255–263, 2015.
- [169] J-P Couzinié and G Dirras. Body-centered cubic high-entropy alloys: From processing to underlying deformation mechanisms. *Materials Characterization*, 147:533–544, 2019.

- [170] Yeqiang Bu, Yuan Wu, Zhifeng Lei, Xiaoyuan Yuan, Honghui Wu, Xiaobin Feng, Jiabin Liu, Jun Ding, Yang Lu, Hongtao Wang, et al. Local chemical fluctuation mediated ductility in body-centered-cubic high-entropy alloys. *Materials Today*, 46:28–34, 2021.
- [171] Bing Chen, Suzhi Li, Hongxiang Zong, Xiangdong Ding, Jun Sun, and Evan Ma. Unusual activated processes controlling dislocation motion in body-centered-cubic high-entropy alloys. *Proceedings of the National Academy of Sciences*, 117(28):16199–16206, 2020.
- [172] Chanhoo Lee, Francesco Maresca, Rui Feng, Yi Chou, T Ungar, Michael Widom, Ke An, Jonathan D Poplawsky, Yi-Chia Chou, Peter K Liaw, et al. Strength can be controlled by edge dislocations in refractory high-entropy alloys. *Nature communications*, 12(1):1–8, 2021.
- [173] Chanhoo Lee, George Kim, Yi Chou, Brianna L Musicó, Michael C Gao, Ke An, Gian Song, Yi-Chia Chou, Veerle Keppens, Wei Chen, et al. Temperature dependence of elastic and plastic deformation behavior of a refractory high-entropy alloy. *Science Advances*, 6(37):eaaz4748, 2020.
- [174] SI Rao, C Varvenne, C Woodward, TA Parthasarathy, D Miracle, ON Senkov, and WA Curtin. Atomistic simulations of dislocations in a model bcc multicomponent concentrated solid solution alloy. *Acta Materialia*, 125:311–320, 2017.
- [175] Evan Ma. Unusual dislocation behavior in high-entropy alloys. *Scripta Materialia*, 181:127–133, 2020.
- [176] Cláudio Geraldo Schön. On short-range order strengthening and its role in high-entropy alloys. *Scripta Materialia*, 196:113754, 2021.
- [177] Yixi Shen and Douglas E Spearot. Mobility of dislocations in fcc high entropy alloys. *Modelling and Simulation in Materials Science and Engineering*, 29(8):085017, 2021.
- [178] Zhijun Wang, CT Liu, and Peng Dou. Thermodynamics of vacancies and clusters in high-entropy alloys. *Physical Review Materials*, 1(4):043601, 2017.
- [179] Qingqing Ding, Yin Zhang, Xiao Chen, Xiaoqian Fu, Dengke Chen, Sijing Chen, Lin Gu, Fei Wei, Hongbin Bei, Yanfei Gao, et al. Tuning element distribution, structure and properties by composition in high-entropy alloys. *Nature*, 574(7777):223–227, 2019.

- [180] Shijun Zhao. Role of chemical disorder and local ordering on defect evolution in high-entropy alloys. *Phys. Rev. Materials*, 5:103604, Oct 2021.
- [181] J. Byggmästar, K. Nordlund, and F. Djurabekova. Modeling refractory high-entropy alloys with efficient machine-learned interatomic potentials: Defects and segregation. *Phys. Rev. B*, 104:104101, Sep 2021.
- [182] Ankit Roy, Prashant Singh, Ganesh Balasubramanian, and Duane D Johnson. Vacancy formation energies and migration barriers in multi-principal element alloys. *Acta Materialia*, page 117611, 2022.
- [183] Mukul Kabir, Timothy T Lau, David Rodney, Sidney Yip, and Krystyn J Van Vliet. Predicting dislocation climb and creep from explicit atomistic details. *Physical review letters*, 105(9):095501, 2010.
- [184] M.Z. Hossain and Jaime Marian. Stress-dependent solute energetics in γ -tial alloys from first-principles calculations. *Acta Materialia*, 80:107 – 117, 2014.
- [185] Michael Zehetbauer. Effects of non-equilibrium vacancies on strengthening. In *Key Engineering Materials*, volume 97, pages 287–306. Trans Tech Publ, 1994.
- [186] François Louchet and Bernard Viguier. Ordinary dislocations in γ -tial: cusp unzipping, jog dragging and stress anomaly. *Philosophical Magazine A*, 80(4):765–779, 2000.
- [187] SI Rao, C Woodward, B Akdim, ON Senkov, and D Miracle. Theory of solid solution strengthening of bcc chemically complex alloys. *Acta Materialia*, 209:116758, 2021.
- [188] Qiang Feng and Sung H Whang. Cross-slip and glide behavior of ordinary dislocations in single crystal γ -ti-56al. *Intermetallics*, 7(9):971–979, 1999.
- [189] Xinran Zhou, Sicong He, and Jaime Marian. Cross-kinks control screw dislocation strength in equiatomic bcc refractory alloys. *Acta Materialia*, 211:116875, 2021.
- [190] Xinran Zhou and Jaime Marian. Temperature and stress dependence of screw dislocation mobility in nb-v-ta alloys using kinetic monte carlo simulations. *Frontiers in Materials*, 8, 2021.
- [191] Ziqing Zhou, Yeju Zhou, Quanfeng He, Zhaoyi Ding, Fucheng Li, and Yong Yang. Machine learning guided appraisal and exploration of phase design for high entropy alloys. *npj Computational Materials*, 5(1):1–9, 2019.

- [192] JM Rickman, G Balasubramanian, CJ Marvel, HM Chan, and M-T Burton. Machine learning strategies for high-entropy alloys. *Journal of Applied Physics*, 128(22):221101, 2020.
- [193] Fritz Körmann, Andrei V. Ruban, and Marcel H.F. Sluiter. Long-ranged interactions in bcc nbmotaw high-entropy alloys. *Materials Research Letters*, 5(1):35–40, 2017.
- [194] X.B. Feng, J.Y. Zhang, Y.Q. Wang, Z.Q. Hou, K. Wu, G. Liu, and J. Sun. Size effects on the mechanical properties of nanocrystalline nbmotaw refractory high entropy alloy thin films. *International Journal of Plasticity*, 95:264 – 277, 2017.
- [195] SW Xin, M Zhang, TT Yang, YY Zhao, BR Sun, and TD Shen. Ultrahard bulk nanocrystalline vnbmotaw high-entropy alloy. *Journal of Alloys and Compounds*, 769:597–604, 2018.
- [196] Hang Zhang, Yizhen Zhao, Jianglong Cai, Shaokun Ji, Jiale Geng, Xiaoyu Sun, and Dichen Li. High-strength nbmotax refractory high-entropy alloy with low stacking fault energy eutectic phase via laser additive manufacturing. *Materials & Design*, 201:109462, 2021.
- [197] Marta Pozuelo and Jaime Marian. Microscale deformation controlled by compositional fluctuations in equiatomic nb-mo-ta-w alloys. submitted to it Materials Science and ENgineering A, 2022.
- [198] Xiangguo Li. A spectral neighbor analysis potential for nb-mo-ta-w. *OpenKIM*, 2019.
- [199] Alexander Stukowski. Visualization and analysis of atomistic simulation data with OVITO-the Open Visualization Tool. *MODELLING AND SIMULATION IN MATERIALS SCIENCE AND ENGINEERING*, 18(1), JAN 2010.
- [200] Yu Zou, Huan Ma, and Ralph Spolenak. Ultrastrong ductile and stable high-entropy alloys at small scales. *Nature communications*, 6(1):1–8, 2015.
- [201] P Thirathipviwat, G Song, J Bednarcik, U Kühn, T Gemming, K Nielsch, and J Han. Compositional complexity dependence of dislocation density and mechanical properties in high entropy alloy systems. *Progress in Natural Science: Materials International*, 30(4):545–551, 2020.
- [202] Jenő Gubicza, Anita Heczal, Megumi Kawasaki, Jae-Kyung Han, Yakai Zhao, Yunfei Xue, Shuo Huang, and János L Lábár. Evolution of microstructure and

- hardness in hf25nb25ti25zr25 high-entropy alloy during high-pressure torsion. *Journal of Alloys and Compounds*, 788:318–328, 2019.
- [203] Athanasios Arsenlis, Wei Cai, Meijie Tang, Moono Rhee, Tomas Opperstrup, Gregg Hommes, Tom G Pierce, and Vasily V Bulatov. Enabling strain hardening simulations with dislocation dynamics. *Modelling and Simulation in Materials Science and Engineering*, 15(6):553, 2007.
- [204] O Jamond, R Gatti, Arjen Roos, and Benoit Devincere. Consistent formulation for the discrete-continuous model: Improving complex dislocation dynamics simulations. *International Journal of Plasticity*, 80:19–37, 2016.
- [205] Celine Varvenne, Aitor Luque, and William A. Curtin. Theory of strengthening in fcc high entropy alloys. *Acta Materialia*, 118:13. 164–176, 2016.
- [206] Francesco Maresca and William A Curtin. Mechanistic origin of high strength in refractory bcc high entropy alloys up to 1900k. *Acta Materialia*, 182:235–249, 2020.
- [207] N Shiotani, H Kimura, RR Hasiguti, and R Maddin. The mechanism of hardening in quenched aluminum. *Acta Metallurgica*, 15(2):287–296, 1967.
- [208] Sadakichi Kitajima, Hiroaki Kurishita, and Yuichi Sakurai. Yielding mechanism of highly perfect copper single crystals. *Memoirs of the Faculty of Engineering, Kyushu University*, 69(3), 2009.
- [209] Kinshuk Srivastava, Satish I Rao, and Jaafar A El-Awady. Unveiling the role of super-jogs and dislocation induced atomic-shuffling on controlling plasticity in magnesium. *Acta Materialia*, 161:182–193, 2018.
- [210] J. S. Koehler. The nature of work-hardening. *Phys. Rev.*, 86:52–59, Apr 1952.
- [211] Hiroyasu SAKA, Kenji NODA, and Toru IMURA. Direct observation of dislocation multiplication in iron at low temperatures by hvem. *Transactions of the Iron and Steel Institute of Japan*, 13(5):318–324, 1973.
- [212] E. Martinez, J. Marian, A. Arsenlis, M. Victoria, and J.M. Perlado. A dislocation dynamics study of the strength of stacking fault tetrahedra. part i: interactions with screw dislocations. *Philosophical Magazine*, 88(6):809–840, 2008.

- [213] Lin Song, Junpin Lin, and Jinshan Li. Ordinary dislocation configurations in high nb-containing tial alloy deformed at high temperatures. *Philosophical Magazine*, 97(7):515–526, 2017.
- [214] SI Rao, B Akdim, E Antillon, C Woodward, TA Parthasarathy, and ON Senkov. Modeling solution hardening in bcc refractory complex concentrated alloys: Nbtizr, nb1. 5tizr0. 5 and nb0. 5tizr1. 5. *Acta Materialia*, 168:222–236, 2019.
- [215] Francesco Maresca and William A Curtin. Theory of screw dislocation strengthening in random bcc alloys from dilute to “high-entropy” alloys. *Acta Materialia*, 182:144–162, 2020.
- [216] L. Lilensten, J.-P. Couzini, L. Perri, A. Hocini, C. Keller, G. Dirras, and I. Guillot. Study of a bcc multi-principal element alloy: Tensile and simple shear properties and underlying deformation mechanisms. *Acta Materialia*, 142:131 – 141, 2018.
- [217] Fulin Wang, Glenn H Balbus, Shuozhi Xu, Yanqing Su, Jungho Shin, Paul F Rottmann, Keith E Knipling, Jean-Charles Stinville, Leah H Mills, Oleg N Senkov, et al. Multiplicity of dislocation pathways in a refractory multiprincipal element alloy. *Science*, 370(6512):95–101, 2020.
- [218] Chien-Chang Juan, Ming-Hung Tsai, Che-Wei Tsai, Chun-Ming Lin, Woei-Ren Wang, Chih-Chao Yang, Swe-Kai Chen, Su-Jien Lin, and Jien-Wei Yeh. Enhanced mechanical properties of hfmotatizr and hfmonbtatizr refractory high-entropy alloys. *Intermetallics*, 62:76–83, 2015.
- [219] Oleg N Senkov, Daniel B Miracle, Kevin J Chaput, and Jean-Philippe Couzini. Development and exploration of refractory high entropy alloys—a review. *Journal of materials research*, 33(19):3092–3128, 2018.
- [220] Rui Feng, Bojun Feng, Michael C Gao, Chuan Zhang, Joerg C Neuefeind, Jonathan D Poplawsky, Yang Ren, Ke An, Michael Widom, and Peter K Liaw. Superior high-temperature strength in a supersaturated refractory high-entropy alloy. *Advanced Materials*, 33(48):2102401, 2021.
- [221] A Vattré, B Devincre, and A Roos. Dislocation dynamics simulations of precipitation hardening in ni-based superalloys with high γ volume fraction. *Intermetallics*, 17(12):988–994, 2009.

- [222] Gabor A. Somorjai and Yimin Li. Impact of surface chemistry. *Proceedings of the National Academy of Sciences*, 108(3):917–924, 2011. eprint: <https://www.pnas.org/doi/pdf/10.1073/pnas.1006669107>.
- [223] Jens K. Nørskov, Frank Abild-Pedersen, Felix Studt, and Thomas Bligaard. Density functional theory in surface chemistry and catalysis. *Proceedings of the National Academy of Sciences*, 108(3):937–943, 2011. eprint: <https://www.pnas.org/doi/pdf/10.1073/pnas.1006652108>.
- [224] Shengnan Sun, Haiyan Li, and Zhichuan J. Xu. Impact of surface area in evaluation of catalyst activity. *Joule*, 2(6):1024–1027, 2018.
- [225] M.A. Meyers, A. Mishra, and D.J. Benson. Mechanical properties of nanocrystalline materials. *Progress in Materials Science*, 51(4):427–556, May 2006.
- [226] P. Marin and A. Hernando. Applications of amorphous and nanocrystalline magnetic materials. *Journal of Magnetism and Magnetic Materials*, 215–216:729–734, 2000.
- [227] C. S. Witharamage, J. Christudasjustus, J. Smith, W. Gao, and R. K. Gupta. Corrosion behavior of an in situ consolidated nanocrystalline Al-V alloy. *npj Materials Degradation*, 6(1):15, February 2022.
- [228] R. K. Gupta and N. Birbilis. The influence of nanocrystalline structure and processing route on corrosion of stainless steel: A review. *Corrosion Science*, 92:1–15, 2015.
- [229] Li Liu, Ying Li, and Fuhui Wang. Electrochemical Corrosion Behavior of Nanocrystalline Materials—a Review. *Journal of Materials Science & Technology*, 26(1):1–14, 2010.
- [230] Weiping Zhang, Yi Xiong, Jiawei Wu, Wenrui Cheng, Congcong Du, Shuoxue Jin, Baoru Sun, and Tongde Shen. Comparison of helium ion irradiation resistance between nanocrystalline and coarse grained 304 austenitic stainless steel. *Nuclear Fusion*, 62(12):126034, December 2022.
- [231] Cuncai Fan, Zhongxia Shang, Tongjun Niu, Jin Li, Haiyan Wang, and Xinghang Zhang. Dual beam in situ radiation studies of nanocrystalline cu. *Materials*, 12(17), 2019.

- [232] Christopher M. Barr, Nan Li, Brad L. Boyce, and Khalid Hattar. Examining the influence of grain size on radiation tolerance in the nanocrystalline regime. *Applied Physics Letters*, 112(18):181903, 05 2018.
- [233] I. J. Beyerlein, A. Caro, M. J. Demkowicz, N. A. Mara, A. Misra, and B. P. Uberuaga. Radiation damage tolerant nanomaterials. *Materials Today*, 16(11):443–449, 2013.
- [234] S. Srinivasan, C. Kale, B. C. Hornbuckle, K. A. Darling, M. R. Chancey, E. Hernández-Rivera, Y. Chen, T. R. Koenig, Y. Q. Wang, G. B. Thompson, and K. N. Solanki. Radiation tolerance and microstructural changes of nanocrystalline Cu-Ta alloy to high dose self-ion irradiation. *Acta Materialia*, 195:621–630, 2020.
- [235] Sanchita Dey, John W. Drazin, Yongqiang Wang, James A. Valdez, Terry G. Holesinger, Blas P. Uberuaga, and Ricardo H. R. Castro. Radiation Tolerance of Nanocrystalline Ceramics: Insights from Yttria Stabilized Zirconia. *Scientific Reports*, 5(1):7746, January 2015.
- [236] O. El-Atwani, E. Esquivel, E. Aydogan, E. Martinez, J. K. Baldwin, M. Li, B. P. Uberuaga, and S. A. Maloy. Unprecedented irradiation resistance of nanocrystalline tungsten with equiaxed nanocrystalline grains to dislocation loop accumulation. *Acta Materialia*, 165:118–128, 2019.
- [237] James E. Nathaniel, Pranav K. Suri, Emily M. Hopkins, Jianguo Wen, Peter Baldo, Marquis Kirk, and Mitra L. Taheri. Grain boundary strain as a determinant of localized sink efficiency. *Acta Materialia*, 226:117624, 2022.
- [238] Christopher M. Barr, Elton Y. Chen, James E. Nathaniel, Ping Lu, David P. Adams, Rémi Dingreville, Brad L. Boyce, Khalid Hattar, and Douglas L. Medlin. Irradiation-induced grain boundary facet motion: In situ observations and atomic-scale mechanisms. *Science Advances*, 8(23):eabn0900, 2022.
- [239] Yinguang Piao and Khanh Chau Le. Thermodynamic theory of dislocation/grain boundary interaction. *Continuum Mechanics and Thermodynamics*, 34(3):763–780, May 2022.
- [240] C. Y. Hung, G. Vetterick, E. Hopkins, J. K. Balwin, P. Baldo, M. A. Kirk, A. Misra, and M. L. Taheri. Insight into defect cluster annihilation at grain boundaries in an irradiated nanocrystalline iron. *Journal of Nuclear Materials*, 566:153761, 2022.

- [241] M. A. Kirk, M. L. Jenkins, and H. Fukushima. The search for interstitial dislocation loops produced in displacement cascades at 20 K in copper. *Journal of Nuclear Materials*, 276(1):50–58, 2000.
- [242] A. V. Barashev, S. I. Golubov, and R. E. Stoller. Theoretical investigation of microstructure evolution and deformation of zirconium under neutron irradiation. *Journal of Nuclear Materials*, 461:85–94, 2015.
- [243] D. R. Mason, X. Yi, M. A. Kirk, and S. L. Dudarev. Elastic trapping of dislocation loops in cascades in ion-irradiated tungsten foils. *Journal of Physics: Condensed Matter*, 26(37):375701, August 2014. Publisher: IOP Publishing.
- [244] Larissa M. Woryk, Sicong He, Emily M. Hopkins, Chang-Yu Hung, Jian Han, David J. Srolovitz, Jaime Marian, and Mitra L. Taheri. Geometrically necessary dislocation fingerprints of dislocation loop absorption at grain boundaries. *Phys. Rev. Mater.*, 6:083804, Aug 2022.
- [245] Yang Li, Max Boleininger, Christian Robertson, Laurent Dupuy, and Sergei L. Dudarev. Diffusion and interaction of prismatic dislocation loops simulated by stochastic discrete dislocation dynamics. *Phys. Rev. Mater.*, 3(7):073805, July 2019. Publisher: American Physical Society.
- [246] K. Arakawa, K. Ono, M. Isshiki, K. Mimura, M. Uchikoshi, and H. Mori. Observation of the one-dimensional diffusion of nanometer-sized dislocation loops. *Science*, 318(5852):956–959, 2007.
- [247] D. Hull and D. J. Bacon. Chapter 4 - Elastic Properties of Dislocations. In D. Hull and D. J. Bacon, editors, *Introduction to Dislocations (Fifth Edition)*, pages 63–83. Butterworth-Heinemann, Oxford, fifth edition edition, 2011.
- [248] N. Gao, Z. W. Yao, G. H. Lu, H. Q. Deng, and F. Gao. Mechanisms for $\langle 100 \rangle$ interstitial dislocation loops to diffuse in BCC iron. *Nature Communications*, 12(1):225, January 2021.
- [249] Xiaoyang Wang, Ning Gao, Yinan Wang, Xiaoyu Wu, Guogang Shu, Chengliang Li, Qiulin Li, Ben Xu, and Wei Liu. Formation of $\langle 100 \rangle$ dislocation loop in bcc-Fe via the ternary loop reaction. *Scripta Materialia*, 162:204–208, 2019.
- [250] Jaime Marian, Brian D. Wirth, and J. Manuel Perlado. Mechanism of formation and growth of $\langle 100 \rangle$ interstitial loops in ferritic materials. *Phys Rev Lett*, 88(25 Pt 1):255507, June 2002. Place: United States.

- [251] K. Arakawa, M. Hatanaka, E. Kuramoto, K. Ono, and H. Mori. Changes in the Burgers Vector of Perfect Dislocation Loops without Contact with the External Dislocations. *Phys. Rev. Lett.*, 96(12):125506, March 2006. Publisher: American Physical Society.
- [252] J. Marian, B. D. Wirth, A. Caro, B. Sadigh, G. R. Odette, J. M. Perlado, and T. Diaz de la Rubia. Dynamics of self-interstitial cluster migration in pure α -Fe and Fe-Cu alloys. *Phys. Rev. B*, 65(14):144102, March 2002. Publisher: American Physical Society.
- [253] G. Vetterick, J. K. Baldwin, A. Misra, and M. L. Taheri. Texture evolution in nanocrystalline iron films deposited using biased magnetron sputtering. *Journal of Applied Physics*, 116(23):233503, 12 2014.
- [254] Paul Erhart and Jaime Marian. Calculation of the substitutional fraction of ion-implanted He in an α -Fe target. *Journal of Nuclear Materials*, 414(3):426–430, 2011.
- [255] Joaquim Portillo, Edgar F. Rauch, Stavros Nicolopoulos, Mauro Gemmi, and Daniel Bultreys. Precession Electron Diffraction Assisted Orientation Mapping in the Transmission Electron Microscope. *Materials Science Forum*, 644:1–7, 2010. Publisher: Trans Tech Publications Ltd.
- [256] Edgar F. Rauch, Joaquim Portillo, Stavros Nicolopoulos, Daniel Bultreys, Sergei Rouvimov, and Peter Moeck. Automated nanocrystal orientation and phase mapping in the transmission electron microscope on the basis of precession electron diffraction. 225(2-3):103–109, 2010.
- [257] C. Begau, J. Hua, and A. Hartmaier. A novel approach to study dislocation density tensors and lattice rotation patterns in atomistic simulations. *Journal of the Mechanics and Physics of Solids*, 60(4):711–722, 2012.
- [258] Ryosuke Matsutani and Susumu Onaka. Representation of nye’s lattice curvature tensor by log angles. *MATERIALS TRANSACTIONS*, 60(6):935–938, 2019.
- [259] Plotly Technologies Inc. Collaborative data science, 2015. Place: Montreal, QC Publisher: Plotly Technologies Inc.
- [260] B. D. Wirth, G. R. Odette, D. Maroudas, and G. E. Lucas. Dislocation loop structure, energy and mobility of self-interstitial atom clusters in bcc iron. *Journal of Nuclear Materials*, 276(1):33–40, 2000.

- [261] M. Hernández-Mayoral and D. Gómez-Briceño. Transmission electron microscopy study on neutron irradiated pure iron and RPV model alloys. *Journal of Nuclear Materials*, 399(2):146–153, 2010.
- [262] Daniel Foley and Garritt J Tucker. Quantifying grain boundary damage tolerance with atomistic simulations. *Modelling and Simulation in Materials Science and Engineering*, 24(7):075011, September 2016. Publisher: IOP Publishing.
- [263] N. Matsunami, T. Murase, M. Tazawa, S. Ninad, O. Fukuoka, T. Shimura, M. Sataka, and Y. Chimi. Analysis of N isotope depth profiles in search for reaction of implanted nitrogen with substrate near Si₃N₄–nitride–film and SiO₂–glass–substrate interface. *Nuclear Instruments and Methods in Physics Research Section B: Beam Interactions with Materials and Atoms*, 249(1):185–188, August 2006.
- [264] Christopher M. Barr, Leland Barnard, James E. Nathaniel, Khalid Hattar, Kinga A. Unocic, Izabela Szlurfarska, Dane Morgan, and Mitra L. Taheri. Grain boundary character dependence of radiation-induced segregation in a model Ni–Cr alloy. *Journal of Materials Research*, 30(9):1290–1299, May 2015.
- [265] O. El-Atwani, E. Martinez, E. Esquivel, M. Efe, C. Taylor, Y. Q. Wang, B. P. Uberuaga, and S. A. Maloy. Does sink efficiency unequivocally characterize how grain boundaries impact radiation damage? *Phys. Rev. Mater.*, 2(11):113604, November 2018. Publisher: American Physical Society.
- [266] Jaime Marian, Steve Fitzgerald, and Giacomo Po. Discrete Dislocation Dynamics Simulations of Irradiation Hardening in Nuclear Materials. In Wanda Andreoni and Sidney Yip, editors, *Handbook of Materials Modeling: Applications: Current and Emerging Materials*, pages 1–29. Springer International Publishing, Cham, 2018.
- [267] Shu Huang and Jaime Marian. Rates of diffusion controlled reactions for one-dimensionally-moving species in 3D space. *Philosophical Magazine*, 99(20):2562–2583, October 2019. Publisher: Taylor & Francis.
- [268] O. V. Ogorodnikova, M. Majerle, J. Čížek, S. Simakov, V. V. Gann, P. Hruška, J. Kameník, J. Pospíšil, M. Štefánik, and M. Vinš. Positron annihilation spectroscopy study of radiation-induced defects in W and Fe irradiated with neutrons with different spectra. *Sci Rep*, 10(1):18898, November 2020. Place: England.

- [269] Jenna L. Wardini, Charlette M. Grigorian, and Timothy J. Rupert. Amorphous complexions alter the tensile failure of nanocrystalline Cu-Zr alloys. *Materialia*, 17:101134, 2021.
- [270] Vladyslav Turlo and Timothy J. Rupert. Grain boundary complexions and the strength of nanocrystalline metals: Dislocation emission and propagation. *Acta Materialia*, 151:100–111, 2018.
- [271] Timothy J. Rupert. The role of complexions in metallic nano-grain stability and deformation. *Current Opinion in Solid State and Materials Science*, 20(5):257–267, 2016.